Transport of Elliptic Intense Charged-Particle Beams

by

Jing Zhou

Submitted to the Department of Physics
in partial fulfillment of the requirements for the degree of

Doctor of Philosophy in Physics

at the

MASSACHUSETTS INSTITUTE OF TECHNOLOGY

June 2006

Author.....
Department of Physics
May 25, 2006

Certified by.....
Richard J. Temkin
Senior Scientist
Thesis Supervisor

Certified by.....
Chiping Chen
Principal Research Scientist
Thesis Supervisor

Accepted by.....
Thomas J. Greytak
Professor & Associate Department Head for Education

Transport of Elliptic Intense Charged-Particle Beams

by

Jing Zhou

Submitted to the Department of Physics
on May 26, 2006 in partial fulfillment of the
requirements for the degree of Doctor of Philosophy in
Physics

Abstract

The transport theory of high-intensity elliptic charged-particle beams is presented. In particular, the halo formation and beam loss problem associated with the high space charge and small-aperture structure is addressed, and a novel transport theory of large-aspect-ratio elliptic beams has been developed.

In a small-aperture system image-charge effects have been found to be a new mechanism for inducing chaotic particle motion, halo formation and beam loss. The rms envelope equations have been derived and analyzed for unbunched intense charged-particle beams in an alternating-gradient focusing field and a cylindrical metal pipe. Numerical results have shown that for vacuum phase advance $\sigma_v < 90^\circ$, the higher-order image-charge effects on the matched and slightly mismatched beam envelopes are negligibly small for all beams with arbitrary beam density profiles (including hollow density profiles) as well as for arbitrary small apertures (including beams with large aspect ratios). However, the main unstable region for the envelope evolution with image-charge effects, which occurs for $90^\circ < \sigma_v < 270^\circ$, depending on the value of the normalized beam intensity SK/ε, has been found to be narrower than its counterpart without image-charge effects. Using the test-particle model it has been shown that in a small-aperture alternating-gradient focusing channel, image-charge effects induce chaotic particle motions and halo formation in intense charge-particle beams. This mechanism occurs for well-matched beams with the ideal Kapchinskij-Vladimirskij (KV) distribution. The halo formation and beam loss are sensitive to system parameters: the quadruple focusing field filling factor, the vacuum phase advance, the perveance and the pipe radius. As shown in our parametric studies, the beam loss increases rapidly as the perveance of the beam increases and as the pipe radius decreases. In addition, a self-consistent PIC simulation code, Periodically Focused Beam (PFB2D), has been developed, and used to simulate intense charged-particle beams in small-aperture alternating-gradient systems. PIC simulation results on the beam envelope are consistent with the envelope equation solutions. However, due to numerical noise in PIC simulations, the beam loss predicted by PIC simulation has been found to be an order of magnitude higher than that predicted by the test-particle model. To analyze the noise in PIC simulations, an error scaling law for the edge emittance growth and particle diffusion due to the discrete macro-particle effects has been derived for self-consistent intense beam simulations. The error scaling

law has been tested in the self-consistent Green's function simulations and self-consistent PIC PFB2D simulations. The simulation results have shown good agreement with the scaling law.

Novel exact paraxial cold-fluid and Vlasov equilibria have been found for a high-intensity, space-charge-dominated charged-particle beam with a periodically twisted elliptic cross section in a non-axisymmetric periodic magnetic field. Generalized envelope equations, which determine the beam envelopes, ellipse orientation, density, and internal flow velocity profiles, have been derived, and solved numerically for nonrelativistic and relativistic examples of such beams. The equilibrium and stability of such beams have been demonstrated by self-consistent particle-in-cell (PIC) simulations. For current applications, the temperature effects are found to be small on a periodically twisted large-aspect-ratio elliptic beam. We anticipate that the equilibrium theory will provide a valuable tool in the design of high-intensity elliptic beams in novel vacuum electron devices, especially for ribbon-beam klystrons (RBKs) and ribbon-beam traveling-wave amplifiers (RBA). The ellipse-shaped beam equilibria may provide some flexibility in the design and operation of high-intensity accelerators.

Thesis Supervisor: Richard J. Temkin
Title: Senior Scientist, Department of Physics

Thesis Supervisor: Chiping Chen
Title: Principal Research Scientist

Acknowledgement

I would like to thank my thesis supervisor Dr. Richard Temkin and Dr. Chiping Chen. Dr. Richard Temkin has provided me guidance and great advises through the work. Dr. Chiping Chen has been always available for help and guidance with a lot of interest and patience. I am thankful to him for giving me the opportunity to work on this research and helping me when I encountered difficulties.

I learned a lot about heavy ion beams experiments and simulations from Dr. Enrique Henestroza. I thank Professor Mark Hess for his help and encouragement during the first couple of years of my stay at MIT. I thank Professor Baoliang Qian for his contribution on the envelope studies. Professor Renato Pakter contributed a lot to the work of particle-in-cell noise analysis. I enjoyed the discussions about large-aspect-ratio elliptic beams with Dr. Ronak Bhatt and Mr. Tom Bemis. I also thank Dr. Amit Kesar for helping me visualized some of my simulations and for having fun of playing table tennis with me. My fellow graduate students, Evgenya Smirnova, Ksenia Samokhvalova, Eun-mi Choi, Melissa Hornstein and Roark Marsh were a great company and made my stay so enjoyable.

Thank Fuwan Gan, Li Yu, Li He, Fei Zhou, Hai Jiang, and Yi Zheng for being good friends and being supportive and helpful. Finally, thanks to my father and my mother for their love, support and encouragement. Without you, I would have never accomplished this work.

Contents

Chapter 1

Introduction

1.1 Applications of intense charged-particle beams

The field of intense charged-particle beams is a rapidly growing field due to many important applications ranging from inertial confinement fusion, to high-energy density physics, to particle accelerators, to high power sources of coherent radiation, to vacuum electron devices [1], to mention a few examples.

For inertial confinement fusion or related high-energy density physics research, research on intense heavy-ion beams are being studied at Virtual National Laboratory for Heavy-Ion Fusion (VNL-HIF) and other research institutions. Heavy-ion fusion uses beams of heavy ions from accelerators to produce X rays to compress and heat the target. The resulting burst of fusion energy is contained, captured, and converted into heat in the target chamber. The intense ion beams will have a total energy of 5 MJ, a focal spot radius of 3 mm, a pulse duration of 10 ns, and a total current of 40 kA on target. The current focus of HIF research is a series of small-scale experiments to study certain key aspects of intense-beam physics. These experiments include the High-Brightness Injector Experiment to study the generation of beams with high current density, the High-Current Experiment (HCX) [2] to investigate questions of beam transport, acceleration and steering, and the Neutralized Transport Experiment (NTX) [3] to model certain aspects of beam transport in a fusion chamber. In high-energy density physics research, intense ion beams are required to deliver an energy density of 1-10 J/mm^3 .

In particle accelerators, intense proton, antiproton, electron and positron beams are used. Examples of such particle accelerators are the Spallation Neutron Source (SNS) and the Large Hadron Collider (LHC) under construction, and the International Linear Collider (ILC) which is being designed. The charged-particle beam has extremely high intensity at the low-energy front end (i.e., the injector and the damping ring) of each of those machines. As the beam is accelerated, maintenance of the high intensity is critical in order to achieve desired luminosity so that the precision measurements can be made in a reasonable length of time at LHC or ILC, or the neutron intensity is sufficiently high at SNS.

Besides major efforts on intense beams in particle accelerator, there are vigorous research activities in the research and development of RF sources which employ intense electron beams. For example, sheet-beam klystrons are being studied in Stanford Linear Accelerator Center (SLAC) [4]. A mm-wave sheet-beam traveling-wave tube has been under development at Los Alamos National Laboratory (LANL) [5]. At MIT, efforts have been made on designing large-aspect-ratio beams which will be used in a ribbon-beam traveling-wave tube amplifier (RBA) for wireless communications and ribbon-beam klystrons for direct energy and ILC.

1.2 Physics of intense charged-particle beams

An intense charged-particle beam can be characterized as organized charged particles (ions or electrons) for which the effects of beam self-field are of major importance in determining the evolution of the beam. The high-intensity charged-particle (ion or electron) beams in all the applications mentioned above have the following unique properties.

1. The beams are nonneutral plasmas which have one component (ions, electrons or antiparticles).

2. The beams travel in a periodic electric and/or magnetic focusing channel. The motion of particles is paraxial, i.e., the longitudinal energy of the particles is much higher than their transverse energy.
3. The thermal energies in the beams are low compared with the mean-flow kinetic energies.
4. The beams are in the space-charge-dominated regimes. The condition of a space-charged dominated beam is

$$K >> \frac{1}{2}\frac{\varepsilon_x^2}{\langle x^2 \rangle}, \tag{1.1}$$

where the normalized self-field perveance K and the unnormalized transverse emittance ε_x in any transverse direction are defined by

$$K = \frac{2Z_i N_b e^2}{\gamma_b^3 m_b \beta_b^2 c^2} \tag{1.2}$$

and

$$\varepsilon_x^2 = \frac{4}{\beta_b^2 c^2}\left[\langle x^2 \rangle \langle v_x^2 \rangle - \langle x v_x \rangle^2\right], \tag{1.3}$$

with the average defined as $\langle \chi \rangle = \int \chi f_b(\mathbf{x}, \mathbf{v}, t) d\mathbf{x} d\mathbf{v}$.

As a one-component nonneutral plasma, an intense charged-particle beam is a many-body collection of charged particles which exhibit a broad range of collective phenomena, such as plasma equilibrium and instabilities. Basic theoretical frameworks, such as single-particle orbit theory, fluid theory and kinetic theory are employed in studying the behavior of high-intensity charged-particle beams. In particular, space-charge fields have strong influence on the dynamics

of intense beams. In this regard, an improved theoretical understanding of the nonlinear dynamics and detailed transport properties is needed.

1.3 Issues of intense beams

There are many issues that must be addressed in order to achieve the required intensity and performance of intense beams. In the scope of this thesis, however, we will focus on two outstanding issues of high-intensity beams; namely, chaotic particle motion, halo formation and particle losses in intense beams, and the transport of large-aspect-ratio elliptic beams.

It is of critical importance to understand the mechanisms and control of chaotic particle motion, halo formation and particle losses in intense charged-particle beams in order to design and operate intense beam systems [6][7]. Beam loss due to halo formation is very harmful to the intense charged-particle systems. For example, in the heavy-ion fusion system, halo production prevents the final ion beam from being focused to a spot radius of 3 mm. On the other hand, in SNS, LHC and ILC, halo production dilutes the beam quality, degrades luminosity, and limits the machine performance. In addition, a fractional loss of only 10^{-7} of the beam is sufficient to quench a superconducting magnet, while the beam dump on the accelerator structure discharges an energy equivalent to a considerable concentration of explosives.

In order to minimize or control beam loss, it is necessary to study and understand the physics of halo formation because the beam loss is typically associated with the low density halo surrounding beam core for well controlled beams. Similar to a moon halo, a ring of light surrounding the moon, the beam halo is a ring of charged particles surrounding the beam core. As shown in Fig. 1.1, the beam halo is formed by the sparse particles surrounding the beam core which has a circular boundary indicated by the purple ring in Fig. 1.1 [8]. In particular, the halo

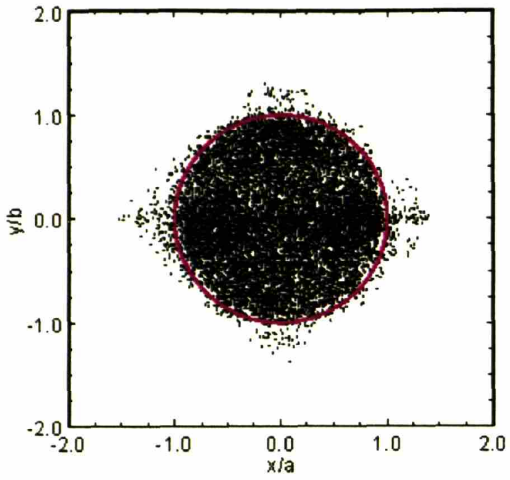

Fig. 1.1 An illustration of the beam halo in the cross-section plane (x, y).

formation is closely related to chaotic particle motion due to nonlinear effects. The intrinsic space-charge effects of intense charged-particle beams have been found to play an important role in inducing chaotic particle motion, beam halo formation and beam loss [7]-[9].

The other focus of this thesis is to understand the transport of a large-aspect-ratio elliptic beam which had not been well understood. Such beams have very important applications in accelerators and vacuum electron devices. For example, in the final collision section of a linear collider, electron and positron beams with an aspect ratio of ~100 collide with each other. Sophisticated manipulation of intense elliptic beams is required in a linear collider. On the other hand, large-aspect-ratio elliptic beams have many important applications in RF sources including klystrons, traveling-wave tubes and other vacuum electron devices.

Most beams are focused either by a periodic solenoidal magnetic focusing channel or by a periodic electric or magnetic quadrupole focusing channel. Although a conventional space-charge-dominated beam normally has an elliptic cross-section, the beam envelopes alternates and

the beams are circular on average, i.e., the beam envelopes averages over one period in different directions are equal. In the conventional space-charge-dominated beams, the halo formation and beam loss, induced by the space-charge effects and image-charge effects are found to be important. In order to reduce to the space charge effects and image-charge effects, a large-aspect-ratio elliptic beam is explored. A large-aspect-ratio beam normally has an elliptic cross section which is kept almost constant as it propagates. Large-aspect-ratio elliptic beams have a lower intrinsic space-charge force and a lower intrinsic space-charge energy. Halo formation and beam loss is expected to be less pronounced in large-aspect-ratio elliptic beams.

In addition to the reduced space-charge force and energy, large-aspect-ratio beams couple efficiently to rectangular rf structures. The combination of the space charge reduction and efficient coupling allows efficient rf generation in vacuum electron devices, and efficient acceleration in particle accelerators. Moreover, elliptic beams provide an additional adjustable parameter (e.g., the aspect ratio) which may be useful for better matching a beam into a periodic focusing channel.

1.4 Thesis outline

This thesis is organized broadly in two parts. The first part, which includes Chapters 2-4, contains the analytical and computational studies of the image-charge effects on inducing chaotic particle motion, halo formation, and beam loss. The second part, which includes Chapter 5 and 6, explore large-aspect-ratio elliptic beams, presents the cold-fluid and kinetic equilibrium theories for intense elliptic beam transport, and particle-in-cell simulations of the equilibrium and stability of intense elliptic beams.

In Chapter 2, the root-mean-squared (rms) envelope equations are derived, including all higher-order image-charge effects from the cylindrical conducting pipe. Numerical results show that for vacuum phase advance $\sigma_v < 90^\circ$, higher-order image-charge effects on the matched and slightly mismatched beam envelopes are negligibly small for all beams with arbitrary beam density profiles as well as for arbitrary small apertures. In addition, in the operation region of the accelerator systems, the image-charge effects do not introduce instabilities.

In Chapter 3, use is made of a test-particle model to investigate the dynamics of rms matched intense charged-particle beams propagating through an alternating-gradient quadrupole magnetic field and a small aperture. The elliptical cross-section of the beam and the circular cross-section of the pipe are incorporated. It is shown that the image-charge-induced fields are nonlinear, and that they induce chaotic particle motion and halo formation and that they cause significant beam losses as the aperture decreases.

In Chapter 4, the development of a two-dimensional electrostatic PIC code, Periodically Focused Beam (PFB2D), is discussed. The code is used to simulate intense charged-particle beams in small-aperture alternating-gradient systems which are investigated theoretically in Chapter 2 and 3. The halo formation and beam loss are found in PIC simulations of those systems and are compared to those from theoretical investigations. The beam loss predicted by PIC simulation is an order of magnitude higher than that predicted by theory, which leads to the noise analysis of PIC simulations. An empirical error scaling law is found in PIC simulations, which will be useful in future studies of beam losses.

In Chapter 5, a cold-fluid equilibrium theory is presented of an ultrahigh-brightness, space-charge-dominated, large-aspect-ratio beam propagating through a non-axisymmetric periodic magnetic focusing field. A paraxial cold-fluid model is employed to derive generalized envelope

equations which determine the equilibrium flow properties of ellipse-shaped beams with negligibly small emittance. A matched envelope solution is obtained numerically from the generalized envelope equations, and the results show that the beam edges in both transverse directions are well confined, and that the angle of the beam ellipse exhibits a periodic small-amplitude twist. The slightly mismatched beams and the beam envelope instability are discussed. Two-dimensional (2D) particle-in-cell (PIC) simulations with the PFB2D code show good agreement with the predictions of the cold-fluid equilibrium theory as well as beam stability.

In Chapter 6, a Vlasov equilibrium theory is presented for a periodically twisted large-aspect-ratio intense charged-particle beam with uniform density in the transverse plane propagating through a non-axisymmetric periodic magnetic focusing field. The single-particle Hamiltonian of such a periodically twisted large-aspect-ratio elliptic beam is investigated. A new constant of motion is found from which a Vlasov equilibrium distribution is constructed. The beam envelope equations and flow velocity equations are derived. They are consistent with the generalized envelope equations derived from the cold-fluid theory equilibrium in the zero temperature limit. Statistical properties and possible applications of the present beam equilibrium are discussed. Effects of finite temperature on the design of intense elliptic beams are also discussed.

Chapter 2

Image-Charge Effects on the Beam Envelope Dynamics in a Small-Aperture Alternating-Gradient Focusing System

2.1 Introduction

A key issue in high-intensity beams is to minimize the aperture of the transport system, while preventing the beams from developing large-amplitude charge density and velocity fluctuations and subsequent emittance growth and halo formation. One potential cause of emittance growth and beam loss is associated with the collective instabilities. In order to understand the collective behavior of high-intensity beams in small-aperture alternating-gradient systems, one needs to start from a basic theoretical model which includes both space-charge and image-charge effects, as described by a solution to Poisson's equation with realistic boundary conditions and beam envelope equations.

Beam envelope equations in alternating-gradient focusing systems have been investigated since the late 1950s. One of the earliest works on the beam envelope equations can be found in Ref. [10], in which the well-known two-dimensional (2-D) Kapchinskij-Vladimirskij (KV) equations were derived for a uniform beam density in free space. In 1965, Lapostolle [11] derived three-dimensional (3-D) envelope equations for a bunched beam with a uniform density in free space. In 1971, Sacherer [12] and Lapostolle [13] extended, independently, the previous 2-D and 3-D results to the beams with a density profile of the elliptic-symmetry form $n\left(x^2/a^2 + y^2/b^2 + z^2/c^2\right)$ in free space. Sacherer's 2-D results, which describe the root-mean-

squared (rms) beam envelopes for all elliptical beams with arbitrary beam densities, assume the same form of the KV equations.

Recently, Allen and Reiser [14]-[16] extended Sacherer's 2-D results [12] to include the image-charge effects due to a cylindrical conducting pipe. They analyzed the first-order image-charge effects. Their results showed that the first-order image-charge effects do not affect the beam envelope evolution until the beam envelope is very close to the wall of the cylindrical conducting pipe.

In this chapter, the Allen-Reiser's 2-D envelope equations are extended to include all higher-order image-charge effects from the cylindrical conducting pipe [17][18]. In particular, the self-electric and self-magnetic fields are calculated for an unbunched beam with elliptic symmetry and an arbitrary transverse dependence. The root-mean-squared (rms) envelope equations are derived, including all higher-order image-charge effects from the cylindrical conducting pipe. Numerical results show that for vacuum phase advance $\sigma_v < 90^\circ$, higher-order image-charge effects on the matched and slightly mismatched beam envelopes are negligibly small for all beams with arbitrary beam density profiles (including hollow density profiles measured recently in the heavy ion injector experiment at Lawrence Berkeley National Laboratory (LBNL) [19]) as well as for arbitrary small apertures (including beams with large aspect ratios). However, the main unstable region for the envelope with image-charge effects, which occurs for $90^\circ < \sigma_v < 270^\circ$, depending on the value of the normalized beam intensity SK/ε, is found to be narrower than its counterpart without image-charge effects [8].

2.2 Beam envelope equations with image-charge effects

We consider an unbunched elliptical beam propagating in an alternating-gradient focusing field and a cylindrical conducting pipe with radius R, as shown in Fig. 2.1. The beam has an envelope $a(s)$ in the x-direction and an envelope $b(s)$ in the y-direction, where $s = z$. The beam drift velocity in the z direction is $v_z \approx \beta_b c$, where c is the speed of light in vacuum. In the present analysis, we assume that the beam centroid motion is stable and is on the z-axis, so that we ignore the beam centroid motion. Following the analysis of Sacherer [12], we express the beam density in a self-similar beam model as

$$n(x, y, s) = n\left(\frac{x^2}{a^2} + \frac{y^2}{b^2}\right). \tag{2.1}$$

The general rms envelope equations can be expressed as [12]

$$\frac{d^2\tilde{x}}{ds^2} + \kappa_q(s)\tilde{x} + \frac{K}{2qN_b\tilde{x}}\left\langle x\frac{\partial\phi}{\partial x}\right\rangle = \frac{1}{\tilde{x}^3}\left(\frac{\varepsilon_x}{4}\right)^2 \tag{2.2}$$

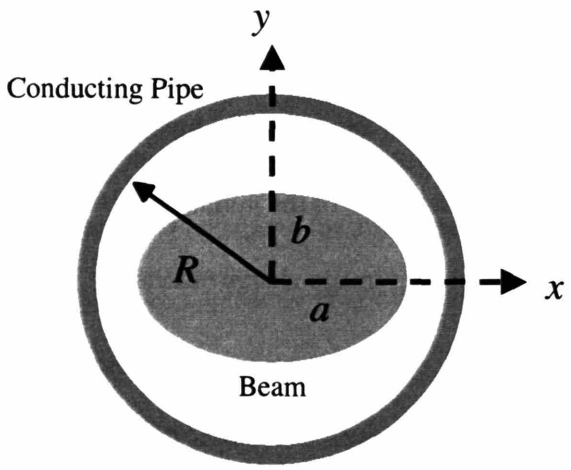

Figure 2.1 Elliptical unbunched charged-particle beam in a cylindrical conducting pipe.

and

$$\frac{d^2\tilde{y}}{ds^2} - \kappa_q(s)\tilde{y} + \frac{K}{2qN_b\tilde{y}}\left\langle y\frac{\partial\phi}{\partial y}\right\rangle = \frac{1}{\tilde{y}^3}\left(\frac{\varepsilon_y}{4}\right)^2. \tag{2.3}$$

In Eqs. (2.2) and (2.3), $\langle\ \rangle$ denotes the moment operator with respect to the particle beam distribution $f(x, y, x', y', s)$, as defined by

$$\langle\chi\rangle = \int\chi f(x, y, x', y', s)dxdydx'dy' \tag{2.4}$$

with prime denoting the derivative with respect to s (e.g, $x' = dx/ds$); $\tilde{x} = \sqrt{\langle x^2\rangle}$ and $\tilde{y} = \sqrt{\langle y^2\rangle}$ are the rms envelopes in the x- and y- directions, respectively;

$$\varepsilon_x = 4\left[\langle x^2\rangle\langle x'^2\rangle - \langle xx'\rangle^2\right]^{1/2} \tag{2.5}$$

and

$$\varepsilon_y = 4\left[\langle y^2\rangle\langle y'^2\rangle - \langle yy'\rangle^2\right]^{1/2} \tag{2.6}$$

are 4 times the beam rms emittances in the x- and y- directions, respectively; $s = \beta_b ct$ is the axial distance; ϕ is the potential distribution generated by the beam space-charge including image-charge effects of the cylindrical conducting pipe.

$$\kappa_q(s) = \frac{qB_q(s)}{(\gamma_b m\beta_b c)} \tag{2.7}$$

is the focusing parameter of the alternating-gradient focusing system;

$$\mathbf{B}^q = B_q(s)(y\mathbf{e}_x + x\mathbf{e}_y) \tag{2.8}$$

is the alternating-gradient quadrupole magnetic field with

$$B_q(s) = B_q(s+S) \equiv \left.\frac{\partial B_x^q}{\partial y}\right|_{(s,0,0)} = \left.\frac{\partial B_y^q}{\partial x}\right|_{(s,0,0)}, \tag{2.9}$$

where S is the period of the filed, m and q are the rest mass and charge of the particle, respectively.

$$K = 2q^2 N_b / \gamma^3 m \beta_b^2 c^2 \tag{2.10}$$

is the generalized beam perveance; $N_b = \int_{-\infty}^{\infty}\int_{-\infty}^{\infty} n(x,y,s)dxdy$ is the number of charged particle per unit length along the z direction; $\gamma = (1-\beta_b^2)^{-1/2}$ is the relativistic factor of the beam.

In order to derive an explicit expression for the potential ϕ, we solve Poisson's equation

$$\nabla_\perp^2 \phi = -4\pi q n\left(\frac{x^2}{a^2} + \frac{y^2}{b^2}\right) \tag{2.11}$$

under the paraxial approximation with the boundary condition $\phi|_{x^2+y^2=R} = 0$. Using Green's function technique, it is shown that the solution to Eq. (2.6) can be expressed as (see Appendix A)

$$\phi = \phi^{free} + \phi^{image}, \tag{2.12}$$

where

$$\phi^{free} = -\pi abq \int_0^\infty \frac{du}{\sqrt{(a^2+u)(b^2+u)}} \int_0^T n(T')dT' \tag{2.13}$$

is the free-space contribution of the beam,

$$\phi^{image} = \pi abq\left[\int_0^{\infty}\frac{ds}{\sqrt{(a^2+s)(b^2+s)}}\int_0^{T_1} n(T_1)dT_1 - 2\ln\frac{R}{r}\int_0^{\infty} n(T_1)dT_1\right] \tag{2.14}$$

is the image-charge contribution from the cylindrical metal pipe, and the function T is defined by

$$T = \frac{x^2}{a^2+u} + \frac{y^2}{b^2+u} \tag{2.15}$$

and the function T_1 is defined by

$$T_1 = \frac{x_1^2}{a^2+s} + \frac{y_1^2}{b^2+s} \tag{2.16}$$

with

$$x_1 = \frac{R^2 x}{x^2+y^2} \tag{2.17}$$

and

$$y_1 = \frac{R^2 y}{x^2+y^2}. \tag{2.18}$$

The space-charge terms in the envelope equations (2.2) and (2.3) can be simplified by using Eq. (2.7)-(2.10). The results are

$$\left\langle x\frac{\partial\phi}{\partial x}\right\rangle = N_b q\left(I_x^{free} + I_x^{image}\right) \tag{2.19}$$

and

$$\left\langle y\frac{\partial\phi}{\partial y}\right\rangle = N_b q\left(I_y^{free} + I_y^{image}\right), \tag{2.20}$$

where

$$I_x^{free} = -\frac{\tilde{x}}{\tilde{x}+\tilde{y}} \tag{2.21}$$

and

$$I_y^{free} = -\frac{\tilde{y}}{\tilde{x}+\tilde{y}} \tag{2.22}$$

are the space-charge contributions in free space [12], and

$$I_x^{image} = -\sum_{l=1}^{\infty} \frac{\tilde{x}^2\left(\tilde{x}^2-\tilde{y}^2\right)^{2l-1}}{R^{4l}} 4^{2l} N_l \tag{2.23}$$

and

$$I_y^{image} = -\sum_{l=1}^{\infty} \frac{\tilde{y}^2\left(\tilde{y}^2-\tilde{x}^2\right)^{2l-1}}{R^{4l}} 4^{2l} N_l \tag{2.24}$$

are the image-charge contributions from the cylindrical conducting pipe. Here,

$$N_l = 2\left(\frac{(2l)!}{4^l (l!)^2}\right)^2 \frac{\left[\int_0^{\infty} 2\pi ab\, n\left(\hat{r}^2\right)\hat{r}^{2l+1} d\hat{r}\right]^2 \left[\int_0^{\infty} 2n\left(\hat{r}^2\right)\hat{r} d\hat{r}\right]^{2l}}{N_b^2\left[4\int_0^{\infty} n\left(\hat{r}^2\right)\hat{r}^3 d\hat{r}\right]^{2l}} \tag{2.25}$$

is a multiple momentum factor related to the beam density profile.

Substituting Eqs. (2.19)-(2.25) into Eqs. (2.2) and (2.3), we obtain the envelope equations of the following form

$$\frac{d^2X}{ds^2} + \kappa_q(s)X - 2K\left[\frac{1}{X+Y} + \sum_{l=1}^{\infty} \frac{X\left(X^2-Y^2\right)^{2l-1}}{R^{4l}} N_l\right] = \frac{\varepsilon_x^2}{X^3} \tag{2.26}$$

and

$$\frac{d^2Y}{ds^2} - \kappa_q(s)Y - 2K\left[\frac{1}{X+Y} + \sum_{l=1}^{\infty} \frac{Y\left(Y^2 - X^2\right)^{2l-1}}{R^{4l}} N_l\right] = \frac{\varepsilon_y^2}{Y^3}, \tag{2.27}$$

where $X = 2\tilde{x} = 2\sqrt{\langle x^2 \rangle}$ and $Y = 2\tilde{y} = 2\sqrt{\langle y^2 \rangle}$.

Unlike the previous results obtained by Allen and Reiser [14]-[16], which include only the $l = 1$ contribution, the present envelope equations (2.21) and (2.22) are complete, including both the $l = 1$ contribution and all of the higher-order image-charge effects with $l \geq 2$.

2.3 RMS matched beams

In this section, we investigate numerically the image-charge effects on a matched beam using the analytical results obtained in Sec. 2.2, and show that for vacuum phase advance $\sigma_v < 90$, the higher-order image-charge effects on the matched beam envelopes are negligibly small for all beams with arbitrary beam density profiles with elliptic symmetry (including hollow density profiles) as well as for arbitrary small apertures (including beams with large aspect ratios). Special attention is paid to a hollow beam observed in a recent heavy ion beam experiment [19].

The multiple momentum factor N_l contains the information about the higher-order image-charge effects in the envelope equations (2.26) and (2.27). We can assess these effects by evaluating N_l as a function of l. In particular, we consider the following parabolic density profile 0

$$n=\begin{cases} n_0+\delta n_0\left[1-3\left(\dfrac{x^2}{a^2}+\dfrac{y^2}{b^2}\right)^2\right], & \dfrac{x^2}{a^2}+\dfrac{y^2}{b^2}\le 1, \\ 0, & \dfrac{x^2}{a^2}+\dfrac{y^2}{b^2}>1, \end{cases} \tag{2.28}$$

where

$$N_b=\int_{-\infty}^{\infty}\int_{-\infty}^{\infty} n\,dxdy=\pi abn_0=\text{constant}, \tag{2.29}$$

and δn_0 is independent of x and y and satisfies the inequality $-n_0\le\delta n_0\le n_0/2$.

In Eq. (2.28), the parameter $\delta n_0=0$ means that the beam density is a constant across the beam profile; The parameter $\delta n_0>0$ indicates that the beam density decreases monotonically from the center of profile to its edge and represents a Gaussian-like beam profile; The parameter $\delta n_0<0$ implies that the beam density increases monotonically from the center of beam profile to its edge and represents a hollow beam profile such as that observed in the heavy ion injector experiment at LBNL [19].

Using Eq. (2.28), we obtain the simplified expressions for the envelopes

$$X=a\left(1-\frac{1}{2}g\right)^{1/2} \tag{2.30}$$

and

$$Y=b\left(1-\frac{1}{2}g\right)^{1/2}, \tag{2.31}$$

where

$$g = \frac{\delta n_0}{n_0}. \tag{2.32}$$

Substituting Eqs. (2.28) and (2.29) into Eq. (2.25), we obtain

$$N_l = 2\left(\frac{(2l)!}{4^l (l!)^2}\right)^2 \left(\frac{1}{l-0.5g}\right)^{2l} \left(\frac{1-2gl/(l+3)}{l+1}\right)^2. \tag{2.33}$$

Note in Eq. (2.33) that $N_1 = 1/8 = 0.125$ is independent of the factor g.

Figure 2.2 shows a plot of N_l as a function of l for three cases corresponding to $g = 0$, 0.5, and -0.5. In Fig. 2.2, $N_1 = 0.125$ for all three cases, as expected. For $l \geq 2$, however, the value of N_l decreases with increasing l and depends strongly on the factor g (i.e., on the choice of the density profile). In addition, for a given value of $l > 1$, N_l increases with g; that is, the value of N_l is lower at $g = -0.5$ than at $g = 0.5$. However, this does not necessarily mean that the image charge effects of a hollow beam are weaker than those of a solid beam because the

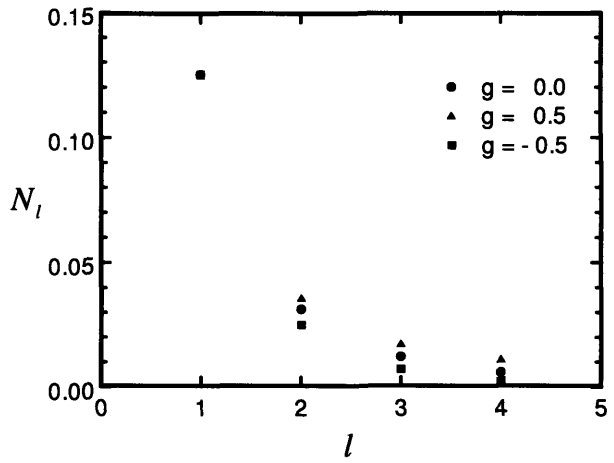

Figure 2.2 Multiple momentum factor N_l versus l for the density in Eq. (2.32) with $g = 0$, 0.5, and –0.5.

beam envelopes X and Y given by Eqs. (2.30) and (2.31) increase considerably with decreasing g. The physics of image charge effects is contained in X and Y. Obviously, the values of X and Y are higher at $g = -0.5$ than at $g = 0.5$, which implies that the image charge effects of a hollow beam are stronger than those of a solid beam.

For present purposes, we assume that the rms emittances ε_x and ε_y are assumed to be constant, i.e., $\varepsilon_x = \varepsilon_y = \varepsilon$, and that the beam density profile is given in Eq. (2.25). We also assume that the alternating-gradient transport system is presented a step-function lattice (in Fig. 2.3) defined by

$$\kappa_q(s) = \begin{cases} +\kappa_{q0}, & 0 \le s/S < 0.25\eta, \\ 0, & 0.25\eta \le s/S < 0.5(1-0.5\eta), \\ -\kappa_{q0}, & 0.5(1-0.5\eta) \le s/S < 0.5(1+0.5\eta), \\ 0, & 0.5(1+0.5\eta) \le s/S < 0.5(2-0.5\eta), \\ +\kappa_{q0}, & 0.5(2-0.5\eta) \le s/S < 1, \end{cases} \tag{2.34}$$

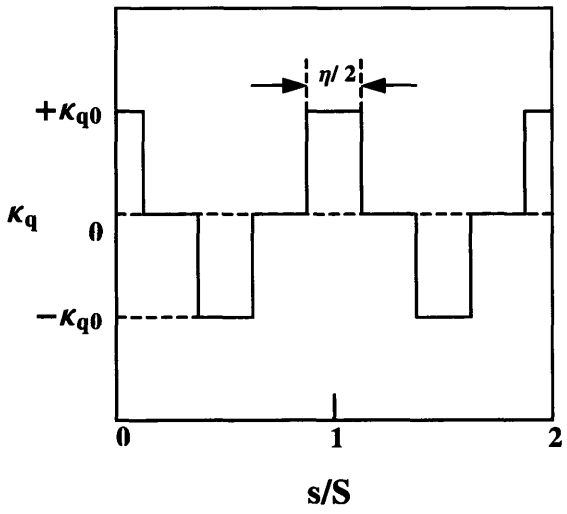

Figure 2.3 Step-function lattice $\kappa_q(s)$ versus s for $\eta = 0.5$.

where κ_{q0} is a constant and η $(0<\eta<1)$ is the filling factor of the quadrupole focusing field. The strength of the alternating-gradient focusing field can be measured in terms of the vacuum phase advances, which are defined as

$$\sigma_{vx}=\varepsilon_x\int_{s_0}^{s_0+S}\frac{ds}{a^2(s)},\ \text{and}\ \sigma_{vy}=\varepsilon_y\int_{s_0}^{s_0+S}\frac{ds}{b^2(s)}. \tag{2.35}$$

For $\varepsilon_x=\varepsilon_y=\varepsilon$ the two vacuum phase advances are equal so we define the vacuum phase advance $\sigma_v=\sigma_{vx}=\sigma_{vy}$. For step-function lattice defined in Eq. (2.34), the vacuum phase advance σ_v satisfies [8]

$$\cos\sigma_v=\cosh\varphi_1(\cos\varphi_1-\varphi_2\sin\varphi_1)+\varphi_2\sinh\varphi_1(\cos\varphi_1-0.5\varphi_2\sin\varphi_1), \tag{2.36}$$

where

$$\varphi_1=0.5S\eta\sqrt{\kappa_{q0}} \tag{2.37}$$

and

$$\varphi_2=\frac{1-\eta}{\eta}\varphi_1. \tag{2.38}$$

In the numerical analysis of the beam envelope equations (2.26) and (2.27), it is convenient to use the dimensionless parameters and normalized variables defined by $\tilde{s}=s/S$, $\tilde{a}=X/\sqrt{S\varepsilon}$, $\tilde{b}=Y/\sqrt{S\varepsilon}$, $\tilde{K}=KS/\varepsilon$, $\tilde{R}=R/\sqrt{S\varepsilon}$, and $\tilde{\kappa}_q(s)=S^2\kappa_q(s)$. For example, Fig. 2.4 shows the matched beam envelope functions $\tilde{a}(s)=\tilde{a}(s+S)$ and $\tilde{b}(s)=\tilde{b}(s+S)$ with $\sigma_v=80°$, $\tilde{K}=10$, $\eta=0.5$, and $g=-0.5$ for beam propagation in free space as well as in a cylindrical conducting pipe with $\tilde{R}=4.0$. It is evident in Fig. 2.4 that the image-charge effects, including the

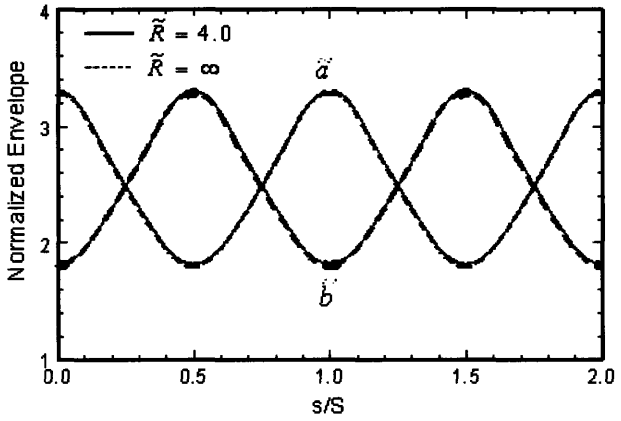

Figure 2.4 Beam envelopes $\tilde{a}$ and $\tilde{b}$ vs s/S for two case: $\tilde{R} = 4.0$ (cylindrical-conducting-pipe case) and $\tilde{R} = \infty$ (free-space case) with $\sigma_v = 80^0$, $\tilde{K} = 10$, $\eta = 0.5$ and $g = -0.5$.

contributions from all orders, are negligibly small for a hollow beam whose maximum envelopes are very close to the wall of the cylindrical pipe ($\tilde{a}_{max} = \tilde{b}_{max} \approx 3.25$ and $\tilde{R} = 4.0$).

We have carried out comprehensive numerically studies of the image-charge effects on the matched envelope functions for different beam density profiles, including beams with large aspect ratios. The numerical results show that for vacuum phase advance $\sigma_v < 90^\circ$, the total image-charge effects, including higher-order ones, do not affect significantly the matched beam envelopes for arbitrary beam density profiles with elliptic symmetry and arbitrarily small apertures (conducting pipes).

2.4 Mismatched beams and envelope instabilities

In a real device, it is difficult to obtain a precisely matched beam because there exist some perturbations on the beam propagation. These perturbations may cause beam envelope

instabilities, and the unstable beam envelopes may result in particle losses. A perturbation on the matched beam results in a mismatched beam in the alternating-gradient focusing system. The beam envelope instability has already been investigated in free space 0-[24]. However, the image-charge effects of the cylindrical conducting pipe on the mismatched beams and the beam envelope instability have not been studied until the present work. In this section, the envelope equations (2.26) and (2.27) are solved, assuming $\varepsilon_x = \varepsilon_y = \varepsilon$, for slightly mismatched beams to determine the unstable regions in the parameter space.

In order to obtain slightly mismatched beam envelopes, following the method employed in Ref. 0, the initial conditions for $\tilde{a}(s)$ and $\tilde{b}(s)$ at $s = 0$ are chosen to be

$$\tilde{a}(0) = \tilde{a}_0(1+\delta) \tag{2.39}$$

and

$$\tilde{b}(0) = \tilde{b}_0(1-\delta), \tag{2.40}$$

where $\tilde{a}_0$ and $\tilde{b}_0$ are the matched beam envelopes at $s = 0$ and δ is chosen to be in the interval of $0 \le |\delta| \le 0.01$. Here, δ represents the perturbations caused by the noise in the beam. Therefore, the initial perturbation to the matched beam envelope is assumed to be as small as 1%. In the numerical calculations, the particle beams are allowed to propagate over 40 periods. Further increasing the number of the propagation periods does not affect the determination of the unstable regions.

Figure 2.5 is a plot of $\tilde{K} = KS/\varepsilon$ versus σ_v, showing the unstable regions of the slightly mismatched beam envelopes in both the free-space and cylindrical-conducting-pipe cases for $\eta = 0.5$, $\tilde{a}_0 / \tilde{R} = 0.9$, and $g = -0.5$. As can be seen from Fig. 2.5, both unstable regions for the

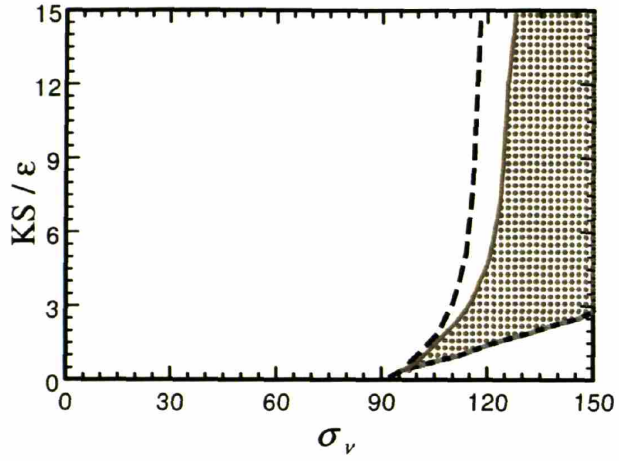

Figure 2.5 The unstable regions of the slightly mismatched beam envelopes in both the free-space and cylindrical-conducting-pipe cases for $\eta = 0.5$, $\tilde{a}_0 / \tilde{R} = 0.9$, and $g = -0.5$. The solid lines indicate the boundary of the unstable region (which is shaded) in the cylindrical conducting pipe (i.e., with image-charge effects), and the dashed lines represent the boundary of the unstable region in free space (i.e., without image-charge effects).

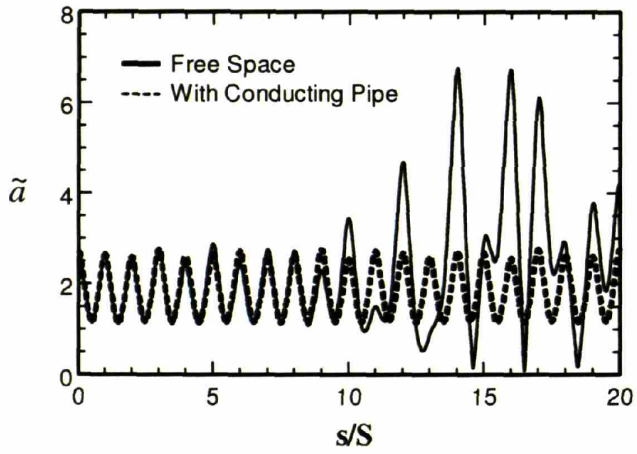

Figure 2.6 Oscillations of the beam envelope $\tilde{a}(s)$ for both the free-space and cylindrical-conducting-pipe cases at $\tilde{K} = 10.0$ and $\sigma_\nu = 120°$ corresponding to a point in Fig. 2.5 where the beam envelopes in free space are unstable but the beam envelopes in the cylindrical conducting pipe are stable.

free-space and cylindrical-conducting-pipe cases start around $\sigma_v = 90°$. The solid lines indicate the boundary of the unstable region with image-charge effects from the cylindrical conducting pipe, whereas the dashed lines represent the boundary of unstable region without image-charge effects in free space. The unstable region with image-charge effects is shaded in Fig. 2.5. Although the lower boundaries for both cases almost coincide, there is an observable difference between their upper boundaries. The unstable region for the cylindrical-conducting-pipe case (i.e., with image-charge effects) is obviously narrower than that in free space (i.e., without image-charge effects).

Figure 2.6 shows the oscillations of $\tilde{a}(s)$ for both the free-space and cylindrical-conducting-pipe cases at $\tilde{K} = 10.0$ and $\sigma_v = 120°$, which corresponds to a point in Fig. 2.5 where the beam envelopes in free space are unstable but the beam envelopes in the cylindrical conducting pipe are stable. Figure 2.7 shows the oscillations of $\tilde{a}(s)$ for both the free-space and cylindrical-conducting-pipe cases at $\tilde{K} = 10.0$ and $\sigma_v = 130°$, which corresponds to a point in Fig. 2.5 where the envelopes are unstable in both free space and the cylindrical conducting pipe. Figure 2.7 indicates that the instability growth rate for the beam envelopes in free space is greater than that in the cylindrical conducting pipe. The results for free space agree with those obtained by Qian and Davidson in Ref. [20], in which they showed an unstable region for $90° < \sigma_v < 170°$. It should be mentioned that the unstable regions are not sensitive to η and g for the case of a cylindrical conducting pipe, which is similar to the fact that the instability in free space is insensitive to η and g as noted by Qian and Davison [8].

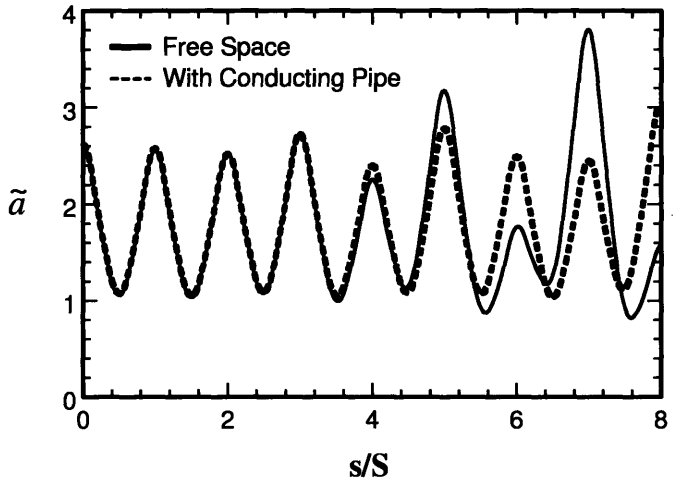

Figure 2.7 Oscillations of the beam envelope $\tilde{a}(s)$ for both the free-space and cylindrical-conducting-pipe cases at $\tilde{K} = 10.0$ and $\sigma_v = 130°$ corresponding to a point in Fig. 2.5 where the beam envelopes are unstable in both free space and the cylindrical conducting pipe.

2.5 Summary

The rms beam envelope equations (2.26) and (2.27) were derived and analyzed for unbunched intense charged-particle beams in an alternating-gradient focusing field and a cylindrical conducting pipe. For beams with elliptic symmetry all higher-order image-charge effects from the cylindrical pipe were expressed in terms of so-called multiple moment factors in the rms beam envelope equations, and the multiple momentum factors were evaluated. Numerical results showed that for vacuum phase advance $\sigma_v < 90°$, the higher-order image-charge effects on the matched and slightly mismatched beam envelopes are negligibly small for all beams with arbitrary beam density profiles with elliptic symmetry (including hollow density profiles) as well as for arbitrary small apertures (including beams with large aspect ratios). However, the main

unstable region for the beam envelope evolution with image-charge effects, which occurs for $90 < \sigma_v < 270$, depending on the value of the normalized beam intensity SK/ε, was found to be narrower than its counterpart without image-charge effects.

Chapter 3

Test-Particle Studies of Image-Charge Effects in a Small-Aperture Alternating-Gradient Focusing System

3.1 Introduction

In Chapter 2, we concluded that the image-charge effects are negligibly small on the beam envelopes and do not introduce collective instabilities in the regions of operation with $\sigma_v < 90^\circ$. The purpose of this chapter is to show that image-charge effects induce a new mechanism for chaotic particle motion, halo formation and particle losses in small-aperture alternating-gradient focusing systems.

Two key mechanisms for emittance growth and beam loss have been studied using analytical models [8][14]-[30] and self-consistent simulations with particle-in-cell (PIC) [8][31]-[33] and Green's function techniques. It has been shown in the test-particle model that chaotic particle motion and halo formation occur when the root-mean-squared (rms) beam envelopes have a sufficient large mismatch in a constant focusing channel [30] or when the beam density is sufficiently nonuniform in an alternative-gradient focusing channel [8]. Until the present analysis [34][35], however, most published analytical results on beam halo formation have been based on free-space models in which wall (image-charge) effects on halo formation have been ignored.

In particular, use is made of a test-particle model to investigate the dynamics of rms matched intense charged-particle beams propagating through an alternating-gradient quadrupole magnetic field and a small-aperture cylindrical perfectly conducting pipe [34][35]. The elliptical cross-

section of the beam and the circular cross-section of the cylindrical conducting pipe are incorporated. While the present model allows for nonuniform beams with elliptic symmetry, the effects of image charges on halo formation are illustrated with a uniform (KV) beam distribution [10]. It is shown that the image-charge-induced fields are nonlinear, that they induce chaotic particle motions and halo formation, and that they cause significant beam losses as the aperture decreases.

3.2 Test-particle models and assumptions

We consider an rms-matched, continuous, intense charged-particle beam propagating in the longitudinal direction through an alternating-gradient quadrupole magnetic field in a perfectly conducting cylindrical pipe with radius R. The motion of an individual test particle in the applied and self fields are described by the orbit equations in Cartesian coordinates [36]

$$\frac{d}{dt}p_x = Z_i e\left[E_x^{\,self} - \frac{1}{c}v_z\left(B_y^{\,self} + B_y^{\,applied}\right) + \frac{1}{c}v_y\left(B_z^{\,self} + B_z^{\,applied}\right)\right], \tag{3.1}$$

$$\frac{d}{dt}p_y = Z_i e\left[E_y^{\,self} + \frac{1}{c}v_z\left(B_y^{\,self} + B_y^{\,applied}\right) - \frac{1}{c}v_x\left(B_z^{\,self} + B_z^{\,applied}\right)\right], \tag{3.2}$$

$$\frac{d}{dt}p_z = Z_i e\left[E_z^{\,self} + \frac{1}{c}v_x\left(B_y^{\,self} + B_y^{\,applied}\right) - \frac{1}{c}v_y\left(B_y^{\,self} + B_y^{\,applied}\right)\right]. \tag{3.3}$$

Here, the particle momentum $\mathbf{p}(t)$ and particle velocity $\mathbf{v}(t) = d\mathbf{x}(t)/dt$ are related by $\mathbf{p}(t) = \gamma(t)m_i\mathbf{v}(t)$, where $\gamma(t) = \sqrt{1+\mathbf{p}^2(t)/m_i^2c^2}$, is the relativistic mass factor.

In the paraxial approximation of a unbunched beam, the conditions

$$p_z^2 >> p_x^2 + p_y^2 \quad \text{and} \quad \frac{\upsilon}{\beta_b^2 \gamma_b^3} \equiv \frac{I_b}{mc^2/Z_i e} \frac{1}{\beta_b^2 \gamma_b^3} << 1 \tag{3.4}$$

are satisfied. We approximate

$$\frac{dp_x}{dt} = mv_x \frac{d\gamma}{dt} + \gamma m \frac{d^2 x}{dt^2} \approx \gamma m \frac{d^2 x}{dt^2}. \tag{3.5}$$

Neglecting spread in the axial velocity about $v_z = p_z/\gamma m$, we further approximate $v_z \cong \beta_b c$ and $\gamma \cong \gamma_b = 1/\sqrt{1-\beta_b^2}$. We make similar approximations in Eqs. (3.2) and (3.3). Under these approximations, Eqs. (3.1) - (3.3) reduce to

$$\frac{d^2 x}{dt^2} = \frac{Z_i e}{\gamma_b m}\left[E_x^{\,self} - \frac{1}{c} v_z \left(B_y^{\,self} + B_y^{\,applied} \right) + \frac{1}{c} \frac{dy}{dt} \left(B_z^{\,self} + B_z^{\,applied} \right) \right], \tag{3.6}$$

$$\frac{d^2 y}{dt^2} = \frac{Z_i e}{\gamma_b m}\left[E_y^{\,self} + \frac{1}{c} v_z \left(B_y^{\,self} + B_y^{\,applied} \right) - \frac{1}{c} v_x \left(B_z^{\,self} + B_z^{\,applied} \right) \right], \tag{3.7}$$

$$\frac{d^2 z}{dt^2} = 0. \tag{3.8}$$

The applied alternating-gradient quadrupole magnetic field is periodic in the axial direction with periodicity length S and is defined as [see, also Eqs. (2.8) and (2.9)]

$$\mathbf{B}^{applied}(x, y, s) = B_q(s)(y\mathbf{e}_x + x\mathbf{e}_y), \tag{3.9}$$

where

$$B_q(s) = B_q(s+S) \equiv \left(\frac{\partial B_x^q}{\partial y} \right)_{(s,0,0)} = \left(\frac{\partial B_y^q}{\partial x} \right)_{(s,0,0)}, \tag{3.10}$$

is the quadrupole field gradient, (x, y) is the transverse coordinates measured from the beam axis, and $s = \beta_b ct$ is the axial distance.

The beam density is assumed to have elliptical symmetry, i.e.,

$$n = n\left(\frac{x^2}{a^2} + \frac{y^2}{b^2}\right). \tag{3.11}$$

Under steady-state condition $(\partial/\partial t = 0)$, the space charge and axial current of the beam produce an self-electric field,

$$\mathbf{E}^{self}(\mathbf{x}) = -\nabla\phi(\mathbf{x}), \tag{3.12}$$

and a self-magnetic field,

$$\mathbf{B}^{self}(\mathbf{x}) = \nabla \times \mathbf{A}^{self}(\mathbf{x}). \tag{3.13}$$

In terms of the beam density $n_b(\mathbf{x})$, Poisson's equation for $\phi(\mathbf{x})$ is given by

$$\nabla_\perp^2 \phi(\mathbf{x}) = -4\pi Z_i e n_b(\mathbf{x}). \tag{3.14}$$

For an elliptical beam in a perfectly conducting cylindrical pipe, the potential has been obtained (see Appendix A)

$$\begin{aligned}\phi = &-\pi abq \int_0^\infty \frac{ds}{\sqrt{(a^2+s)(b^2+s)}} \int_0^T n(T)dT \\ &+ \pi abq\left[\int_0^\infty \frac{ds}{\sqrt{(a^2+s)(b^2+s)}} \int_0^{T_1} n(T_1)dT_1 - 2\ln\left(\frac{R}{r}\right)\int_0^\infty n(T_1)dT_1\right],\end{aligned} \tag{3.15}$$

where

$$T = \frac{x^2}{a^2+s} + \frac{y^2}{b^2+s}, \tag{3.16}$$

$$T_1 = \frac{x_1^2}{a^2 + s} + \frac{y_1^2}{b^2 + s}, \tag{3.17}$$

with $r = \left(x^2 + y^2\right)^{1/2}$, $x_1 = R^2 x/\left(x^2 + y^2\right)$, $y_1 = R^2 y/\left(x^2 + y^2\right)$, and the periodic beam envelope functions $a(s) = a(s+S)$ and $b(s) = b(s+S)$ obey the envelope equations (2.26) and (2.27).

Since the beam has been assumed to have negligible axial velocity spread. The magnetic self-potential is determined approximately by

$$\nabla^2 A_z^{self}(\mathbf{x}) = -4\pi Z_i e \beta_b n_b(\mathbf{x}). \tag{3.18}$$

Comparing Eq. (3.14) with Eq. (3.18), we find

$$\mathbf{A}^{self}(\mathbf{x}) = A_z^{self}(\mathbf{x})\mathbf{e}_z = \beta_b \phi(\mathbf{x})\mathbf{e}_z, \tag{3.19}$$

Substituting $t = s/\beta_b s$, Eqs. (3.9), (3.12) and (3.13) into Eqs. (3.6) and (3.7) yields

$$\frac{d^2 x}{ds^2} = -\frac{Z_i e}{\gamma_b^3 m \beta_b^2 c^2}\frac{\partial \phi_0}{\partial x} - \frac{Z_i e B_q}{\gamma_b m \beta_b c^2} x \tag{3.20}$$

and

$$\frac{d^2 y}{ds^2} = -\frac{Z_i e}{\gamma_b^3 m \beta_b^2 c^2}\frac{\partial \phi_0}{\partial y} + \frac{Z_i e B_q}{\gamma_b m \beta_b c^2} y, \tag{3.21}$$

where ϕ is given by Eq. (3.15).

It is convenient to introduce the abbreviated notation

$$\kappa_q(s) = \frac{Z_i e B_q(s)}{\gamma_b m \beta_b c^2} = \frac{Z_i e}{\gamma_b m \beta_b c^2}\left(\frac{\partial B_x^q}{\partial y}\right)_{(s,0,0)}. \tag{3.22}$$

The transverse equations of motion, (3.20) and (3.21), can then be expressed in the compact form as

$$\frac{d^2x}{ds^2} + \kappa_q(s)x + \frac{Z_i e}{\gamma_b^3 m\beta_b^2 c^2}\frac{\partial \phi}{\partial x} = 0, \tag{3.23}$$

$$\frac{d^2y}{ds^2} - \kappa_q(s)y + \frac{Z_i e}{\gamma_b^3 m\beta_b^2 c^2}\frac{\partial \phi}{\partial y} = 0. \tag{3.24}$$

3.3 Chaotic particle motion, halo formation and particle losses

While the present model allows for nonuniform beams with elliptic symmetry, the effects of image charges on halo formation are illustrated with a uniform (KV) beam distribution [36], as discussed in Sec. 3.1. We consider an rms-matched continuous beam with a uniform density profile propagating in the longitudinal direction through an alternating-gradient quadrupole magnetic field in a perfectly conducting cylindrical pipe with radius R.

For the KV beam, the beam density profile is expressed as

$$n = \begin{cases} n_0, & \dfrac{x^2}{a^2} + \dfrac{y^2}{b^2} \le 1, \\ 0, & \dfrac{x^2}{a^2} + \dfrac{y^2}{b^2} \ge 1. \end{cases} \tag{3.25}$$

where $n_0 = N_b/\pi ab$.

Making use of the analytical results in Eq. (3.15), an analytical expression for the scalar potential is obtained in Appendix B for the assumed uniform-density profile. The results are

$$\phi = -\frac{2\pi abqn_0}{a+b}\left[\frac{x^2}{a}+\frac{y^2}{b}\right] + 2\pi abqn_0\left[\ln\left(\sqrt{a^2+\xi_1}+\sqrt{b^2+\xi_1}\right) - \ln(a+b) - \ln\frac{R}{\sqrt{x^2+y^2}}\right.$$
$$\left. + \frac{x^2\sqrt{b^2+\xi_1}+y^2\sqrt{a^2+\xi_1}}{\left(\sqrt{a^2+\xi_1}+\sqrt{b^2+\xi_1}\right)\sqrt{(a^2+\xi_1)(b^2+\xi_1)}} \times \frac{R^4}{(x^2+y^2)^2}\right], \quad for\ \frac{x^2}{a^2}+\frac{y^2}{b^2} \le 1; \tag{3.26}$$

$$\phi = -2\pi abqn_0\left[\ln\left(\sqrt{a^2+\xi}+\sqrt{b^2+\xi}\right) - \ln(a+b) + \frac{x^2\sqrt{b^2+\xi}+y^2\sqrt{a^2+\xi}}{\left(\sqrt{a^2+\xi}+\sqrt{b^2+\xi}\right)\sqrt{(a^2+\xi)(b^2+\xi)}}\right]$$
$$+ 2\pi abqn_0\left[\ln\left(\sqrt{a^2+\xi_1}+\sqrt{b^2+\xi_1}\right) - \ln(a+b) - \ln\frac{R}{\sqrt{x^2+y^2}}\right.$$
$$\left. + \frac{x^2\sqrt{b^2+\xi_1}+y^2\sqrt{a^2+\xi_1}}{\left(\sqrt{a^2+\xi_1}+\sqrt{b^2+\xi_1}\right)\sqrt{(a^2+\xi_1)(b^2+\xi_1)}} \times \frac{R^4}{(x^2+y^2)^2}\right], \quad for\ \frac{x^2}{a^2}+\frac{y^2}{b^2} > 1\ . \tag{3.27}$$

In Eqs. (3.26) and (3.27),

$$\xi_1 = \frac{1}{2(x^2+y^2)}\left[R^4 - (a^2+b^2)(x^2+y^2)\right.$$
$$\left. \pm\sqrt{R^8 - 2(a^2-b^2)(x^2-y^2)R^4 + (a^2-b^2)^2(x^2+y^2)^2}\right] \tag{3.28}$$

and

$$\xi = \frac{1}{2}\left[x^2+y^2-a^2-b^2 \pm \sqrt{(x^2+y^2-a^2-b^2)^2 + 4(b^2x^2+a^2y^2-a^2b^2)}\right]. \tag{3.29}$$

For the KV beam, the periodic beam envelope functions $a(s) = a(s+S)$ and $b(s) = b(s+S)$ obey [18]

$$\frac{d^2a}{ds^2} + \kappa_q(s)a - 2K\left[\frac{1}{a+b} + \sum_{l=1}^{\infty}\frac{a(a^2-b^2)^{2l-1}}{R^{4l}}N_l\right] = \frac{\varepsilon_x^2}{a^3} \tag{3.30}$$

and

$$\frac{d^2b}{ds^2} - \kappa_q(s)b - 2K\left[\frac{1}{a+b} + \sum_{l=1}^{\infty} \frac{b\left(b^2-a^2\right)^{2l-1}}{R^{4l}} N_l\right] = \frac{\varepsilon_y^2}{b^3}, \tag{3.31}$$

where $N_l = (2/\pi)[\Gamma(l+\frac{1}{2})/\Gamma(l+2)]^2$ with $\Gamma(x)$ being the standard Gamma function. Equations (3.30) and (3.31) are readily derived from Eqs. (2.26), (2.27) and (3.25).

In the paraxial approximation, the transverse equations of motion for an individual test particle in the uniform-density beam can be expressed as [36]

$$\frac{d^2x}{ds^2} + \kappa_q(s)x + \frac{q}{\gamma_b^3 m\beta_b^2 c^2}\frac{\partial\phi}{\partial x} = 0, \tag{3.32}$$

$$\frac{d^2y}{ds^2} - \kappa_q(s)y + \frac{q}{\gamma_b^3 m\beta_b^2 c^2}\frac{\partial\phi}{\partial y} = 0, \tag{3.33}$$

where ϕ is defined in (3.26) and (3.27).

In the numerical studies discussed in the reminder of this section, it is important to specify initial conditions for the test-particle motion that are consistent with the assumed beam density, which is accomplished by the particular choice of an initial distribution function [8] at $s = s_0$,

$$f_b(x, y, x', y', s_0) = N_b\delta(W-1)/\pi^2\varepsilon_x\varepsilon_y, \tag{3.34}$$

where $x' = dx/ds$, and W is the variable defined by

$$W = \frac{x^2}{a^2} + \frac{(ax'-xa')^2}{\varepsilon_x^2} + \frac{y^2}{b^2} + \frac{(by'-yb')^2}{\varepsilon_y^2}. \tag{3.35}$$

Here, a, a', b, and b' denote the "initial" values at $s = s_0$.

For the KV beam distribution, as the conducting pipe radius goes to infinity, the image charge fields vanish. Therefore, in the free-space case, the self fields have a linear dependence on x and

y within the beam boundary $x^2/a^2 + y^2/b^2 = 1$. The equations of motion reduce to uncoupled Hill's equations, and the particle orbits are confined within the beam envelope, provided the latter is stable.

As the conducting pipe radius gets close to the beam envelope, the fields become nonlinear due to the image charge on the conducting pipe. The particle orbits are non-integrable, and can become chaotic. A test-particle simulation module is added to the existing two-dimensional Periodically Focused Beam (PFB2D) code for studies of the test-particle dynamics. Equations (3.32) and (3.33) are solved numerically, where the periodic $a(s)$ and $b(s)$ are obtained numerically from the envelope equations (3.30) and (3.31). The code uses the standard IMSL Runge-Kutta integration routine [37]. For the results discussed below, a sufficiently low error tolerance of 10^{-4} is used in the simulations. We have benchmarked our numerical results against the published results for the free-space case in [8].

The mechanism of beam loss is best illustrated by the phase space structure for the test-particle motion in the plane (x, x') as shown in Fig. 3.1, where the Poincaré surface-of-section plots for the trajectories of 21 test particles are demonstrated for two cases: (a) free-space ($\hat{R} \equiv R/\sqrt{\varepsilon S} = \infty$) and (b) $\hat{R} = 4.5$. In the simulations, we use a periodic step-function lattice with filling factor η, as shown in Fig. 2.3. The system parameters are $\eta = 0.5$, $\sigma_v = 80.0°$, $KS/\varepsilon = 10.0$ and $\varepsilon_x = \varepsilon_y = \varepsilon$, which correspond to those in the planned High-Current Experiment (HCX) at LBNL [38].

For these parameters, the maximum value of the normalized envelope is $a(0)/\sqrt{\varepsilon S} \cong 3.25$. Forty one and twenty nine test particles are loaded uniformly at $s = s_0 = 0$ in the intervals $-2.0 \le x' \le 2.0$ and $-1.32 \le x' \le 1.32$ along the x' - axis in Figs. 3.1(a) and 3.1(b), respectively.

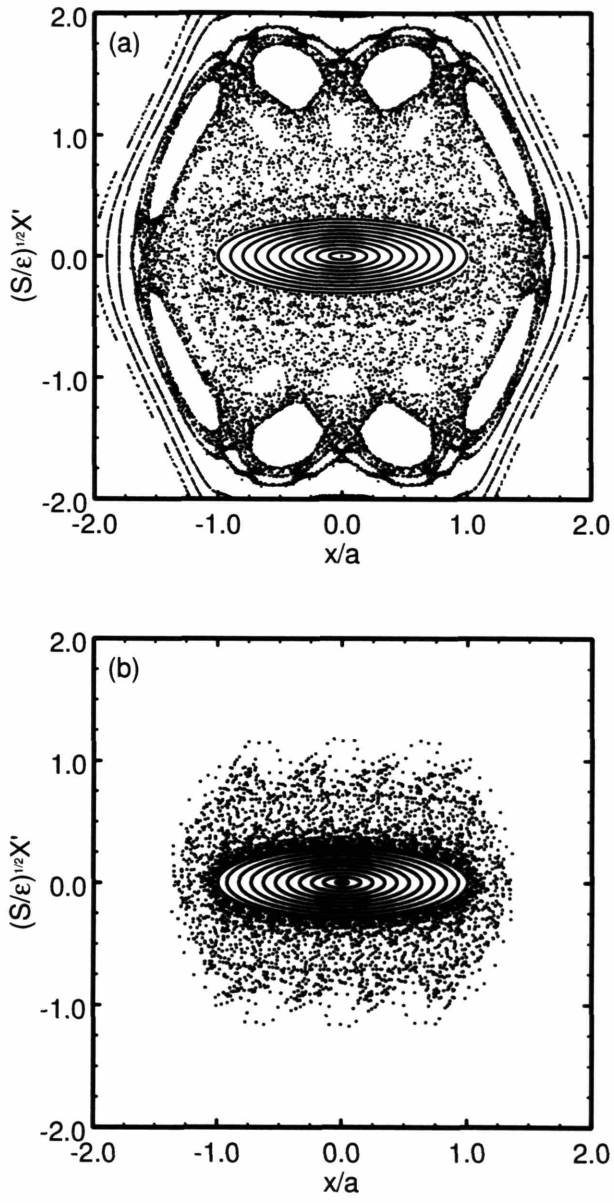

Figure 3.1 Poincaré surface-of section plots of test particles propagating over 1000 lattice periods in the phase plane (x, x') for two cases: (a) free-space $\hat{R} = \infty$ and (b) $\hat{R} = 4.5$. The system parameters are chosen to be $\eta = 0.5$, $\sigma_v = 80.0°$, $KS/\varepsilon = 10.0$ and $\varepsilon_x = \varepsilon_y = \varepsilon$. Forty one and twenty nine test particles are loaded uniformly at $s = s_0 = 0$ in the intervals $-2.0 \le x' \le 2.0$ and $-1.32 \le x' \le 1.32$ along the x'- axis in (a) and (b), respectively.

Because all of the test particles have $(y(0), y'(0)) = 0$, their trajectories remain in the phase plane (x, x'). As shown in Fig. 3.1 (a), well inside the beam with $W_x \leq 1$ the motion is regular, whereas there is a chaotic sea bounded between $W = 1$ and an outer Kolmogorov-Arnold-Moser (KAM) surface [39] at $x/a = 1.7$ for the free-space case with $\hat{R} = \infty$. This chaotic sea is fully connected; that is, a particle in the chaotic sea will fill out the entire region if it travels for a sufficiently long distance. As the conducting pipe radius R decreases, the conductor wall intersects the chaotic sea as shown in Fig. 3.1 (b), in which case the particles in the chaotic sea will eventually strike the wall.

It should be pointed out that as the conducting pipe radius R decreases, the image effect on the dynamics of a beam with the KV distribution is subtle, as illustrated in Fig. 3.2. In Fig. 3.2 the transverse energy $W_x(s) = (x/a)^2 + (ax'/\varepsilon)^2$ is plotted as a function of the axial distance s for 50 test particles loaded at $s = s_0 = 0$ on the beam boundary $W_x(0) = 1$ in the phase space with the initial phases $\phi_0 = \tan^{-1}\left[(S/\varepsilon)^{1/2} a(0)x'(0)/x(0)\right]$ uniformly distributed from 0 to $\pi/2$ for two cases: (a) free-space ($\hat{R} = \infty$) and (b) $\hat{R} = 4.5$. The system parameters are chosen to be the same as in Fig. 3.1. For the free-space case, the motion is stable, and the transverse energy is conserved for all of the test particles. As $\hat{R}$ decreases to $\hat{R} = 4.5$, some test particles become chaotic due to the nonlinear force of the induced image charge on the wall, and the transverse energies of these particles are no longer constant. As a result, these particles can gain energy and escape from the beam interior into the chaotic sea, striking the wall eventually. Figure 3.2(b) shows that some of these particles can form halo in less than 100 lattice periods and hit the wall in 300 to 400 lattice periods.

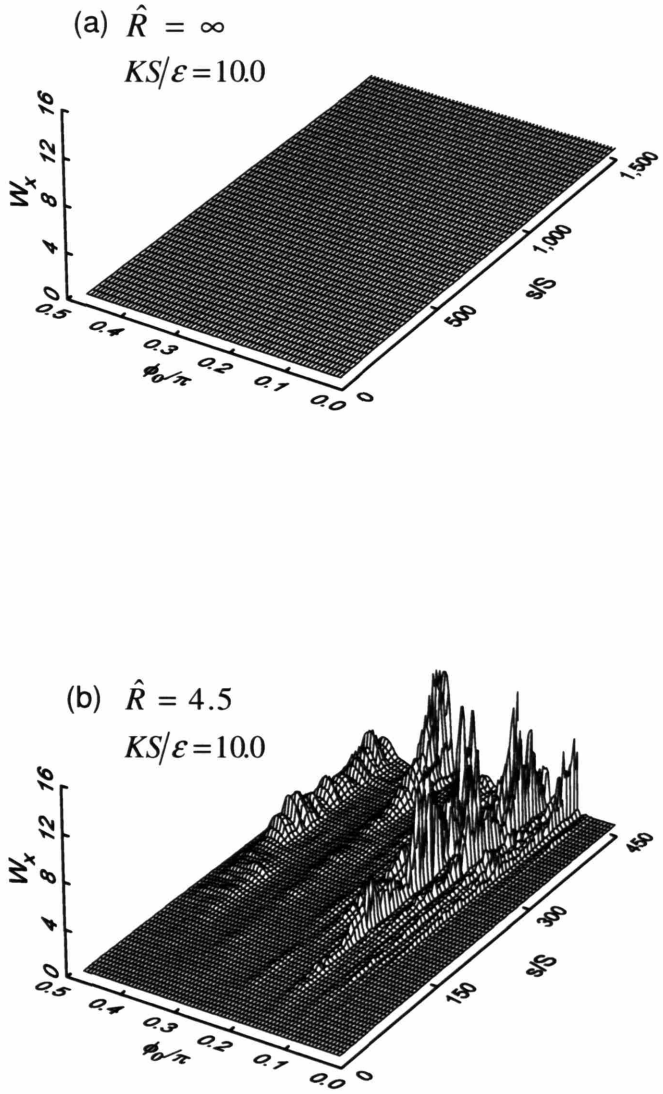

Figure 3.2 Plots of W_x vs s for 50 test particles in two cases: (a) free-space ($\hat{R} = R/\sqrt{\varepsilon S} = \infty$) and (b) $\hat{R} = 4.5$. The system parameters are the same as in Fig. 3.1. The test particles are initially loaded uniformly at $s = s_0 = 0$ with phase ϕ_0 ranging from 0 to $\pi/2$ on the beam boundary $[x(0)/a(0)]^2 + [a(0)x'(0)/\varepsilon]^2 = 1$ in the phase space.

In order to determine the outermost Kolmogorov-Arnold-Moser (KAM) surface of the beam core as illustrated in Fig. 3.1, the range of W for various initial conditions is plotted on the plane $(W_x, x/a)$. In Fig. 3.3, the range of transverse energy $W_x = x^2/a^2 + (ax' - xa')^2/\varepsilon^2$ is plotted for test particles propagating over 2000 lattice periods for two cases: (a) free-space ($\hat{R} \equiv R/\sqrt{\varepsilon S} = \infty$) and (b) $\hat{R} = 3.8$. The system parameters are chosen to be the same as in Fig. 3.1. The 115 test particles are loaded uniformly at $s = s_0 = 0$ in the interval $0 \le W_x \le 1.15$ along the x'- axis. As shown in Fig. 3.3(a), the outermost Kolmogorov-Arnold-Moser (KAM) surface for the beam core in the free space case is located at $x/a = 1.03$ which is slightly outside the beam boundary. There is a continuum of KAM surfaces for $x(0)/a(0) \le 1.03$, where W_x is conserved. The particles inside the beam core have regular motion and cannot escape to form a halo. As the conducting pipe radius R decreases, the conductor wall intersects the chaotic sea. Furthermore, the image force induced by the conductor wall becomes important and the KAM surface for the beam core moves inside the beam interior, reaching $x/a = 0.96$, as shown in Fig. 3.3(b) for $\hat{R} = 3.8$. In this case some particles inside the beam core will escape to form a halo and eventually strike the wall.

The locations and evolution of the chaotic particles are illustrated in Fig. 3.4, where the transverse energy W_x is plotted for 2000 test particles loaded at $s = 0$ on the beam boundary $W_x(0) = 1$ in the phase space with the initial phases $\phi_0 = \tan^{-1}\left[(S/\varepsilon)^{1/2} a(0)x'(0)/x(0)\right]$ uniformly distributed from 0 to 2π for the same system parameters as in Fig. 3.1(b). Those test particles with initial phases in the intervals $0 \le \phi_0 \le 0.1\pi$, $0.9\pi \le \phi_0 \le 1.1\pi$, and $1.9\pi \le \phi_0 \le 2\pi$ are regular and remain inside the beam with $W_x \cong 1$. The other test particles are chaotic and gain energy. Some of the chaotic particles in Fig. 3.4 strike the wall after tens of periods. An example

of such a chaotic particle is illustrated in comparison with a core particle in Fig. 3.5, where W_x is plotted as a function of s for two test particles with initial phases: (a) $\phi_0/\pi = 0$ and (b) $\phi_0/\pi = 0.35$, which correspond to a halo particle and a core particle, respectively.

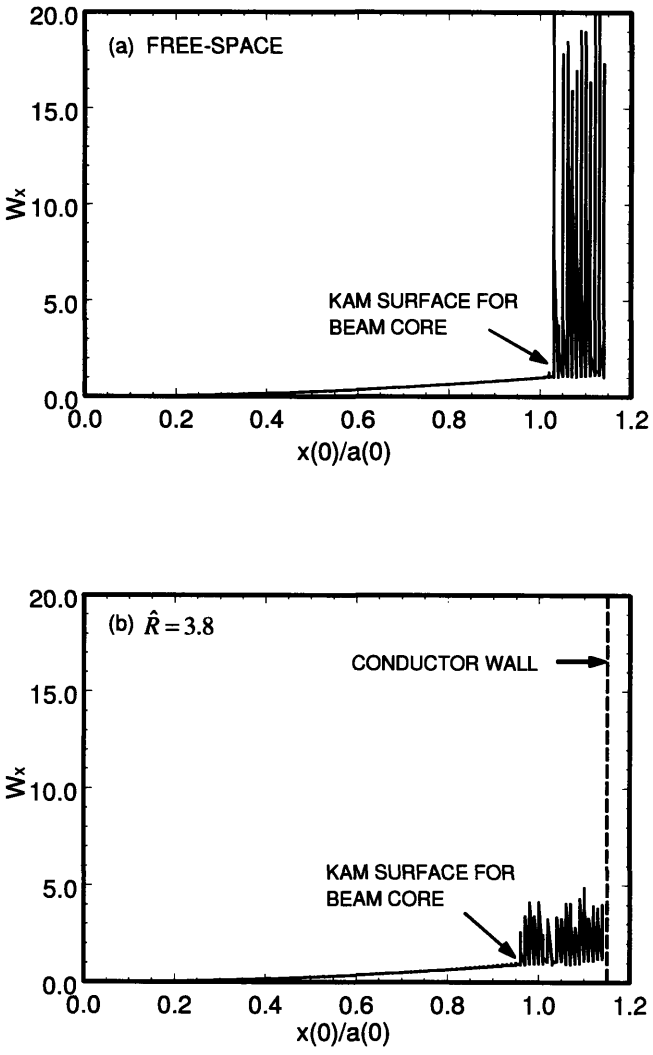

Figure 3.3 Plots of the range of W_x for test particles propagating over 2000 lattice periods for two cases: (a) free-space $\hat{R} = \infty$ and (b) $\hat{R} = 3.8$. The system parameters are chosen to be $\eta = 0.5$, $\sigma_v = 80.0°$, $KS/\varepsilon = 10.0$ and $\varepsilon_x = \varepsilon_y = \varepsilon$. The 115 test particles are loaded uniformly at $s = s_0 = 0$ in the interval $0 \le W_x \le 1.15$ along the x' axis in phase space.

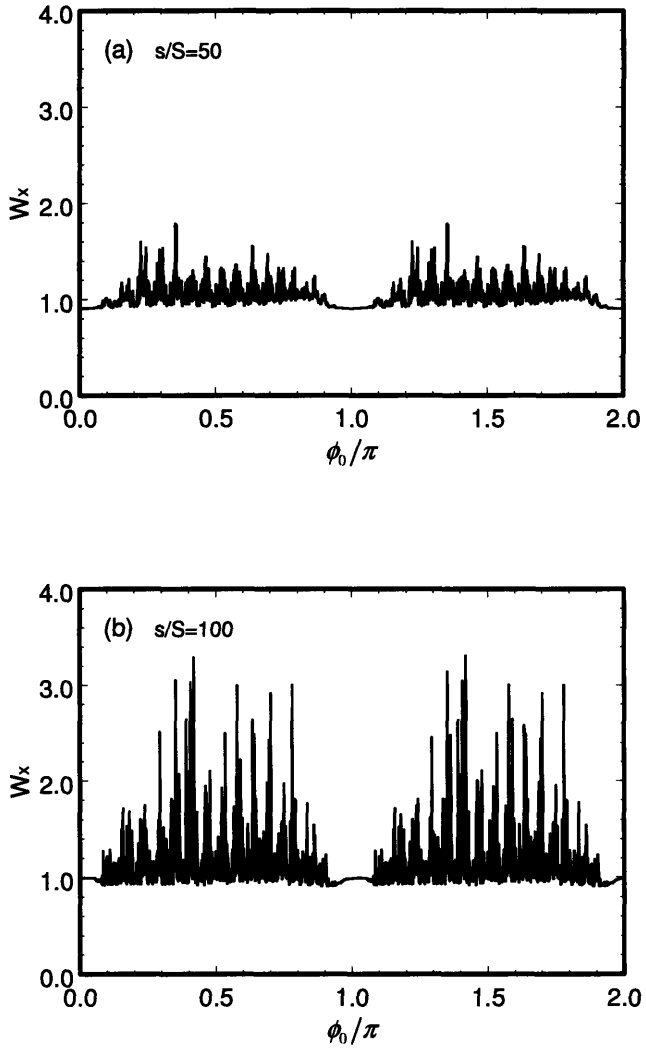

Figure 3.4 Plots of W_x for 2000 test particles with the same system parameters as in Fig. 3.1(b) at two axial locations (a) $s/S = 50$ and (b) $s/S = 100$. The test particles are initially loaded uniformly at $s = s_0 = 0$ with phase ϕ_0 ranging from 0 to 2π on the beam boundary $W_x(0) = [x(0)/a(0)]^2 + [a(0)x'(0)/\varepsilon]^2 = 1$ in the phase space.

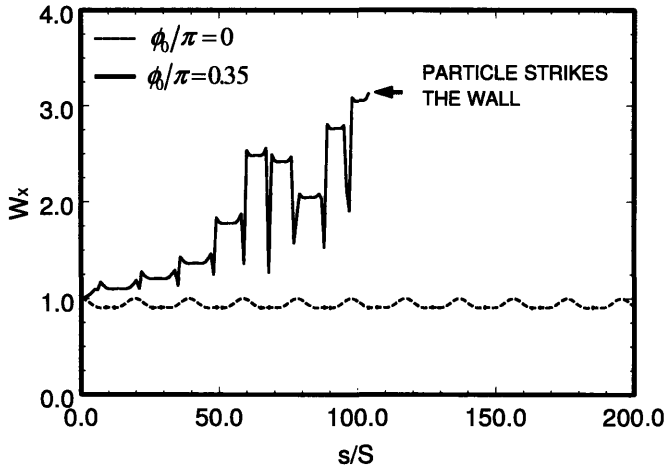

Figure 3.5 Plots of W_x vs s for two test particles with initial phases (a) $\phi_0/\pi = 0$ and (b) $\phi_0/\pi = 0.35$ for the same system parameters as in Fig. 3.1(b).

3.4 Parametric studies

In this section, we study the sensitivity of chaotic particle motion, halo formation and beam loss on the system parameters: the filling factor of the quadrupole focusing field, the vacuum phase advance, the beam perveance, and the ratio of the beam size to the aperture. Furthermore, we calculate the percentage of beam loss to the conductor wall as a function of propagating distance and aperture.

As the vacuum phase advance σ_v decreases, the regular region of particle motion decreases, which means that for smaller vacuum phase advance σ_v more particles are in the chaotic sea and can form halo. As shown in Fig. 3.6 the outermost KAM surface location relative to the beam

boundary decreases with increasing vacuum phase advance for two cases: (a) $a/R = 80\%$ and (b) $a/R = 85\%$ with $\eta = 0.5$, $KS/\varepsilon_x = 10.0$, and $\varepsilon_x = \varepsilon_y = \varepsilon$.

However, the rate of the halo production decreases as the vacuum phase advance decreases. The locations and evolution of the chaotic particles are illustrated in Fig. 3.7, where the transverse energy $W_x(s/S = 50)$ is plotted for 2000 test particles loaded initially at $s = s_0 = 0$ on the beam boundary $W_x(0) = 1$ in the phase space with the initial phases $\phi_0 = \tan^{-1}\left[(S/\varepsilon)^{1/2} a(0)x'(0)/x(0)\right]$ uniformly distributed from 0 to 2π for two cases: (a) $\sigma_v = 60°$ and (b) $\sigma_v = 80°$. Those regular particles remain inside the beam with $W_x \cong 1$, while the other test particles are chaotic and gain energy with $W_x > 1$. At $s/S = 50$, Fig. 3.7 shows that more halo forms with $W_x > 1$ at $\sigma_v = 80°$ compared with the situation at $\sigma_v = 60°$.

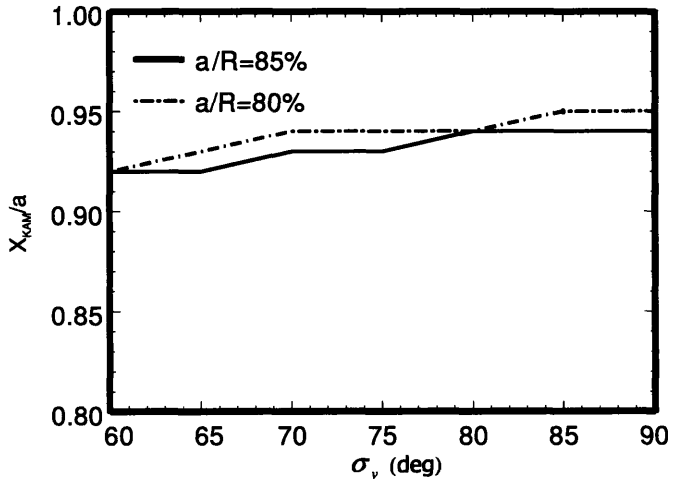

Figure 3.6 Plots of the outermost KAM surface location X_{KAM}/a of the beam core as a function of the vacuum phase advance σ_v for $\eta = 0.5$, $KS/\varepsilon = 10.0$, $\varepsilon_x = \varepsilon_y = \varepsilon$, and two cases: (a) $a/R = 80\%$ and (b) $a/R = 85\%$.

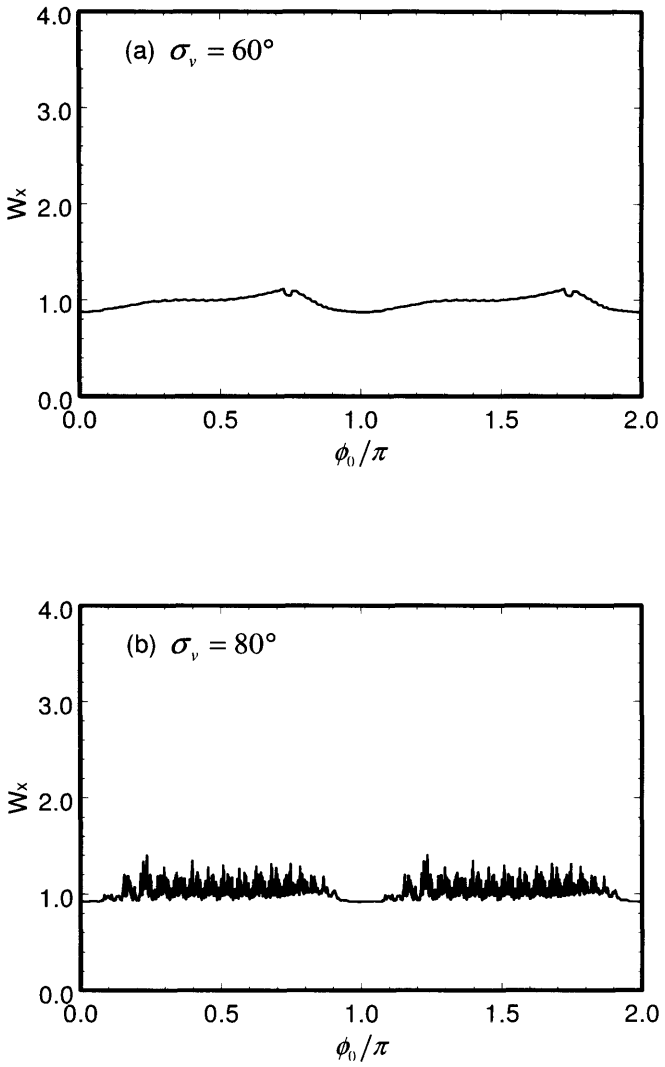

Figure 3.7 Plots of W_x vs ϕ_0 for 2000 test particles at axial distance $s/S = 50$ for $\eta = 0.5$, $KS/\varepsilon = 10.0$, $\varepsilon_x = \varepsilon_y = \varepsilon$, and two cases: (a) $\sigma_v = 60°$, and (b) $\sigma_v = 80°$. The test particles are initially loaded uniformly at $s = s_0 = 0$ with phase ϕ_0 ranging from 0 to 2π on the beam boundary $W_x(0) = 1$ in the phase space.

Figures 3.8 and 3.9 show the dependence of halo formation and chaotic particle motion on the filling factor of the quadrupole focusing field. As the filling factor of the quadrupole focusing field decreases, the regular region of particle motion decreases, which means that for smaller filling factor of the quadrupole focusing field more particles are in the chaotic sea. However, the rate of the halo production decreases as the filling factor of the quadrupole focusing field decreases. This is illustrated in Fig. 3.9 where the halo for $\eta = 0.2$ is more pronounced than that for $\eta = 0.8$ at $s/S = 50$.

Figures 3.10 and 3.11 show the dependence of halo formation and chaotic particle motion on the beam perveance. As the perveance increases, the regular region of particle motion decreases, which means that for high intensity beam, more particles are in the chaotic sea. The rate of the

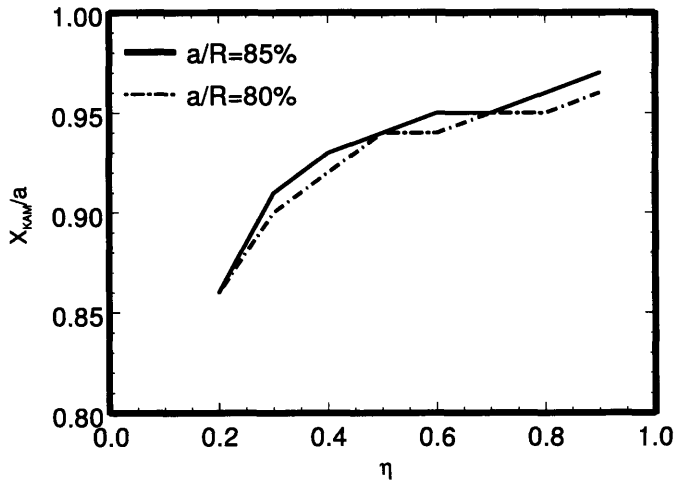

Figure 3.8 Plots of the outermost KAM surface location X_{KAM}/a of the beam core as a function of the filling factor of the quadrupole focusing field η, for $KS/\varepsilon = 10.0$, $\varepsilon_x = \varepsilon_y = \varepsilon$, $\sigma_v = 80°$ and two cases: (a) $a/R = 80\%$ and (b) $a/R = 85\%$.

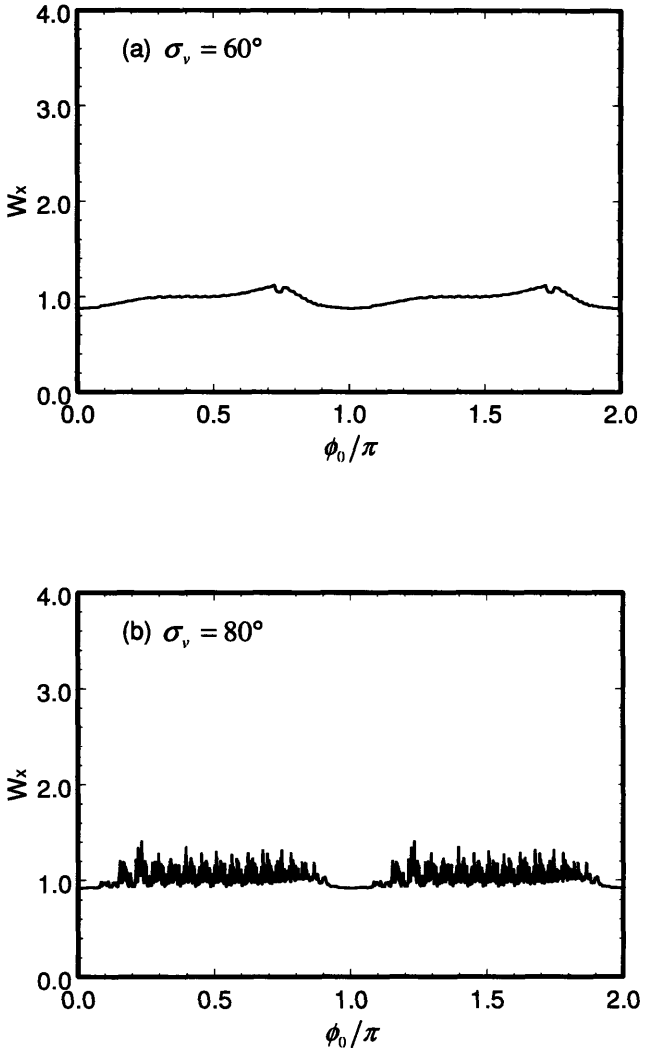

Figure 3.9 Plots of W_x vs ϕ_0 for 2000 test particles at axial distance $s/S = 50$ for $KS/\varepsilon = 10.0$, $\varepsilon_x = \varepsilon_y = \varepsilon$, $\sigma_v = 80°$ and two cases: (a) $\eta = 0.2$ and (b) $\eta = 0.8$. The test particles are initially loaded uniformly at $s = s_0 = 0$ with phase ϕ_0 ranging from 0 to 2π on the beam boundary $W_x(0) = 1$ in the phase space.

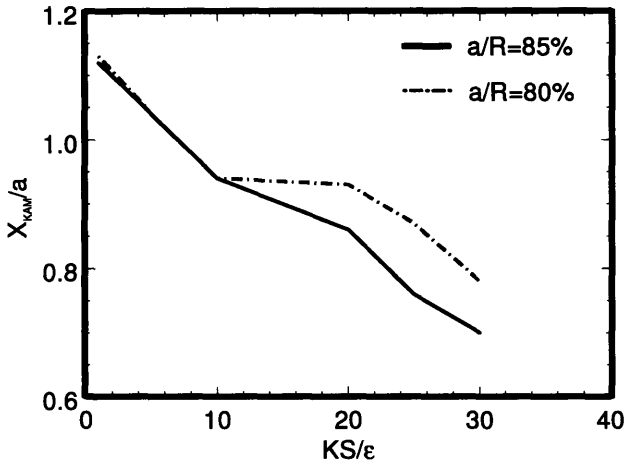

Figure 3.10 Plots of the outermost KAM surface location X_{KAM}/a of the beam core as a function of the scaled perveance $\hat{K} = KS/\varepsilon$ for $\eta = 0.5$, $\varepsilon_x = \varepsilon_y = \varepsilon$, $\sigma_v = 80°$ and two cases: (a) $a/R = 80\%$ and (b) $a/R = 85\%$.

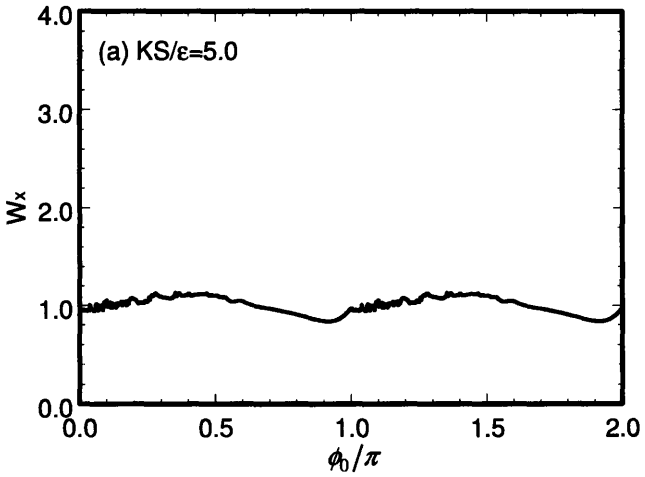

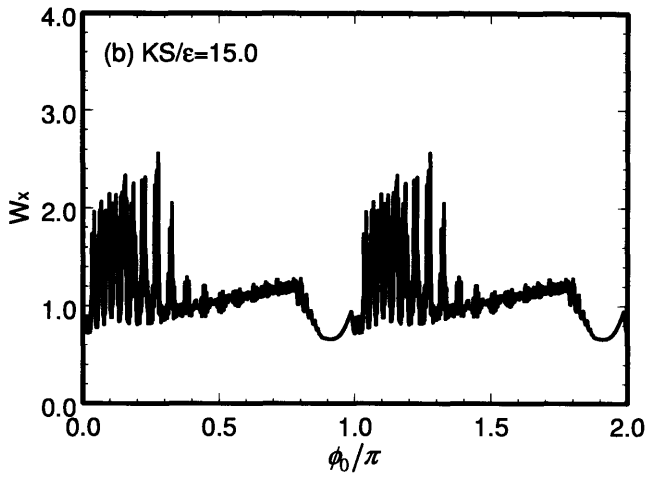

Figure 3.11 Plots of W_x vs ϕ_0 for 2000 test particles at axial distance $s/S = 50$ for $\eta = 0.5$, $\sigma_v = 80°$, $\varepsilon_x = \varepsilon_y = \varepsilon$, $a/R = 85\%$ and two cases: (a) $KS/\varepsilon_x = 5.0$, and (b) $KS/\varepsilon_x = 15.0$.

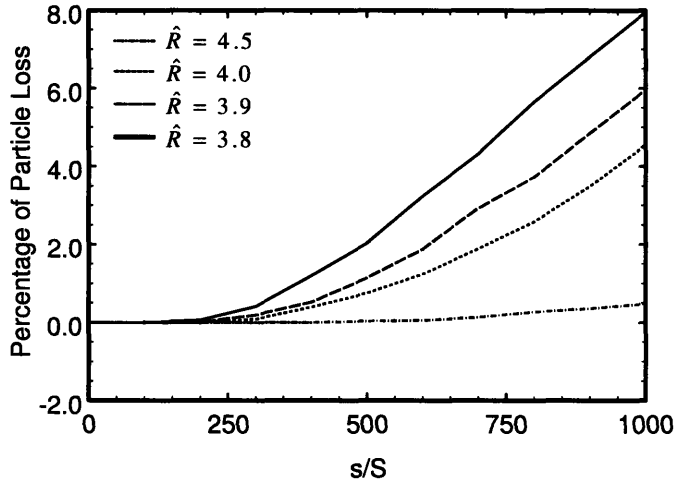

Figure 3.12 Plots of the percentage of particles striking the conductor wall as a function of propagation distance for $\eta = 0.5$, $\sigma_v = 80.0°$, $KS/\varepsilon = 10.0$, $\varepsilon_x = \varepsilon_y = \varepsilon$ and several choices of $\hat{R} \equiv R/\sqrt{\varepsilon S}$. Here, 10000 test particles with the KV distribution initially are used in the simulations.

halo production increases as the beam intensity increases. This is illustrated in Fig. 3.11 where the halo for $KS/\varepsilon_x = 15.0$ is more pronounced than that for $KS/\varepsilon_x = 5.0$ at $s/S = 50$.

Finally, the beam loss is computed as a function of propagation distance and conducting pipe radius. As an example, the results are shown in Fig. 3.12 for $\eta = 0.5$, $\sigma_v = 80.0°$, $KS/\varepsilon = 10.0$, $\varepsilon_x = \varepsilon_y = \varepsilon$, $\sigma_v = 80°$, and four choices of the conducting pipe radius with $\hat{R} \equiv R/\sqrt{\varepsilon S} = 3.8$, 3.9, 4.0, and 4.5. The critical value of $\hat{R}$ for the outermost KAM surface adjacent to the beam core to penetrate the beam is estimated to be $\hat{R} = 5.5$; that is, $X_{KAM} = a$ at $\hat{R} = 5.5$. In another words, when the pipe radius is chosen to be bigger than $\hat{R} = 5.5$ i.e., $a/R = 60\%$, no beam loss occurs. The beam loss rate increases with the decreasing pipe radius, where the image effects play a more important role in the total space charge force. When the maximum beam envelope fills 86% of the conducting pipe, the beam loss reaches 8% at $s = 1000S$. Although the results shown in Fig. 3.12 are based on the test-particle calculations, they provide order of magnitude estimates for the actual beam losses, which are being studied using self-consistent simulations [31][38] (also see Sec. 4.3).

3.5 Summary

We have shown, using the test-particle model in a small-aperture alternating-gradient focusing system, that image-charge effects induce a new mechanism for chaotic particle motion, halo formation, and particle loss in intense charged-particle beams. This mechanism occurs for well-matched beams with the ideal Kapchinskij-Vladimirskij (KV) distribution. The halo formation and beam loss are sensitive to the choices of system parameters: the filling factor of the

quadruple focusing field, the vacuum phase advance, the perveance, and the conducting pipe radius.

As shown in our parametric studies, the beam loss increases rapidly as the perveance of the beam increases or as the conducting pipe radius decreases. This demonstrates that in the current configuration, halo formation and beam loss is intrinsic of the nonlinear space-charge forces in high-intensity charged-particle beams focused by the alternating-gradient focusing fields in small-aperture systems. In order to eliminate halo formation and beam loss in high-intensity charged-particle beams, one could change the system configuration to reduce the nonlinear space-charge forces while still maintaining the high intensities of the beams.

Chapter 4

Particle-In-Cell (PIC) Simulations

4.1 Introduction

The complex nature of the problems encountered in plasma physics and accelerator physics has motivated considerable interest in computer simulation, which has played an essential role in the development of plasma theory. In addition, computer simulation is also becoming an efficient design tool to provide accurate performance predictions in plasma physics applications.

In non-neutral plasma physics, computer simulations are based on kinetic description involving particle interactions with the electromagnetic field. The simulation model is established either by solving numerically the plasma kinetic equations (e.g. Vlasov or Fokker-Plank equations) or by "particle" simulation, which simply computes the motions of a collection of charged particles, interacting with each other and with externally applied fields.

The pioneering work of Dawson and others [40]-[43] in the early 60's has shown that, when appropriate methods are used, relatively small systems of a few thousand particles can indeed simulate accurately collective behavior of a real plasma. Since then, the development of new algorithms and the availability of more powerful computers, especially, parallel computation which employs thousands of computer processors, have allowed particle simulation to progress from simple, one-dimensional, electrostatic problems to more complex and realistic situations, involving electromagnetic fields in multiple dimensions and up to millions of particles.

There have been extensive efforts to develop large scale, multi-dimensional, parallel and realistic particle simulation codes for beam simulations at national laboratories and in industries in United State, such as Track3P at Stanford Linear Accelerator Center (SLAC) [44], WARP3D

at Lawrence Berkeley National Laboratory (LBNL) and Lawrence Livermore National Laboratory (LLNL) [45], ICEPIC at Airforce Research Laboratory, MAGIC at Mission Research Corp. (MRC) [46], and VORPAL at Tech-X Corporation at Boulder Colorado [47].

In this chapter, the development of a two-dimensional electrostatic PIC code, Periodically Focused Beam (PFB2D) at Massachusetts Institute of Technology (MIT), is discussed. The PFB2D code is used to simulate intense charged-particle beams in small-aperture alternating-gradient systems which were investigated theoretically in Chapters 2 and 3. The envelope dynamics and test-particle dynamics in Chapters 2 and 3 were based on a self-similar model in which the particles do not interact with each other, therefore, the beam distribution does not evolve self-consistently. The present PIC simulations include those interactions and allow the beam distribution to evolve according to the self and applied focusing fields. Despite the numerical errors and noise in the PIC simulations, the PIC model does represent a more realistic model of the actual system. However, in the PIC simulation studies of halo formation and beam loss, the numerical noise makes it difficult to distinguish the difference between the noise and halo formation and beam loss. The beam loss predicted by the PIC simulations is an order of magnitude higher than that predicted by theory. In order to estimate the noise in the PIC simulations, particle diffusion due to discrete macro-particle effects is analyzed [48]. In particular, an error scaling law is derived which gives the edge emittance growth due to discrete macro-particle effects. Moreover, the scaling law is tested in Green's function simulation and the PIC simulations. Implications of the error scaling law in the PIC simulation studies of halo formation and beam loss are discussed.

This chapter is organized as follows. In Sec. 4.2, the algorithms of the PFB2D code are presented. In Sec. 4.3, the PFB2D simulation results of intense charged-particle beams in small-

aperture alternating-gradient systems are discussed and compared to the theoretical results from the test-particle model. In Sec. 4.4, the noise and particle diffusion due to discrete macro-particle effects is analyzed. In Sec. 4.5, a brief summary is given.

4.2 Description of the PIC PFB2D code

The system under discussion involves charged particle dynamics in both applied and self-generated fields. The physics comes from two parts: the fields produced by the charged particles and external electrodes or magnets, and the motion produced by the Lorentz force. The fields are calculated from Maxwell's equations by knowing the positions of all of the charged particles and their velocities. The PFB2D code calculates the fields from the initial charge and current densities, then moves the charged particles by some small distances in a small time step. It recalculates the fields due to the particles at their new positions and new velocities. This procedure is repeated for many small time steps.

The main differences between a laboratory plasma and a simulated plasma are that the fields are computed on a spatial grid in the PFB2D simulations instead of as a continuous function, and that the charged particles move discontinuously in time step by step. At each step in time, the PFB2D code solves for the fields from the charged particles and then moves the charged particles in a cycle, shown in Figure 4.1. In the PFB2D code the axial distance plays the role of "time". The cycle starts at $s = 0$, with some appropriate initial conditions on the charged particles' positions $\mathbf{x}_i$ and velocities $\mathbf{v}_i$. An example of the KV beam loading will be discussed in Sec 4.2.1. The fields will be obtained only on the spatial grid in the plane (x, y). Typically, the spatial grids are 32×32 to 512×512. The maximum number of grid points depends on the machine's capacity. The fields are computed by first calculating the charge and current densities

on the grid according to the charged particle positions and velocities with a certain weighting scheme, which will be discussed in Sec. 4.2.3. Once the densities are established on the grid, then Poisson's equation can be solved using finite-different method to obtain the electric field and magnetic field. With the fields known on the grid, we interpolate the fields from the grid to the charged particles' positions in order to apply the forces at the charged particles performing a weighting. Finally, the charged particles are moved to the next time step according to the Lorentz force.

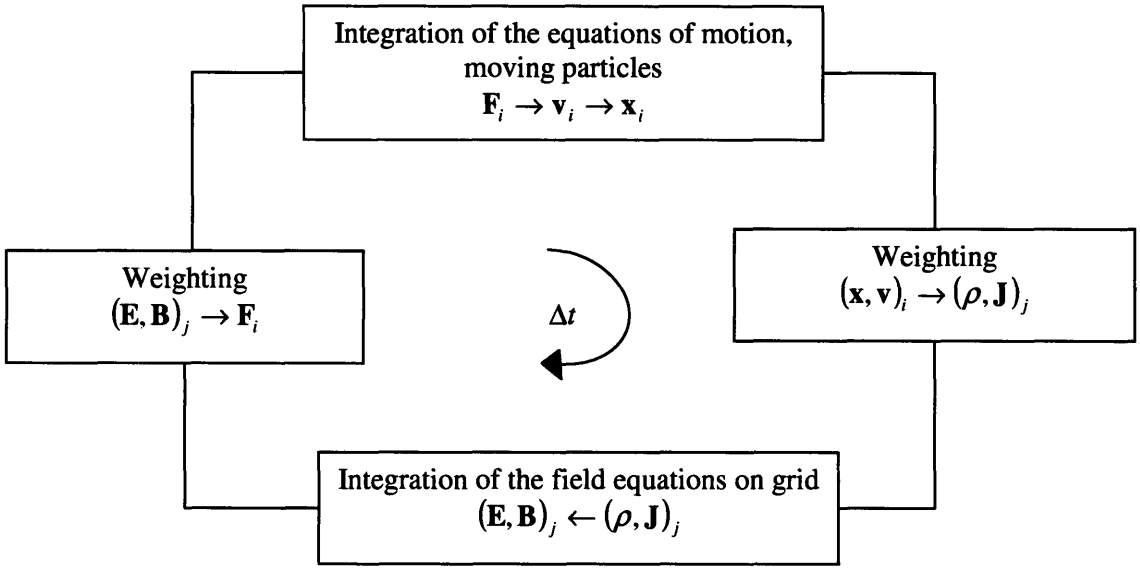

Figure 4.1 A typical one-time-step cycle in a PFB2D simulation. The charged particles are numbered with $i = 1, 2, ..., N_p$; the grid indices are j, which is a vector in 2 dimensions.

4.2.1 Initial particle loading

The charged particles have to be loaded carefully according to some desirable particle distribution $f(\mathbf{x}, \mathbf{v})$ in phase space. The number of particles N_p loaded has to be large enough to make the density variations relatively smooth, implying that there have to be, on average, a few particles per cell where the beam resides.

For example, the initial loading distribution for a KV beam is described as [8]

$$f_b(x, y, x', y', s_0) = \frac{N_b \delta(W-1)}{\pi^2 \varepsilon_x \varepsilon_y}, \tag{4.1}$$

where $x' = dx/ds$, and W is the variable defined by

$$W = \frac{x^2}{a^2} + \frac{(ax' - xa')^2}{\varepsilon_x^2} + \frac{y^2}{b^2} + \frac{(by' - yb')^2}{\varepsilon_y^2}. \tag{4.2}$$

Here, a, a', b, and b' denote the "initial" rms envelope values at $s = s_0$. The particles' locations and velocities are generated from the uniform distributed random variables defined by

$$x = aR_1 \cos(2\pi R_2), \tag{4.3}$$

$$y = b\sqrt{1 - R_1^2} \cos(2\pi R_3), \tag{4.4}$$

$$x' = \frac{\varepsilon_x}{a} R_1 \sin(2\pi R_2) + a' R_1 \cos(2\pi R_2), \tag{4.5}$$

$$y' = \frac{\varepsilon_y}{b}\sqrt{1 - R_1^2} \sin(2\pi R_3) + b'\sqrt{1 - R_1^2} \cos(2\pi R_3), \tag{4.6}$$

where R_1, R_2 and R_3 are independent, uniformly distributed random variables in the interval $[0, 1]$. It is readily to shown that substituting Eqs. (4.3)-(4.6) into Eq. (4.2) yields $W = 1$.

4.2.2 Boundaries and uniform rectangular mesh

In the PFB2D code, the longitudinal coordinate is divided into slices uniformly along z axis. The spatial grid is uniformly meshed on each slice in the transverse (x, y) plane, as illustrated in Fig. 4.2. The self fields are obtained from the charge density and current density on grid points ($x_j = i\Delta x$, $y_k = k\Delta y$). The mesh size is $\Delta x \times \Delta y$, which has to be made small enough to resolve the details deemed necessary and to avoid numerical troubles (with a warm plasma, keeping at least $\Delta x > 3\lambda_D$, where λ_D is the Debye length).

In real systems, we have boundaries which might take irregular geometries. As shown in Fig. 4.2, a commonly used boundary is a cylindrical perfect conducting pipe which is grounded and has zero electric potential. Therefore, the grid points that are close to the boundary have to be assigned zero potential. There are two methods to do the assignment for such a uniform mesh. In the first method, we can assign zero potential to the grid points which are immediately outside the cylindrical pipe. The other method is to assign zero potential to the grid points which are closest to the cylindrical conducting pipe, which can be either outside or inside the pipe. The second method is more accurate than the first method but it is more computationally intensive than the first one. In the PFB2D, the first method is implemented.

4.2.3 Weighting and effective particle shapes

The assignment of a particle charge to its neighboring grid points proceeds with the zero-order [nearest-grid-point (NGP)] weighting, the first order (area) weighting, and higher-order weighting.

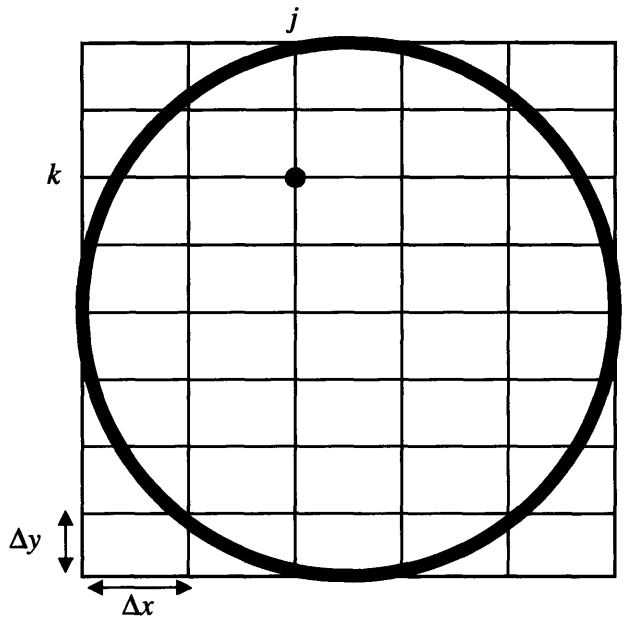

Figure 4.2 Circular conducting pipe under a uniform rectangular mesh in the transverse (x, y) space. The mesh size is $\Delta x \times \Delta y$.

The zeroth-order (NGP) weighting to one grid point is the simplest. The particle charge assignment on a grid point is obtained by counting the number of particles within the rectangular area of Δx by Δy centered at the grid point. The particle shape is a rectangular cloud of height 1 and size Δx by Δy as sketched in Fig. 4.3. The force between two grid points is discontinous which leads to noise and self-heating, but becomes close to the physical $1/r$ dependence at large separation of two charge clouds. For these reasons, the zeroth-order weighting (NGP) is seldom used.

The first-order weighting is usually called area weighting due to its geometric interpretation, as shown in Fig. 4.4. It is still a linear interpolation. The weights are given by

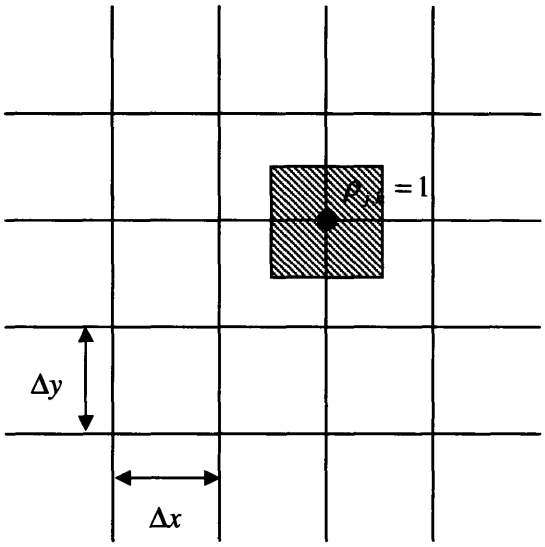

Figure 4.3 Particle shape for the zeroth-order (NGP) weighting in 2D, which is uniform inside the shaded area of size $\Delta x \times \Delta y$ and centered at the grid point.

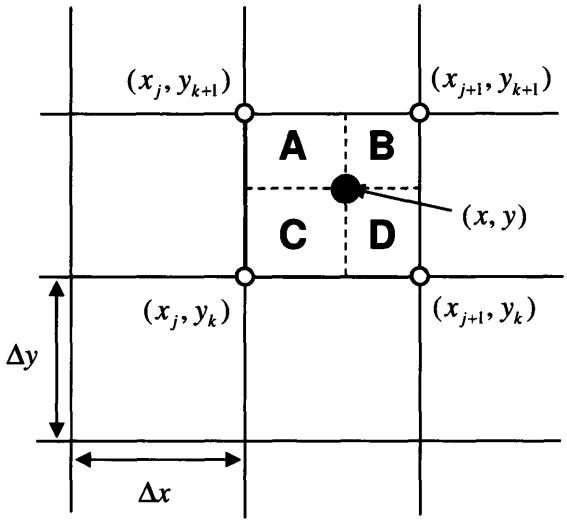

Figure 4.4 Illustration of the first-order weighting in 2D. Areas are assigned to grid points: Area A to the grid point (x_{j+1}, y_k), Area B to the grid point (x_j, y_k), Area C to the grid point (x_{j+1}, y_{k+1}) and Area D to the grid point (x_j, y_{k+1}).

$$\rho_{j,k} = \rho \frac{Area(B)}{Area(A+B+C+D)} = \rho \frac{[x_{j+1} - x][y_{k+1} - y]}{\Delta x \Delta y}, \tag{4.7}$$

$$\rho_{j+1,k} = \rho \frac{Area(A)}{Area(A+B+C+D)} = \rho \frac{[x - x_j][y_{k+1} - y]}{\Delta x \Delta y}, \tag{4.8}$$

$$\rho_{j,k+1} = \rho \frac{Area(D)}{Area(A+B+C+D)} = \rho \frac{[x_{j+1} - x][y - y_k]}{\Delta x \Delta y}, \tag{4.9}$$

$$\rho_{j+1,k+1} = \rho \frac{Area(C)}{Area(A+B+C+D)} = \rho \frac{[x - x_j][y - y_k]}{\Delta x \Delta y}, \tag{4.10}$$

where ρ is the line charge density of a (line) charge at point (x, y), and $\rho_{j,k}$ are the weights associated with the charge at its adjacent grid points.

Effectively, the area weighting scheme introduces a shaped particle with a gradually decreasing "density" distribution. The particle shape can be obtained by measuring the charge assigned to a grid point as the particle moves relative to that point. The particle contours are shown in Fig. 4.5, indicating an improvement over the flat, rectangular NGP particle. As a result, the area weighting scheme reduces the noise and the self-heating relative to NGP.

In the PFB2D simulations, the area weighting scheme is used because it has reduced noise and self-heating as long as the particle density is kept large enough, usually a few particles per cell, and it is less computationally expensive than higher-order weighting schemes.

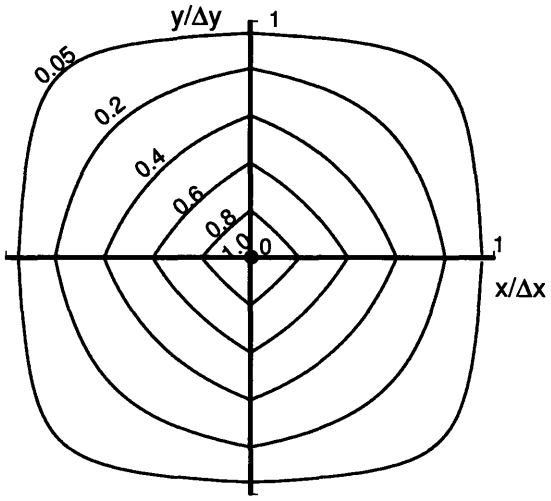

Fig. 4.5 Particle density contours as seen by the center grid point in area weighting in 2D. The total particle are is $4\Delta x\Delta y$.

4.2.4 Solutions of Poisson's equation with boundary conditions

The Poisson's equation is solved using a finite-difference method on the spatial grid. The Poisson's equation for a 2D continuous beam inside a perfect conducting cylindrical pipe is expressed as

$$\left(\frac{\partial^2}{\partial x^2}+\frac{\partial^2}{\partial y^2}\right)\phi=-4\pi qn(x,y), \tag{4.11}$$

$$\phi|_{boundary}=0. \tag{4.12}$$

In the finite difference form, this becomes the five-point form

$$\frac{\phi_{j+1,k}-2\phi_{j,k}+\phi_{j-1,k}}{\Delta x^2}+\frac{\phi_{j,k+1}-2\phi_{j,k}+\phi_{j,k-1}}{\Delta y^2}=-4\pi\rho_{j,k}, \tag{4.13}$$

$$\phi_{j,k}\Big|_{boundary} = 0, \tag{4.14}$$

for $j = 1, 2, 3, ..., N_g$ and $k = 1, 2, 3, ..., N_g$. Here, $N_g \times N_g$ is the total number of mesh cells, the potentials on the boundary were discussed in Sec. 4.2.2, and the charge density is obtained on grid points as discussed in Sec 4.2.3.

The finite difference form of the Poisson equation (4.13) can be written in the matrix form

$$\mathbf{A\varphi} = \boldsymbol{\rho} \tag{4.15}$$

with the boundary conditions. This is called the two-point boundary value problem [49], which is in general solved using relaxation methods. Iteration is in general required to meld these spatially scattered boundary conditions into a single global solution of the differential equations.

A trial solution consists of values for the dependent variables at mesh points, which neither satisfying the desired finite-difference equations nor fulfill the required boundary conditions. The iteration, also called relaxation, consists of adjusting all the values on the mesh so as to bring them successively closer in agreement with the finite-difference equations and, simultaneously, with the boundary conditions.

Good initial guesses are the secret of efficient relaxation methods. Often one has to solve a problem many times, each time with a slightly different value of the system parameters. In that case, the previous solution is usually a good initial guess when the parameter is slightly changed, and relaxation will work well.

There are number of relaxation methods. In the PFB2D code, the successive over relaxation (SOR) method is used. In the PFB2D code, Eq. (4.13) is modified to

$$a_{j,k}\phi_{j+1,k} + b_{j,k}\phi_{j-1,k} + c_{j,k}\phi_{j,k+1} + d_{j,k}\phi_{j,k-1} + e_{j,k}\phi_{j,k} = -4\pi\rho_{j,k}, \tag{4.16}$$

where $a_{j,k} = 1/\Delta x^2$, $b_{j,k} = 1/\Delta x^2$, $c_{j,k} = 1/\Delta y^2$, $d_{j,k} = 1/\Delta y^2$ and $e_{j,k} = -2/\Delta x^2 - 2/\Delta y^2$. The iterations start with an initial guess distribution φ^0, and the iteration is

$$\phi_{j,k}^{n+1} = \phi_{j,k}^{n} - \omega \frac{\zeta_{j,k}^{n}}{e_{j,k}^{n}}, \tag{4.17}$$

where the residual is defined as

$$\zeta_{j,k}^{n} = a_{j,k}^{n}\phi_{j+1,k}^{n} + b_{j,k}^{n}\phi_{j-1,k}^{n} + c_{j,k}^{n}\phi_{j,k+1}^{n} + d_{j,k}^{n}\phi_{j,k-1}^{n} + e_{j,k}^{n}\phi_{j,k}^{n} - 4\pi\rho_{j,k}^{n}, \tag{4.18}$$

and ω is the over-relaxation parameter. The over-relaxation parameter ω is geometry dependent. In practice, we optimize ω given a particular geometry. Finally, the iteration stops as $\zeta_{j,k}^{n}$ is less than a required error tolerance, typically 10^{-5}.

As a benchmark, the self-electric fields are calculated by using the SOR method discussed above for a uniform distributed elliptic beam inside a cylindrical perfect conducting pipe. As shown in Fig. 4.6, the normalized self-electric fields E_x and E_y on the grid points are plotted with marco-particles initially loaded uniformly inside an elliptic beam boundary $x^2/3.32^2 + y^2/2^2 = 1$, where the spacial mesh of 101×101 and 5000 maro-particles are used in the simulation. For comparison, the self-electric fields are calculated theoretically by differentiating Eq. (3.26) and (3.27), which are plotted in Fig. 4.7. There are excellent agreement between the numerical calculation and the analytic solution, although the numerical results have noises due to the discrete macro-particle charge and discrete spatial mesh which can not match the boundary exactly.

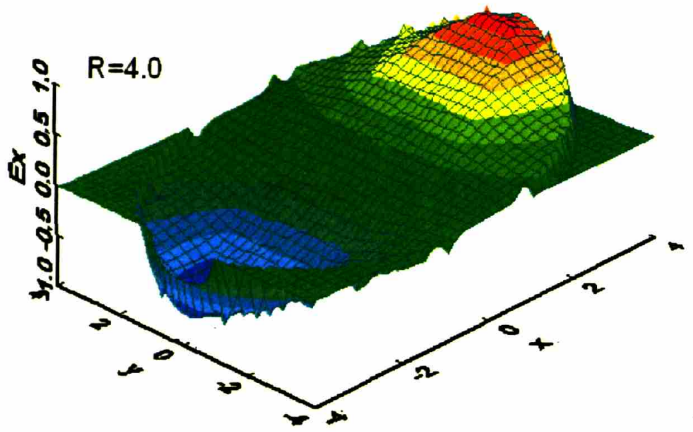

Fig. 4.6 (a)

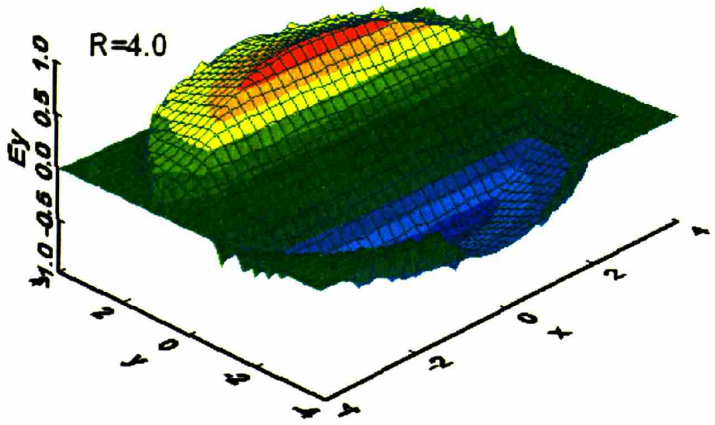

Fig. 4.6 (b)

Figure 4.6 Normalized self-electric field for a uniform 2D elliptic beam inside a cylindrical perfect conducting pipe with radius $R = 4.0$ obtained numerically from PFB2D: (a) E_x and (b) E_y.

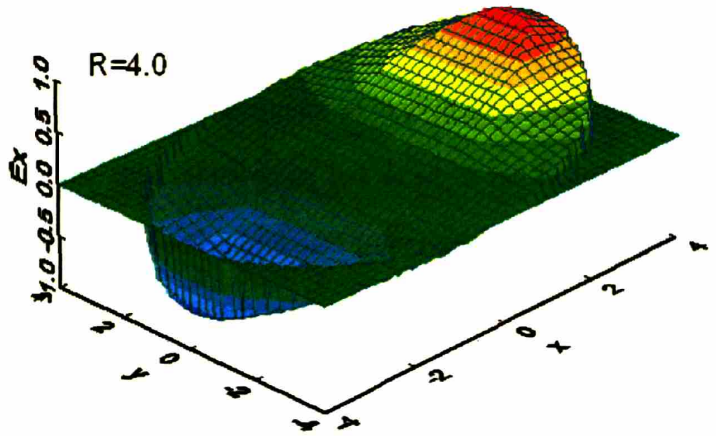

Fig. 4.7 (a)

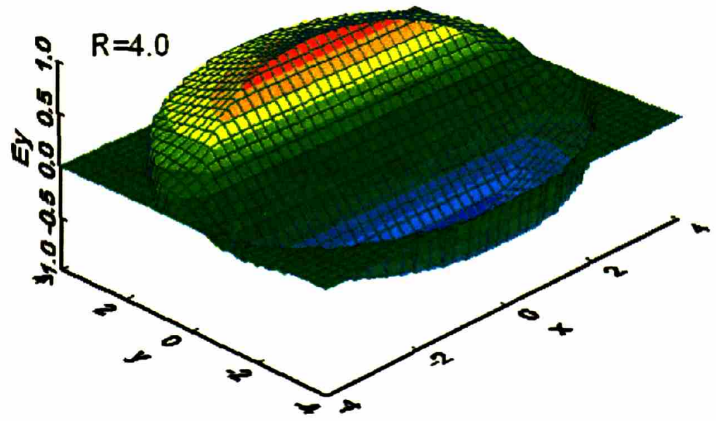

Fig. 4.7 (b)

Figure 4.7 Normalized self-electric field for a uniform 2D elliptic beam inside a perfect conducting pipe with radius $R = 4.0$ obtained analytically from Eqs. (3.26) and (3.27): (a) E_x and (b) E_y.

4.2.5 Particle mover

Once the fields and forces on particles are computed, the particles can be moved to the next time step. The PFB2D code may call for 100,000 particles to be run for 10,000 time steps. This means that the particle motion equations have to be integrated 100,000 times 10,000 = 10^9 times. Therefore, the integration method has to be as fast as possible, while still maintain acceptable accuracy. In addition, our choice of method must take into account the storage capability of the computer we will use in terms of the number of quantities that may be kept for each particle.

Under these considerations, one commonly used integration method is called the leap-frog method. The first-order differential equations to be integrated separately for each particle are

$$\frac{V_{x,n+1/2} - V_{x,n-1/2}}{\Delta t} = \frac{q}{m}\left(E_{x,n} + V_{y,n-1/2}B_{z,n} - V_{z,n-1/2}B_{y,n}\right), \tag{4.19}$$

$$\frac{V_{y,n+1/2} - V_{y,n-1/2}}{\Delta t} = \frac{q}{m}\left(E_{y,n} - V_{x,n-1/2}B_{z,n} + V_{z,n-1/2}B_{x,n}\right), \tag{4.20}$$

$$\frac{x_{n+1} - x_n}{\Delta t} = V_{x,n+1/2}, \tag{4.21}$$

$$\frac{y_{n+1} - y_n}{\Delta t} = V_{y,n+1/2}. \tag{4.22}$$

where $\Delta t = \Delta s/\beta_b c$ in the 2D model and $\beta_b c$ is the axial beam velocity. The flow of a particle's position and velocity in time is shown in Fig. 4.7. The code pushes the velocity back to one half time step initially at time zero; that is, it calculates $\mathbf{V}(-\Delta t/2)$ using the force $\mathbf{F}(t=0)$ at time zero. Then the code advances the velocity and position according to Eqs. (4.19)-(4.22).

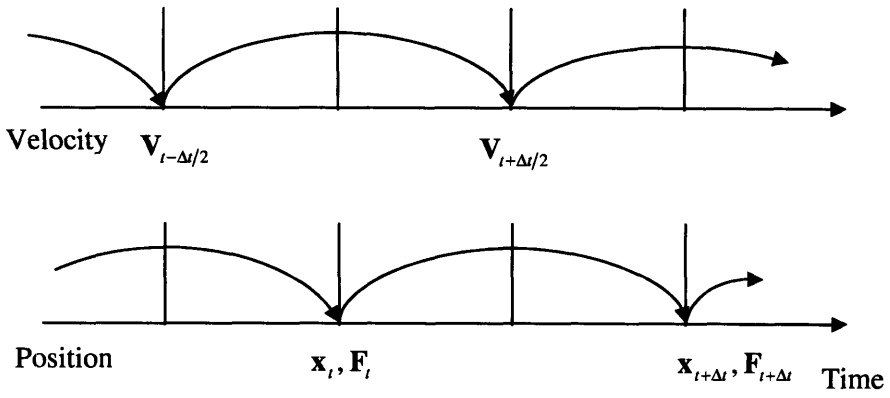

Figure 4.7 Sketch of the leap-frog integration method showing time-centering of the force $\mathbf{F}$ while advancing the velocity $\mathbf{V}$ and of the velocity while advancing the position $\mathbf{x}$.

4.3 PIC simulations of small-aperture alternating-gradient focusing systems

In this section, we apply the PFB2D code to studying the halo formation and beam loss induced by the image-charge effects. In the simulation, the beam distribution is presented by N_p macro-particles which are generated according to the KV distribution.

To illustrate the simulation results, let us focus on the example of an intense charged-particle beam propagating through a periodic quadropule magnetic focusing channel where the magnetic focusing field is defined by the ideal step-function in Eq. (2.34) with system parameters corresponding to $\eta = 0.5$, $\sigma_v = 80°$, $KS/\varepsilon = 10.0$, and $R/\sqrt{\varepsilon S} = 4.0$.

As shown in Fig. 4.9, the envelopes $a(s)$ and $b(s)$ are plotted as a function of the axial distance for beam propagation inside a cylindrical conducting pipe with radius $R/\sqrt{\varepsilon S} = 4.0$. The system parameters are chosen to be: by $\eta = 0.5$, $\sigma_v = 80°$, $KS/\varepsilon = 10.0$ and the K-V

distributed 100k macro-particles are loaded initially at $s = 0$. The solid curves are obtained from the beam envelope equations for a matched solution and the dotted curves are the calculated beam envelopes from the PIC simulation. The two beam envelopes are in good agreement. The beam envelopes obtained from the PIC simulation are stable in this case. The results in Fig. 4.9 demonstrate that the image-charge effects are insignificant on the beam envelopes.

In Fig. 4.10, the centroids $\bar{x}$ and $\bar{y}$ are plotted as a function of the axial distance for beam propagation inside a cylindrical conducting pipe with radius $R/\sqrt{\varepsilon S} = 4.0$. The system parameters are the same as in Fig. 4.9. Because of the choice of the finite number of discrete macro-particles, the center of the beam is not perfectly on the z axis. However, the displacement of the beam center from the z axis in the simulations is kept small and oscillates around the z axis.

In Fig. 4.11, the emittances ε_x and ε_y in the $x-$ and $y-$ directions, respectively, are plotted as a function of the axial distance for beam propagation inside a cylindrical conducting pipe with radius $R/\sqrt{\varepsilon S} = 4.0$. The system parameters are the same as in Fig. 4.9. The beam emittances are conserved within 5% after five periods.

In Fig. 4.12, the trajectories of 5000 particles out of the 100k particles from $\hat{s} = 0$ to $\hat{s} = 20$ are projected onto the phase planes (x, y) at $s/S = 0, 1, 2, ..., 20$ for the same beam as in Fig. 4.8. The green circle represents the cylindrical conducting pipe with radius $R/\sqrt{\varepsilon S} = 4.0$ and the purple ellipse represents the initial beam boundary $x^2/a^2 + y^2/b^2 = 1$. If there are no image-charge effects, the trajectories of the particles should be regular and remain inside the beam boundary. However, in this case the pipe radius is small and the image-charge effects induce significant nonlinear force on the particles. Therefore, the trajectories of the particles become

chaotic. A halo is formed, which is represented by the layer of the particles outside the beam boundary as shown in Fig. 4.12.

In addition, because the halo formation and beam loss depends sensitively on the choice of the pipe radius as indicated by the parametric studies in Chapter 3, we have also investigated the beam losses in the PIC simulations. As shown in Fig. 4.13, the beam loss percentage is simulated with the PFB2D code for the parameter choice $\eta = 0.5$, $\sigma_v = 60°$, $KS/\varepsilon = 10.0$, and $\varepsilon_x = \varepsilon_y = \varepsilon$ with the pipe radius $a_{max}/R = 95.5\%$, where the curves are simulated with the PFB2D code for various choices of particle numbers. The beam loss is sensitive to the macro-particle number N_p. As N_p increases in the simulations, the predicted particle loss decreases. It is apparently that the beam loss calculations in PIC simulations depend on the number of macro-particles. Therefore, the noise in the PIC simulations with moderate particle number is significant, which will be a subject of the investigation in Section 4.4.

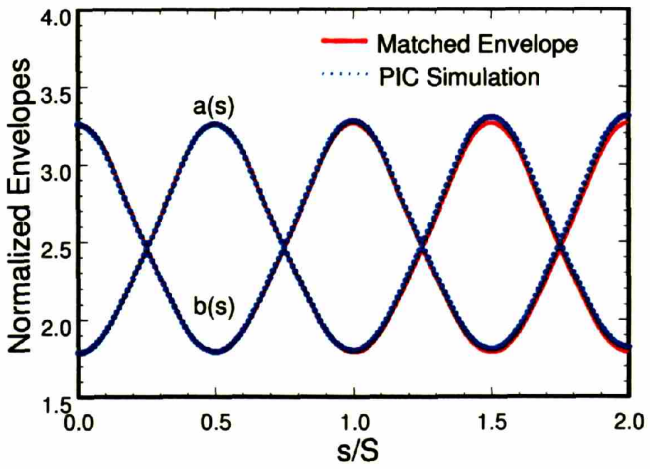

Fig. 4.9 The normalized envelopes $a(s)/\sqrt{\varepsilon S}$ and $b(s)/\sqrt{\varepsilon S}$ are plotted as a function of the axial distance for beam propagation inside a cylindrical conducting pipe with radius $R/\sqrt{\varepsilon S} = 4.0$. The system parameters are chosen to be: $\eta = 0.5$, $\sigma_v = 80°$, and $KS/\varepsilon = 10.0$, and the K-V distributed 100k macro-particle are loaded initially at $\hat{s} = 0$.

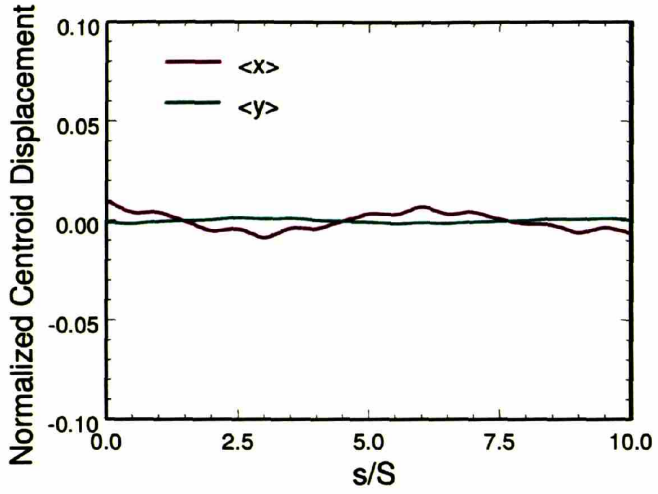

Fig. 4.10 The normalized centroid displacements $\bar{x}/\sqrt{\varepsilon S}$ and $\bar{y}/\sqrt{\varepsilon S}$ are plotted as a function of the axial distance for beam propagation inside a cylindrical conducting pipe with radius $R/\sqrt{\varepsilon S} = 4.0$. The system parameters are the same as in Fig. 4.9.

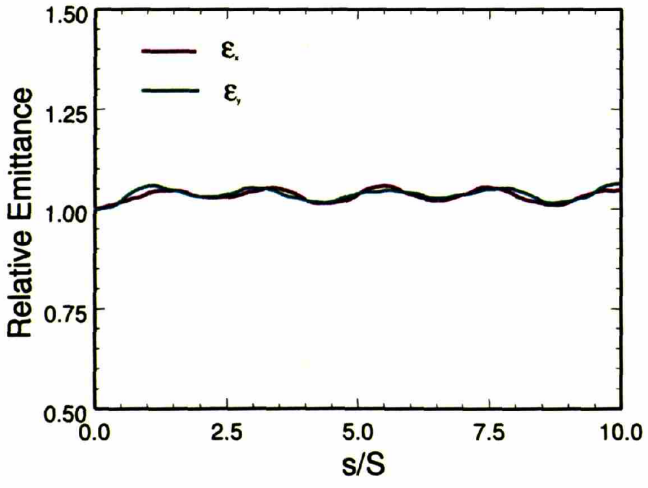

Fig. 4.11 The relative emittances $\varepsilon_x(s)/\varepsilon(0)$ and $\varepsilon_y(s)/\varepsilon(0)$ are plotted as a function of the axial distance for beam propagation inside a cylindrical conducting pipe with radius $R/\sqrt{\varepsilon S} = 4.0$. The system parameters are the same as in Fig. 4.9.

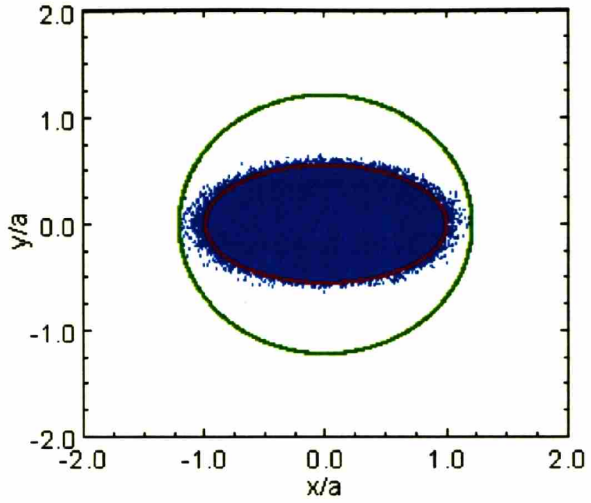

Fig. 4.12 The trajectories of the particles are projected onto the cross-section phase planes (x, y) at $s/S = 0, 1, 2, ..., 20$ for beam propagation inside a cylindrical conducting pipe with radius $R/\sqrt{\varepsilon S} = 4.0$. The system parameters are chosen to be the same as in Fig. 4.9.

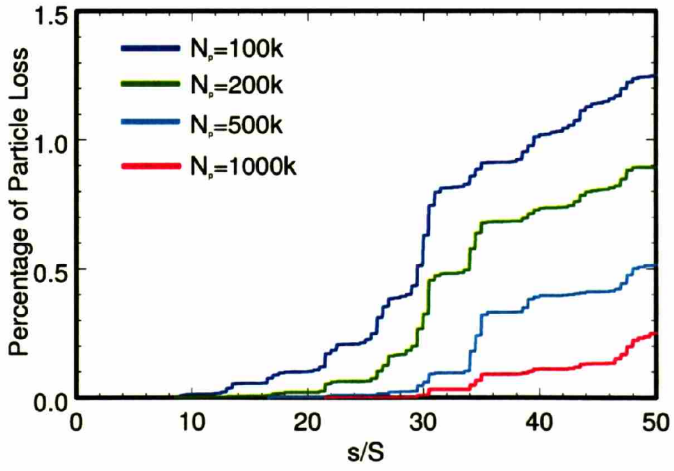

Fig. 4.13 Plot of the beam loss percentage as a function of the axial distance for $a_{max}/R = 95.5\%$ $\eta = 0.5$, $\sigma_v = 60°$, and $KS/\varepsilon = 10.0$, and macro-particle number $N_p = 1\times10^5$, 2×10^5, 5×10^5, and 1×10^6.

4.4 Analysis of noise in PIC simulations

The numerical noise problem has been found to be a very important issue in PIC simulations, as discussed in the previous sections. It causes descrepancies between the simulation results and the theoretical results. In this section, the noise and discrepancies particle diffusion induced by the discrete particle effects is analyzed [50]. In particular, an analytical model is presented which describes the slow-time-scale rms evolution of the edge emittance for a perfectly matched beam in a periodic solenoidal magnetic focusing field. A scaling law for edge emittance growth is derived for beam propagation in a periodic quadrupole magnetic field. Furthermore, the scaling law is verified in the self-consistent Green's function simulations and the PIC PFB2D simulations.

4.4.1 Noise scaling law

Let us consider a continuous charged-particle beam which propagates with average axial velocity $\beta_b c\mathbf{e}_z$ through a periodic quadrupole magnetic field

$$\mathbf{B}^q = B_q(s)[y\mathbf{e}_x + x\mathbf{e}_y]. \tag{4.23}$$

In Eq. (4.23), $s = z$ is the axial coordinate, $B_q(s+S) = B_q(s)$ is the axial component of the applied magnetic field as defined in Eq. (2.9). S is the fundamental periodicity length of the focusing field, c is the speed of light in vacuum.

In the present two-dimensional macro-particle model, the uniform beam density is approximated by

$$n(x,y,s) = \frac{N_b}{N_p}\sum_{i=1}^{N_p}\delta[x - x_i(s)]\delta[y - y_i(s)], \tag{4.24}$$

where N_b is the number of charged-particles per unit axial length, N_p is the number of macro-particles per unit axial length, and (x_i, y_i) is the transverse displacement of the *i*th macro-particle from the beam axis at $(x, y) = (0,0)$.

Under the paraxial approximation, the transverse equations of motion for the *i*th macro-particle of the beam can be expressed as

$$\frac{d^2 x_i}{ds^2} + \kappa_x(s) x_i + \frac{q}{\gamma_b^3 \beta_b^2 mc^2} \frac{\partial \phi^{self}(x_i, y_i, s)}{\partial x_i} = 0, \tag{4.25}$$

$$\frac{d^2 y_i}{ds^2} + \kappa_y(s) y_i + \frac{q}{\gamma_b^3 \beta_b^2 mc^2} \frac{\partial \phi^{self}(x_i, y_i, s)}{\partial y_i} = 0, \tag{4.26}$$

where

$$\phi^{self} = -\frac{qN_b}{N_p} \sum_{j=1(j\neq i)}^{N_p} \ln\left[(x_i - x_j)^2 + (y_i - y_j)^2\right], \tag{4.27}$$

$i = 1, 2, ..., N_p$, $\gamma_b = (1 - \beta_b^2)^{-1/2}$ is the relativistic mass factor, m and q are the particle rest mass and charge, respectively, $\kappa_x = k_q$ and $\kappa_y = -k_q$ with $\kappa_q(s) = qB_q(s)/2\gamma_b\beta_b mc^2$ being a measure of the strength of the quadrupole focusing field, and ϕ^{self} is the self-field scalar potential associated with the beam space-charge.

For simplicity, let us first consider the Kapchinskij-Vladimirskij (KV) beam

$$n_{KV}(x_i, y_i, s) = \begin{cases} N_b/\pi a(s)b(s), & \dfrac{x^2}{a^2} + \dfrac{y^2}{b^2} \leq 1, \\ 0, & \dfrac{x^2}{a^2} + \dfrac{y^2}{b^2} > 1, \end{cases} \tag{4.28}$$

where $a(s)$ and $b(s)$ are the beam envelopes in the x- and y- directions, respectively. The scalar potential for the self-electric field is given by

$$\phi_{KV}^{self}(x,y,s) = -\frac{qN_b}{[a(s)+b(s)]}\left[\frac{x^2}{a(s)}+\frac{y^2}{b(s)}\right] \tag{4.29}$$

in the beam interior. Substituting $\phi^{self}(x_i, y_i, s) = \phi_{KV}^{self}(x_i, y_i, s)$ into Eqs. (4.25) and (4.26), the equilibrium particle orbits $x_i(s)$ and $y_i(s)$ can be expressed as [36]

$$x_i(s) = A_{xi} w_x(s)\cos[\psi_x(s)+\Phi_{xi}], \tag{4.30}$$

$$y_i(s) = A_{yi} w_y(s)\sin[\psi_y(s)+\Phi_{yi}], \tag{4.31}$$

where A_{xi}, $A_{yi} = (1-A_{xi}^2)^{1/2}$, Φ_{xi} and Φ_{yi} are constants determined by the initial conditions, $\psi_x = \int_0^s ds/w_x^2(s)$ and $\psi_y = \int_0^s ds/w_y^2(s)$ are the accumulated phases of the betatron oscillations in the x- and y- directions, respectively, and $w_x(s+S) = w_x(s)$ and $w_y(s+S) = w_y(s)$ solves the beams envelope equations

$$\frac{d^2 w_x}{ds^2}+\left[\kappa_q - \frac{1}{a(s)}\frac{2K}{a(s)+b(s)}\right]w_x = \frac{1}{w_x^3}, \tag{4.32}$$

$$\frac{d^2 w_y}{ds^2}+\left[-\kappa_q - \frac{1}{b(s)}\frac{2K}{a(s)+b(s)}\right]w_y = \frac{1}{w_y^3}, \tag{4.33}$$

where $w_x = a/\sqrt{\varepsilon_x}$ and $w_x = b/\sqrt{\varepsilon_y}$ with ε_x and ε_y being the unnormalized emittance of the beam, and $K = 2q^2 N_b/\gamma_b^3\beta_b^2 mc^2$ being the perveance of the beam.

The particle distribution function for the KV equilibrium can be expressed as

$$f_{\mathrm{KV}}(x,y,x',y')=\frac{N_b}{\pi^2\sqrt{\varepsilon_x\varepsilon_y}}\delta\left(\frac{A_x^2}{\varepsilon_x}+\frac{A_y^2}{\varepsilon_y}-1\right), \tag{4.34}$$

where $\delta(x)$ is the Dirac δ- function. Because the four-dimensional phase-space volume element is given by

$$dxdydx'dy'=\frac{1}{\sqrt{\varepsilon_x\varepsilon_y}}A_xA_ydA_xdA_yd\Phi_xd\Phi_y, \tag{4.35}$$

integrating f_{KV} over A_y, Φ_x and Φ_y yields the distribution function for A_x over a KV beam

$$F_{\mathrm{KV}}(A_x)=\begin{cases}2N_b\,A_x/\sqrt{\varepsilon_x}, & 0\le A_x\le\sqrt{\varepsilon_x},\\ 0, & A_x>\sqrt{\varepsilon_x}.\end{cases} \tag{4.36}$$

Note from Eq. (4.36) that the largest concentration of particles occurs at $A_x=\sqrt{\varepsilon_x}$. Also, particles with $A_{xi}=\sqrt{\varepsilon_x}$ reach the edge of the beam with $x_i=a$. Therefore, they are most likely to leave the beam core under the perturbations induced by the discrete-particle effects.

In the simulations, discrete macro-particles are used which deviates from the smooth beam density $n_{\mathrm{KV}}(x,y,s)$ of the KV equilibrium. For a large number of particles the deviation is small. Such small deviation will induce the slow-time-scale evolution of $A_{xi}(s)$, $A_{yi}(s)$, $\Phi_{xi}(s)$ and $\Phi_{yi}(s)$ in the particle orbits given in Eqs. (4.30)and (4.31). The deviation has the most profound effects on the edge particles which initially have $A_{xi}(s=0)/\sqrt{\varepsilon_x}=1$ and $A_{yi}(s=0)/\sqrt{\varepsilon_y}=\left[1-A_{xi}^2(s=0)/\varepsilon_x\right]^{1/2}=0$, because they are most likely to diffuse away from the beam core.

Substituting Eq. (4.30) into Eq. (4.25) , we obtain

$$A''_{xi} w_x \cos[\psi_x + \Phi_{xi}] + 2A'_{xi} w'_x \cos[\psi_x + \Phi_{xi}] - 2(A'_{xi} w_x + A_{xi} w'_x)(\psi'_x + \Phi'_{xi}) \sin[\psi_x + \Phi_{xi}]$$

$$+ A_{xi} w_x (\psi'_x + \Phi'_{xi})^2 \cos[\psi_x + \Phi_{xi}] + A_{xi} w''_x \cos[\psi_x + \Phi_{xi}] - A_{xi} w_x \sin[\psi_x + \Phi_{xi}](\psi''_x + \Phi''_{xi})$$

$$= -\kappa_q A_{xi} w_x \cos[\psi_x + \Phi_{xi}] - \frac{K}{2qN_b} \frac{\partial \phi^{self}}{\partial x_i}. \tag{4.37}$$

Taking into account the slow dependence of A_{xi} and Φ_{xi}, omitting the second-order differentiations A''_{xi}, Φ''_{xi}, $A'_{xi}\Phi'_{xi}$, and using $\psi'_x = 1/w_x^2$, we express Eq. (4.37) as

$$\cos[\psi_x + \Phi_{xi}]\left[2A'_{xi} w'_x - A_{xi} \frac{2\Phi'_{xi}}{w_x} - A_{xi}\left(w''_x - \kappa_q w_x - \frac{1}{w_x^3}\right)\right] - 2\sin[\psi_x + \Phi_{xi}]\left[\frac{A'_{xi}}{w_x} + A_{xi} w'_x \Phi'_{xi}\right]$$

$$= -\frac{K}{2qN_b} \frac{\partial \phi^{self}}{\partial x_i}. \tag{4.38}$$

Making use of Eq. (4.32), we reduce Eq. (4.38) to

$$\cos[\psi_x + \Phi_{xi}]\left[A'_{xi} w'_x - \frac{A_{xi}\Phi'_{xi}}{w_x}\right] - \sin[\psi_x + \Phi_{xi}]\left[\frac{A'_{xi}}{w_x} + A_{xi}\Phi'_{xi} w'_x\right] = -\frac{K}{4qN_b} \frac{\partial}{\partial x_{xi}}\left[\phi^{self} - \phi^{self}_{\mathrm{KV}}\right]. \tag{4.39}$$

It is evident in Eq. (4.39) that $A'_{xi} = \Phi'_{xi} = 0$ if $\phi^{self} = \phi^{self}_{\mathrm{KV}}$.

Let us examine the particle orbits carefully, focusing on

$$x_i(s) = A_{xi} w_x(s) \cos[\psi_x(s) + \Phi_{xi}]. \tag{4.40}$$

The orbit oscillations occur at two different time scales. One is the envelope oscillations with the same period as the magnetic focusing field S, and the other is the betatron oscillations with the

period $2\pi S/\sigma$, where $\sigma \equiv \int_s^{s+S} ds/w_x^2$ is the phase advance. The diffusion process is slower than both types of the orbit oscillations. To derive a closed set of equations for the slowly varying variables A_{xi} and Φ_{xi}, we take an averages of Eq. (4.39) over the faster envelope oscillations and then an average over the betatron oscillations, respectively. The independent differential equations which determine the slowly varying variables A_{xi} and Φ_{xi} (see Appendix C) are

$$\frac{dA_{xi}}{ds} = -\frac{K}{\sqrt{\varepsilon_x} N_p} \sum_{j=1(j\neq i)}^{N_p} \frac{B_j b_j + C_j c_j}{b_j^2 + c_j^2}, \tag{4.41}$$

$$\frac{d\Phi_{xi}}{ds} = \frac{K}{2\varepsilon_x} - \frac{K}{A_{xi}\sqrt{\varepsilon_x} N_p} \sum_{j=1(j\neq i)}^{N_p} \frac{C_j b_j - B_j c_j}{b_j^2 + c_j^2}. \tag{4.42}$$

where

$$B_j = -\frac{1}{2}\frac{A_{xj}}{\sqrt{\varepsilon_x}} \sin\Delta_{xj}, \tag{4.43}$$

$$C_j = \frac{1}{2}\left(\frac{A_{xi}}{\sqrt{\varepsilon_x}} - \frac{A_{xj}}{\sqrt{\varepsilon_x}} \cos\Delta_{xj}\right), \tag{4.44}$$

$$a_j = \frac{A_{xi}^2}{2\varepsilon_x} - \frac{A_{xi}A_{xj}}{\varepsilon_x}\cos\Delta_{xj} + \frac{A_{xj}^2}{2\varepsilon_x} + \frac{A_{yj}^2}{2\varepsilon_y}, \tag{4.45}$$

$$b_j = \frac{1}{2\varepsilon_x}\left(A_{xi} - A_{xj}\cos\Delta_{xj}\right)^2 - \frac{1}{2\varepsilon_x}\left(A_{xj}\sin\Delta_{xj}\right)^2 - \frac{A_{yj}^2}{2\varepsilon_y}\cos\left[2\Delta_\psi + 2\Delta_{yj}\right], \tag{4.46}$$

$$c_j = \frac{1}{\varepsilon_x}\left(A_{xi} - A_{xj}\cos\Delta_{xj}\right)A_{xj}\sin\Delta_{xj} + \frac{A_{yj}^{\ 2}}{2\varepsilon_y}\sin\left[2\Delta_\psi + 2\Delta_{yj}\right], \tag{4.47}$$

with $\Delta_{\psi} \equiv \psi_y - \psi_x$, $\Delta_{xj} \equiv \Phi_{xj} - \Phi_{xi}$, and $\Delta_{yj} \equiv \Phi_{yj} - \Phi_{xi}$. Results in Eq. (4.41)-(4.47) are the generalization of those in [50] from a periodic solenoidal focusing channel to a periodic quadropule magnetic focusing channel.

In the following derivation, use is made of the dimensionless variables and normalized parameters defined by $\hat{s} = s/S$, $\hat{x} = x/\sqrt{S\varepsilon_x}$, $\hat{y} = y/\sqrt{S\varepsilon_y}$, $\hat{a} = a/\sqrt{S\varepsilon_x}$, $\hat{b} = b/\sqrt{S\varepsilon_y}$, $\hat{A}_{xi} = A_{xi}/\sqrt{\varepsilon_x}$, $\hat{A}_{yi} = A_{yi}/\sqrt{\varepsilon_y}$, $\hat{\kappa}_q = S^2\kappa_q$ and $\hat{K} = SK/\varepsilon$. Using Eq. (4.41) and (4.42), detailed dynamics of the edge particles initially with $\hat{A}_{xi} = 1$ and $\hat{A}_{yi} = 0$ is analyzed. In particular, we investigate the diffusion of the edge particles which can be regarded as a measure of the numerical noise in PIC simulations. The variance $\sigma^2 = \left\langle \left(\hat{A}_{xi} - \left\langle \hat{A}_{xi} \right\rangle\right)^2 \right\rangle$ is used to describe the diffusion process quantitatively, where the average is taken over the particles that are initially located on the beam boundary with $\hat{A}_{xi} = 1$ and $\hat{A}_{yi} = 0$. Let us compute the expectation value of

$$d^2\sigma^2/ds^2 = 2\left\langle \left(\hat{A}'_{xi} - d\left\langle \hat{A}_{xi} \right\rangle/d\hat{s}\right)^2 \right\rangle, \tag{4.48}$$

where the second derivative of A_{xi} is omitted because of the slow dependence of A_{xi}. Averaging Eq. (4.48) over all possible beam distributions which approach the KV distribution when $N_p \to \infty$, then

$$\left\langle \frac{d\hat{A}_{xi}}{d\hat{s}} \right\rangle_{A_{xi}(\hat{s}=0)=1} = \left\langle -\hat{K} \int \frac{B_j b_j + C_j c_j}{b_j^2 + c_j^2} f_{\mathrm{KV}}\left(\hat{x}_j, \hat{y}_j, \hat{x}'_j, \hat{y}'_j, \hat{s}\right) d\hat{x}_j d\hat{y}_j d\hat{x}'_j d\hat{y}'_j \right\rangle_{A_{xi}(\hat{s}=0)=1} = 0, \tag{4.49}$$

$$\left\langle \left(\frac{d\hat{A}_{xi}}{d\hat{s}}\right)^2 \right\rangle_{A_{xi}(\hat{s}=0)=1} = \frac{\hat{K}^2}{N_p} \left\langle \int \left(\frac{B_j b_j + C_j c_j}{b_j^2 + c_j^2}\right)^2 f_{\mathrm{KV}}\left(\hat{x}_j, \hat{y}_j, \hat{x}'_j, \hat{y}'_j, \hat{s}\right) d\hat{x}_j d\hat{y}_j d\hat{x}'_j d\hat{y}'_j \right\rangle_{A_{xi}(\hat{s}=0)=1}. \tag{4.50}$$

Therefore, the expectation of the variance is

$$\sigma^2(\hat{s}) - \sigma^2(0) = D\hat{s}^2, \tag{4.51}$$

where the "diffusion" coefficient is defined as

$$D = \xi \frac{\hat{K}^2}{N_p}, \tag{4.52}$$

with

$$\xi \equiv \left\langle \int \left(\frac{B_j b_j + C_j c_j}{b_j^2 + c_j^2} \right)^2 f_{\mathrm{KV}}(\hat{x}_j, \hat{y}_j, \hat{x}'_j, \hat{y}'_j, \hat{s}) d\hat{x}_j d\hat{y}_j d\hat{x}'_j d\hat{y}'_j \right\rangle_{A_{xi}(\hat{s}=0)=1}. \tag{4.53}$$

Using the Monte-Carlo method, we estimate $\xi = 0.5 \pm 0.3$. In a particular beam simulation, the value of ξ depends on geometry and numerical scheme. In general, the coefficient ξ is slightly higher for the Green's function simulations than for the PIC simulations.

In dimensional units, the edge emittance error scaling law is given by

$$\frac{\varepsilon^{edge}(s)}{\varepsilon^{edge}(0)} - 1 = \xi \frac{K^2 s^2}{(\varepsilon_{rms}(0))^2 N_p}. \tag{4.54}$$

where $\xi = 0.5 \pm 0.3$.

Since the derivation of Eq. (4.41) and (4.42) does not require the explicit form of the focusing magnetic focusing field $\mathbf{B}(s)$, Eq. (4.41) and (4.42) are valid for an arbitrary periodic magnetic focusing channel. This result is also applicable for a beam propagating through a periodic solenoidal magnetic focusing channel, as discussed previously in [50]. To revisit the derivation in [50], let us consider a continuous circular charged-particle beam which propagates with average axial velocity $\beta_b c \mathbf{e}_z$ through an axisymmetric periodic solenoidal magnetic field,

$$\mathbf{B} = B_z(s)\mathbf{e}_z - \frac{1}{2}\frac{dB_z}{ds}\left[x\mathbf{e}_x + y\mathbf{e}_y\right]. \tag{4.55}$$

In Eq. (4.55) $s = z$ is the axial coordinate, $B_z(s+S) = B_z(s)$ is the axial component of the applied magnetic field. S is the fundamental periodicity length of the focusing field, c is the speed of light in vacuum.

Under the paraxial approximation, the transverse equations of motion for the ith macro-particle of the beam can be expressed as

$$\frac{d^2x_i}{ds^2} - 2\sqrt{\kappa_z(s)}\frac{dy_i}{ds} - \frac{d\sqrt{\kappa_z(s)}}{ds}y_i - \frac{q}{\gamma_b^3\beta_b^2mc^2}\frac{\partial\phi^{self}(x_i, y_i, s)}{\partial x_i} = 0, \tag{4.56}$$

$$\frac{d^2y_i}{ds^2} - 2\sqrt{\kappa_z(s)}\frac{dx_i}{ds} - \frac{d\sqrt{\kappa_z(s)}}{ds}x_i - \frac{q}{\gamma_b^3\beta_b^2mc^2}\frac{\partial\phi^{self}(x_i, y_i, s)}{\partial y_i} = 0, \tag{4.57}$$

where $i = 1, 2, ..., N_p$, $\sqrt{\kappa_z(s)} = qB_z(s)/2\gamma_b\beta_bmc^2$ is a measure of the strength of the solenoidal magnetic focusing field.

Introducing a "time"-dependent rotating frame (Larmor frame) defined as

$$\tilde{x}(s) = x(s)\cos[\varphi(s)] - y(s)\sin[\varphi(s)] \tag{4.58}$$

$$\tilde{y}(s) = x(s)\sin[\varphi(s)] + y(s)\cos[\varphi(s)] \tag{4.59}$$

where

$$\varphi(s) = \int_{s_0}^{s}\sqrt{\kappa_z(s)}ds. \tag{4.60}$$

The equations of motion can be written in the Larmor frame as

$$\frac{d^2\tilde{x}_i}{ds^2} + \kappa_z(s)\tilde{x}_i + \frac{q}{\gamma_b^3\beta_b^2mc^2}\frac{\partial\phi^{self}(\tilde{x}_i, \tilde{y}_i, s)}{\partial\tilde{x}_i} = 0, \tag{4.61}$$

$$\frac{d^2\tilde{y}_i}{ds^2} + \kappa_z(s)\tilde{y}_i + \frac{q}{\gamma_b^3\beta_b^2 mc^2}\frac{\partial\phi^{self}(\tilde{x}_i,\tilde{y}_i,s)}{\partial\tilde{y}_i} = 0. \tag{4.62}$$

The equilibrium particle orbits $\tilde{x}_i(s)$ and $\tilde{y}_i(s)$ can be expressed as [36]

$$\tilde{x}_i(s) = A_{xi}w(s)\cos[\psi(s) + \Phi_{xi}] \tag{4.63}$$

$$\tilde{y}_i(s) = A_{yi}w(s)\sin[\psi(s) + \Phi_{yi}] \tag{4.64}$$

where A_{xi}, $A_{yi} = (1 - A_{xi}^2)^{1/2}$, Φ_{xi} and Φ_{yi} are constants determined by the initial conditions, $\psi = \varepsilon\int_0^s ds/r_b^2(s)$ is the accumulated phase of the betatron oscillations, and $w = r_b(s)/\sqrt{\varepsilon}$ solves the beam envelope equation

$$w'' + \kappa_z(s)rw - \frac{K}{r_b^2}w = \frac{1}{w^3}, \tag{4.65}$$

with ε being the unnormalized emittance of the beam.

Taking $w_x = w_y = w$, $\psi_x = \psi_y = \psi$, $a = b = r_b$, and $\varepsilon_x = \varepsilon_y = \varepsilon$, we follow the derivation as we presented earlier in this subsection for the beam propagating through a periodic quadrupole magnetic focusing channel to obtain the same scaling law for beams propagating through the periodic solenoidal magnetic focusing channel, as expressed in Eqs. (4.54).

4.4.2 Verification of the noise scaling law in Green's function simulations

To verify the noise scaling law in Eq. (4.54), we first review the results from the self-consistent Green's function simulations for periodic solenoidal magnetic focusing channels [50].

In the simulations, a first set of N_p macro-particles is loaded corresponding to the KV distribution, a second set of N_t (usually $N_t < N_p$) macro-particles is loaded with $A_{xi} = 1$, $A_{yi} = 0$ and Φ_{xi} ranging uniformly from 0 to 2π. Then the edge emittance $\varepsilon^{edge}(\hat{s})$ is calculated on the second set of edge particles and D is calculated. As the beam propagates through the channel, the N_p macro-particles in the first set of interact with each other, whereas the second set test particles experience the electric and magnetic forces imposed by the particles in the first set.

The simulations of a high-intensity circular beam propagating through the periodic solenoidal magnetic focusing channel are performed. In the simulations,

$$A_{xi}(\hat{s}) = \sqrt{\left(\frac{\hat{\tilde{x}}_{xi}}{\hat{r}_b}\right)^2 + \left(\hat{\tilde{x}}_{xi}\hat{r}_b' - \hat{\tilde{x}}_{xi}'\hat{r}_b\right)^2} \tag{4.66}$$

is tracked for the second set of edge particles which have initially $A_{xi} = 1$, $A_{yi} = 0$ and Φ_{xi} ranging uniformly from 0 to 2π, and the expectation value of σ^2 over the test particles are readily computed. Results are summarized in Fig. 4.13-4.15. In Eq. (4.66), $\hat{r}_b = \hat{w}\sqrt{\varepsilon}$ and $\hat{r}_b' = \hat{w}'\sqrt{\varepsilon}$ are solved from the beam envelope equation (4.65).

The periodic magnetic focusing channel in the self-consistent Green's function simulations is defined by

$$\hat{\kappa}_z(\hat{s}) = [a_0 + a_1 \cos(2\pi\hat{s})]^2 . \tag{4.67}$$

Figure 4.14 shows a plot of $\sigma^2/\hat{s}^2$ versus the propagation distance $\hat{s} = s/S$ obtained from the self-consistent Green's function simulation. The choice of system parameters in Fig. 4.14

corresponding to $N_p = 1024$, $N_t = 512$, $\hat{K} = 0.5$, and $\hat{\kappa}_z$ defined in Eq. (4.67) with $a_0 = a_1 = 0.648$. Due to small residual correlation in the initial distributions of test particles and background macro-paticles, the value of $\sigma^2/\hat{s}^2$ is large for $\hat{s} \leq 1$. As the beam propagates, the residual correlation decays rapidly, and the value of $\sigma^2/\hat{s}^2$ approaches a plateau for $\hat{s} > 1$, where the diffusion coefficient is calculated to be $D = 1.0 \times 10^{-4}$ ($\xi = 0.4$), as indicated by the dashed line. As the beam propagates further through the focusing channel, the plateau levels off because the test particles become widely spread about $A_{xi} = 1$.

The scaling law is verified by varying marco-particle number N_p and peaveance $\hat{K}$ in the self-consistent Green's function simulations. Figure 4.15 shows a logarithmic plot of D versus $\hat{K}$ obtained from self-consistent Green's function simulations for beam propagation through the same periodic focusing channel as in Fig. 4.14. In Fig. 4.15, the number of background macro-particles is kept at a constant value of $N_p = 1024$. The dotted curve is from the self-consistent simulations, whereas the solid line is the fitting curve according to the analytical result $D = \alpha \hat{K}^2$, where α is fitted to be $\alpha = \xi/N_p = 3.5 \times 10^{-4}$ ($\xi = 0.35$).

In Fig. 4.16, the diffusion coefficient D is plotted as a function of N_p, as obtained from self-consistent simulations of beam propagation through the same periodic focusing channel in Fig. 4.16 for a fixed value of $\hat{K} = 0.5$. The dotted curve is from the self-consistent simulations, whereas the solid line is the fitting curve according to the analytical result $D = \beta/N_p$, where β is fitted to be $\beta = \xi\hat{K}^2 = 0.12$ ($\xi = 0.48$). In comparison with Fig. 4.15, data fluctuations in Fig. 4.16 are larger because the initial distribution changes as N_p is varied.

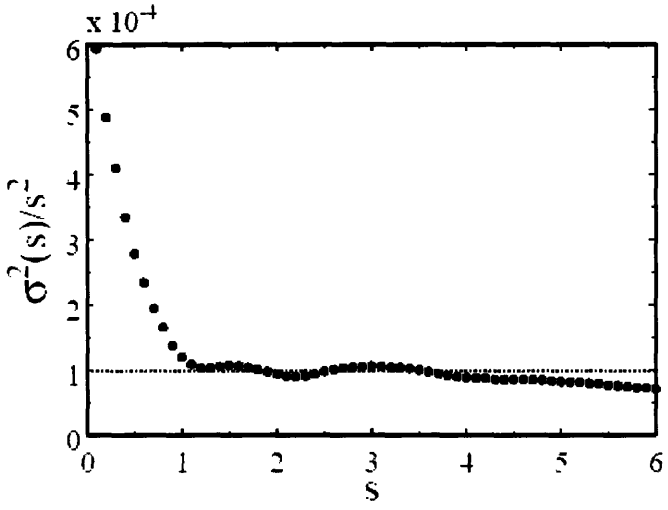

Fig. 4.14 Plot of $\sigma^2/\hat{s}^2$ as a function of $\hat{s}$ obtained from the self-consistent Green's function simulation with the choice of system parameters corresponding to $N_p = 1024$, $N_t = 512$, $\hat{K} = 0.5$, and $\hat{\kappa}_z$ defined in Eq. (4.67) with $a_0 = a_1 = 0.648$.

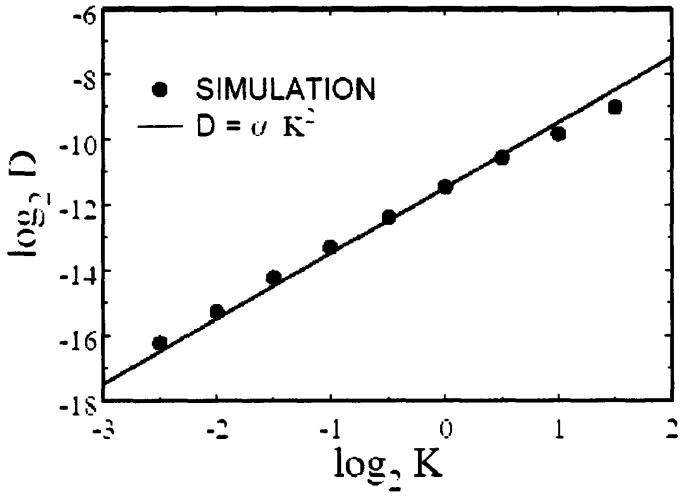

Fig. 4.15 Log-Log plot of D versus $\hat{K}$ obtained from the self-consistent Green's function simulations with the choice of system parameters corresponding to $N_p = 1024$, $N_t = 512$, and $\hat{\kappa}_z$ defined in Eq. (4.67) with $a_0 = a_1 = 0.648$.

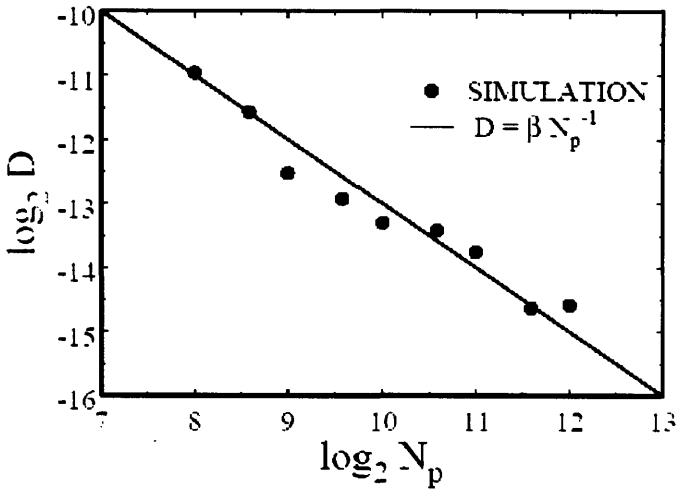

Fig. 4.16 Log-Log plot of D versus N_p obtained from the self-consistent Green's function simulations with the choice of system parameters corresponding to $N_t = 512$, $\hat{K} = 0.5$ and $\hat{\kappa}_z$ defined in Eq. (4.67) with $a_0 = a_1 = 0.648$.

To conclude, it is evident in Fig. 4.15 and 4.16 that the Green's function simulations results are in good agreement with the analytically predicted scaling law discussed in Section 4.4.2.

4.4.3 Verification of the noise scaling law in PIC simulations

We have derived the noise scaling law based a generalization of the previous derivation for the periodic solenoidal magnetic focusing channel on the Green's function simulation model. The present derivation is shown that the noise scaling law is also valid in the self-consistent PIC simulations of intense charged-particle beams propagating through either a periodic solenoidal magnetic focusing channel or a periodic quadrupole magnetic focusing channel.

The only difference between self-consistent Green's function simulations and self-consistent PIC simulations is in the calculation methods of the self-potential. In Green's function simulation, the self-potential is calculated according to the discrete macro-particles by using Eq. (4.32), while in PIC simulation the self-potential is calculated on the grid points according to the weighted average of discrete macro-particles using Eqs. (4.13) and (4.14). The self-potential calculation in both simulations is essentially the same except that in PIC simulations the effects of discrete macro-particles are smoothed out on the grid points. Therefore, the noise scaling law is valid for PIC simulations with a slightly smaller diffusion coefficient ξ.

To verify the scaling law, self-consistent PIC PFB2D simulations have been carried out for the periodic solenoidal magnetic focusing channel (see Figs. 4.17 – 4.18) and for the periodic quadrupole magnetic focusing channel (see Figs. 4.19 – 4.20), using the same process described in Section 4.4.2.

The scaling law is verified for an intense charged-particle beam propagating through a periodic solenoidal magnetic focusing channel. PIC PFB2D simulations are performed by varying macro-particle number N_p and peaveance $\hat{K}$. Figure 4.17 shows a logarithmic plot of D versus $\hat{K}$ obtained from self-consistent PIC PFB2D simulations for beam propagation through the periodic solenoidal magnetic focusing channel with the other system parameters corresponding to $N_p = 100\text{k}$, $N_t = 1024$, and $\hat{\kappa}_z$ defined in Eq. (4.67) with $a_0 = a_1 = 0.648$. The dotted curve is from the self-consistent PIC PFB2D simulations, whereas the solid line is the fitting curve according to the analytical result $D = \alpha \hat{K}^2$, where α is fitted to be $\alpha = \xi / N_p = 2.7 \times 10^{-6}$ ($\xi = 0.27$).

In Fig. 4.18, the diffusion coefficient D is plotted as a function of N_p, as obtained from self-consistent PFB2D simulations of beam propagation through the periodic solenoidal magnetic focusing channel with the other system parameters corresponding to $N_t = 1024$, $\hat{K} = 0.5$ and $\hat{\kappa}_z$ defined in Eq. (4.67) with $a_0 = a_1 = 0.648$. The dotted curve is from the self-consistent simulations, whereas the solid line is the fitting curve according the analytical result $D = \beta / N_p$, where β is fitted to be $\beta = \xi \hat{K}^2 = 0.079$ ($\xi = 0.32$). It is evident in Fig. 4.17 and 4.18 that the PIC PFB2D simulation results are in good agreement with the analytically predicted scaling law discussed in Section 4.4.2. The diffusion coefficient ξ is slightly smaller in the PIC PFB2D simulations than that in the self-consistent Green's function simulations.

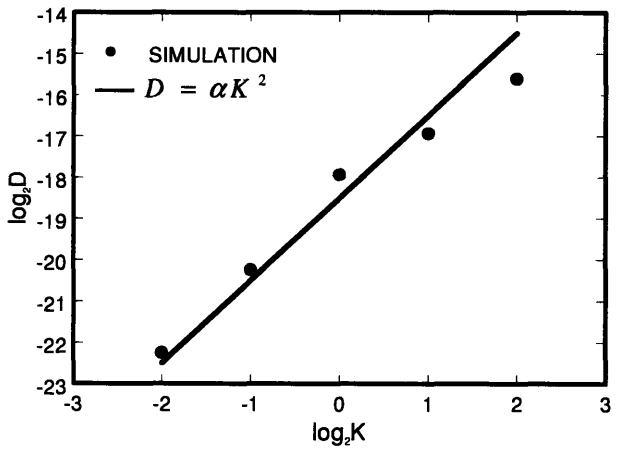

Fig. 4.17 Log-Log plot of D versus $\hat{K}$ obtained from the self-consistent PIC simulation for an intense charged-particle propagating through a periodic solenoidal magnetic focusing channel with the system parameters corresponding to $N_p = 100\text{k}$, $N_t = 1024$, and $\hat{\kappa}_z$ defined in Eq. (4.67) with $a_0 = a_1 = 0.648$.

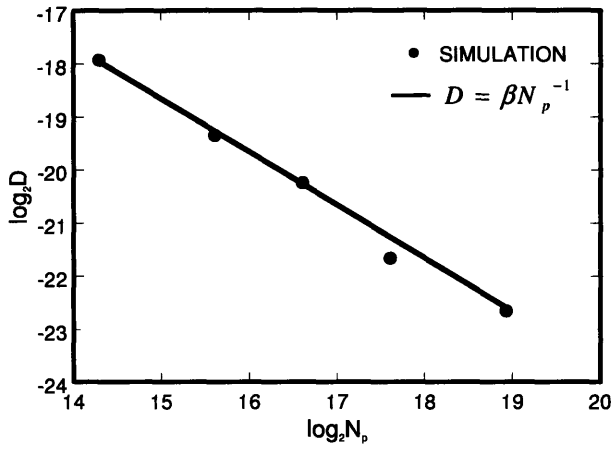

Fig. 4.18 Log-Log plot of D versus N_p obtained from the self-consistent PIC simulation for an intense charged-particle propagating through a periodic solenoidal magnetic focusing channel with the system parameters corresponding to $N_t = 1024$, $\hat{K} = 0.5$ and $\hat{\kappa}_z$ defined in Eq. (4.67) with $a_0 = a_1 = 0.648$.

The scaling law is also verified for an intense charged-particle beam propagating through a periodic quadrupole magnetic focusing channel. PIC PFB2D simulations have been performed by varying marco-particle number N_p and peaveance $\hat{K}$. Figure 4.19 shows a logarithmic plot of D versus $\hat{K}$ obtained from self-consistent PIC simulations for beam propagation through the periodic quadrupole magnetic focusing channel. The periodic quadrupole magnetic focusing channel is defined by the ideal step-function

$$\kappa_q(s) = \begin{cases} +\kappa_{q0}, & 0 \le s/S < 0.25\eta, \\ 0, & 0.25\eta \le s/S < 0.5(1-0.5\eta), \\ -\kappa_{q0}, & 0.5(1-0.5\eta) \le s/S < 0.5(1+0.5\eta), \\ 0, & 0.5(1+0.5\eta) \le s/S < 0.5(2-0.5\eta), \\ +\kappa_{q0}, & 0.5(2-0.5\eta) \le s/S < 1, \end{cases} \tag{4.68}$$

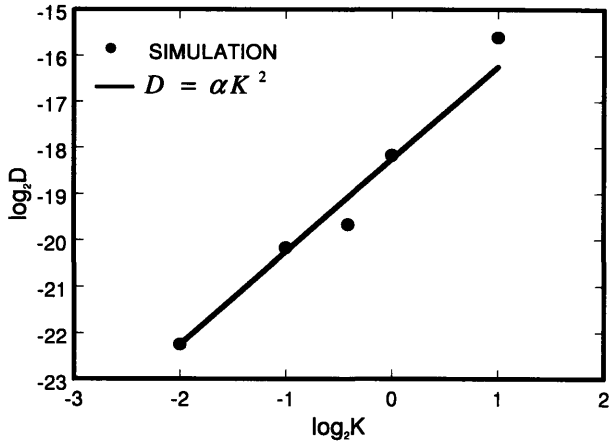

Fig. 4.19 Log-Log plot of D versus $\hat{K}$ obtained from the self-consistent PIC PFB2D simulation for an intense charged-particle propagating through a periodic quadrupole magnetic focusing channel with the system parameters corresponding to $N_p = 100\text{k}$, $N_t = 1024$, $\sigma_v = 50°$ and $\eta = 0.5$.

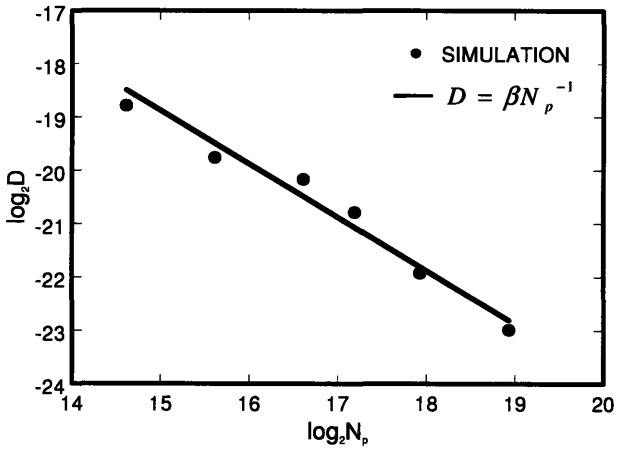

Fig. 4.20 Log-Log plot of D versus N_p obtained from the self-consistent PIC PFB2D simulation for an intense charged-particle propagating through a periodic quadrupole magnetic focusing channel with the system parameters corresponding to $N_t = 1024$, $\hat{K} = 0.5, \sigma_v = 50°$ and $\eta = 0.5$.

The system parameter choice is corresponding to $N_p = 100\text{k}$, $N_t = 1024$, $\sigma_v = 50°$ and $\eta = 0.5$. The dotted curve is from the self-consistent PIC PFB2D simulations, whereas the solid line is the analytical result given by $D = \alpha\hat{K}^2$, where $\alpha = \xi/N_p = 3.2\times10^{-6}$ ($\xi = 0.32$).

In Fig. 4.20, the diffusion coefficient D is plotted versus N_p, as obtained from self-consistent simulations of beam propagation through the periodic focusing channel with the system parameters corresponding to $N_t = 1024$, $\hat{K} = 0.5$, $\sigma_v = 50°$ and $\eta = 0.5$. The dotted curve is from the self-consistent PFB2D simulations, whereas the solid line is the analytical result given by $D = \beta/N_p$, where $\beta = \xi\hat{K}^2 = 0.068$ ($\xi = 0.27$). It is evident in Fig. 4.19 and 4.20 that the PIC PFB2D simulation results verify the noise scaling law for an intense charged-particle beam propagating through a periodic quadrupole magnetic focusing channel.

4.5 Summary

To summarize, a self-consistent PIC simulation code, Periodically Focused Beam (PFB2D), has been developed. The algorithms used in the code are discussed. Such a code is used to simulate intense charged-particle beams in small-aperture alternating-gradient systems which were investigated theoretically in Chapter 2 and 3. PIC PFB2D simulation results on the beam envelope are consistent with the envelope equations solutions, and PIC simulation results on the halo formation are consistent with the test-particle results. However, due to the numerical noise in PIC simulations, the beam loss predicted by PIC PFB2D simulation is an order of magnitude higher than that predicted by the theory, which led to the an analysis of noise in PIC simulations.

In order to resolve the numerical noise problem, an error scaling law for the edge emittance growth and particle diffusion due to the discrete macro-particle effects has been derived for the

periodic magnetic quadrupole focusing field. The error scaling law is valid for both the periodic solenoidal magnetic focusing channel and the periodic quadrupole magnetic focusing channel. In addition, the error scaling law is tested in the self-consistent Green's function simulations and self-consistent PIC PFB2D simulations. The simulation results show good agreement with the error scaling law. The error scaling law will provide a useful guide in determining the fidelity of self-consistent PIC or Green's function simulation studies of halo formation and beam loss, which is a very important aspect in the design of high-power accelerators and beam systems.

Chapter 5

Cold-Fluid Theory of Equilibrium and Stability of a High-Intensity Periodically Twisted Ellipse-Shaped Charged-Particle Beam

5.1 Introduction

High-intensity ribbon (thin sheet) beams are of great interest for applications in particle accelerators, such as storage rings and rf and induction linacs, as well as vacuum electron devices, such as klystrons and traveling-wave tubes with periodic permanent magnet (PPM) focusing. They have the following remarkable properties. First, they can transport large amounts of beam currents at reduced intrinsic space-charge forces and energies. Second, they couple efficiently to rectangular rf structures. The combination of the space charge reduction and efficient coupling allows efficient rf generation in vacuum electronic devices, and efficient acceleration in particle accelerators. Third, elliptic beams provide an additional adjustable parameter (e.g., the aspect ratio) which may be useful for better matching a beam into a periodic focusing channel, such as an alternating-gradient magnetic quadrupole focusing channel.

Although ribbon beams have been discussed in the literature for decades, the equilibrium of a high-intensity, space-charge-dominated beam with a large-aspect-ratio elliptic cross section has not been discovered until the present work. Sturrock [51] first suggested use of a periodic magnetic focusing consisting of an array of planar-wiggler magnets for rectilinear beams. Zhang, et al [52] had some modest success in the experimental demonstration of the transport of a low-intensity (10 A, 500 kV) sheet beam in a planar-wiggler magnetic field, and observed considerable beam loss. Researchers made use of the multiple-time-scale analysis and the

paraxial approximations to obtain the smooth-beam approximation of high-intensity ribbon-beam equilibria [53]-[56]. In the smooth-beam approximation, the effects of the planar-wiggler field [51], [52], or the periodic cusp magnetic (PCM) field [53], [54], or the hybrid of PCM and periodic quadrupole magnet (PQM) fields [55], [56], or the offset pole PCM field [56] are treated as some averaged focusing constants in the transverse directions. While the smooth-beam approximation yields simple results, the multiple-time-scale analysis requires time averaging, losing the detailed information about the beam dynamics. As a result, it does not provide adequate information about how to generate high-intensity ribbon beams in practice.

A widely used tool for the determination of evolution of the charged-particle beam systems is based on the rms beam description. The construction of self-consistent beam distributions with linear focusing forces is discussed in Ref. [57] and [58], such as Kapchinskij-Vladmirskij equilibrium [10], [69], [59], [60] in an alternating-gradient quadrupole magnetic focusing field and the periodically focused rigid-rotor Vlasov equilibrium [61], [62] in a periodic solenoid magnetic focusing field. For ultrahigh-brightness beams with negligibly small emittance, a cold-fluid theory can be used to examine the detailed information about the beam dynamics, especially the evolution of the density and flow velocity profiles [63]-[65], such as the cold-fluid corkscrewing equilibrium [62], [63] in a linear focusing channel consisting of solenoidal and quadrupole magnetic focusing fields.

In this chapter, we present a cold-fluid equilibrium theory of an ultrahigh-brightness, space-charge-dominated, large-aspect-ratio elliptic beam propagating through a non-axisymmetric periodic magnetic focusing field. A paraxial cold-fluid model is employed to derive generalized envelope equations which determine the equilibrium flow properties of ellipse-shaped beams with negligibly small emittance. A matched envelope solution is obtained numerically from the

generalized envelope equations, and the results show that the beam edges in both transverse directions are well confined, and that the angle of the beam ellipse exhibits a periodic small-amplitude twist. Two-dimensional (2D) particle-in-cell (PIC) simulations with our Periodic Focused Beam 2D (PFB2D) code show good agreement with the predictions of equilibrium theory as well as beam stability [65].

The organization of the present chapter is as follows. In Sec. 5.2, the cold-fluid equilibrium theory of a periodically twisted ellipse-shaped charged-particle beam is presented, and the generalized envelope equations are derived. In Sec. 5.3, two-dimensional particle-in-cell simulations of the equilibrium and stability of elliptic beams are discussed. The equilibrium theory is further verified using 3D OMNITRAK which computes the particle trajectories self-consistently. In Sec. 5.4, the designs of periodically twisted ellipse-shaped charged-particle beams for various applications are presented. In Sec. 5.5, a brief summary is given.

5.2 Cold-fluid equilibrium theory

We consider a high-intensity, space-charge-dominated beam in free space, in which kinetic (emittance) effects are negligibly small. The beam can be adequately described by cold-fluid equations. In the paraxial approximation, the steady-state cold-fluid equations for time-stationary flow ($\partial/\partial t = 0$) in cgs units are [61], [62]

$$\beta_b c \frac{\partial}{\partial s} n_b + \nabla_\perp \cdot (n_b \mathbf{V}_\perp) = 0, \tag{5.1}$$

$$\nabla_\perp^2 \phi = \beta_b^{-1} \nabla_\perp^2 A_z = -4\pi q n_b, \tag{5.2}$$

$$n_b\left(\beta_b c\frac{\partial}{\partial s}+\mathbf{V}_\perp\cdot\nabla_\perp\right)\mathbf{V}_\perp=\frac{qn_b}{\gamma_b m}\left[-\frac{1}{\gamma_b^2}\nabla_\perp\phi+\beta_b\hat{\mathbf{e}}_z\times\mathbf{B}_\perp^{ext}+\frac{\mathbf{V}_\perp}{c}\times B_z^{ext}(s)\hat{\mathbf{e}}_z\right], \tag{5.3}$$

where $s=z$, $\mathbf{x}_\perp=x\hat{\mathbf{e}}_x+y\hat{\mathbf{e}}_y$, $\nabla_\perp=\partial/\partial\mathbf{x}_\perp$, q and m are the particle charge and rest mass, respectively, n_b is the particle density, $\mathbf{V}_\perp$ is the transverse flow velocity, $\gamma_b=\left(1-\beta_b^2\right)^{-1/2}$ is the relativistic mass factor, use has been made of $\beta_z=V_z/c\cong\beta_b=const$, c is the speed of light in vacuum and the self-electric field $\mathbf{E}^{self}$ and self-magnetic field $\mathbf{B}^{self}$ are determined from the scalar potential ϕ and vector potential $A_z\hat{\mathbf{e}}_z$, i.e., $\mathbf{E}^{self}=-\nabla_\perp\phi$ and $\mathbf{B}^{self}=\nabla_\perp\times A_z\hat{\mathbf{e}}_z$.

For the beam dimensions small relative to the characteristic scale of magnetic variations, i.e., $(k_{0x}x)^2/6<<1$ and $(k_{0y}y)^2/6<<1$, a three-dimensional (3D) non-axisymmetric periodic magnetic field can be described to the lowest order in the transverse dimension as

$$\mathbf{B}^{ext}(\mathbf{x})\approx B_0\left[\frac{k_{0x}^2}{k_0}\cos(k_0s)x\hat{\mathbf{e}}_x+\frac{k_{0y}^2}{k_0}\cos(k_0s)y\hat{\mathbf{e}}_y-\sin(k_0s)\hat{\mathbf{e}}_z\right], \tag{5.4}$$

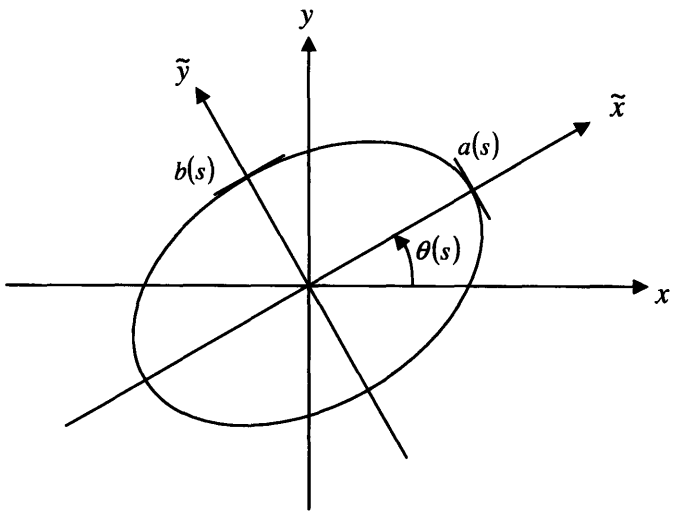

Fig. 5.1 Laboratory and twisted coordinate systems.

where $k_0 = 2\pi/S$, $k_{0x}^2 + k_{0y}^2 = k_0^2$, and S is the axial periodicity length. The 3D magnetic field in Eq. (5.4) is fully specified by the three parameters B_0, S and k_{0x}/k_{0y}.

We seek solutions to Eqs. (5.1)-(5.3) of the form

$$n_b(\mathbf{x}_\perp, s) = \frac{N_b}{\pi a(s) b(s)} \Theta\left[1 - \frac{\tilde{x}^2}{a^2(s)} - \frac{\tilde{y}^2}{b^2(s)}\right], \tag{5.5}$$

$$\mathbf{V}_\perp(\mathbf{x}_\perp, s) = [\mu_x(s)\tilde{x} - \alpha_x(s)\tilde{y}]\beta_b c\hat{\mathbf{e}}_{\tilde{x}} + [\mu_y(s)\tilde{y} + \alpha_y(s)\tilde{x}]\beta_b c\hat{\mathbf{e}}_{\tilde{y}}. \tag{5.6}$$

In Eqs. (5.5) and (5.6), $\mathbf{x}_\perp = \tilde{x}\hat{\mathbf{e}}_{\tilde{x}} + \tilde{y}\hat{\mathbf{e}}_{\tilde{y}}$ is a transverse displacement in the twisted coordinate system illustrated in Fig. 5.1; $\theta(s)$ is the twist angle of the ellipse; $\Theta(x) = 1$ if $x > 0$ and $\Theta(x) = 0$ if $x < 0$; and the functions $a(s)$, $b(s)$, $\mu_x(s)$, $\mu_y(s)$, $\alpha_x(s)$, $\alpha_y(s)$ and $\theta(s)$ are to be determined self-consistently.

Making use of the results in Eq. (3.26), we express the self-electric and self-magnetic fields for an elliptical beam with density distribution specified in Eq. (5.5) as

$$\phi = \beta_b^{-1} A_{\tilde{z}} = -\frac{2qN_b}{a+b}\left(\frac{\tilde{x}^2}{a} + \frac{\tilde{y}^2}{b}\right). \tag{5.7}$$

In obtaining (5.7) from Eq. (3.26), we have omitted the image charge contribution, because the beam is in free space. Substituting Eqs. (5.5) and (5.6) into Eq. (5.1) and expressing the result in terms of the tilde coordinates, we obtain

$$\begin{aligned}&\left(\mu_x + \mu_y - \frac{a'}{a} - \frac{b'}{b}\right)\Theta\left(1 - \frac{\tilde{x}^2}{a^2} - \frac{\tilde{y}^2}{b^2}\right) + 2\left[\left(\frac{a'}{a} - \mu_x\right)\frac{\tilde{x}^2}{a^2} + \left(\frac{b'}{b} - \mu_y\right)\frac{\tilde{y}^2}{b^2}\right.\\ &\left. + \left(-\frac{b}{a}\theta' + \frac{a}{b}\theta' + \frac{b}{a}\alpha_x - \frac{a}{b}\alpha_y\right)\frac{\tilde{x}}{a}\frac{\tilde{y}}{b}\right]\delta\left(1 - \frac{\tilde{x}^2}{a^2} - \frac{\tilde{y}^2}{b^2}\right) = 0,\end{aligned} \tag{5.8}$$

where prime denotes $\partial/\partial s$, and the relations $\tilde{x}' = \tilde{y}\theta'$, $\tilde{y}' = -\tilde{x}\theta'$, $\partial \mathbf{e}_{\tilde{x}}/\partial s = \mathbf{e}_{\tilde{y}}\theta'$ and $\partial \mathbf{e}_{\tilde{y}}/\partial s = -\mathbf{e}_{\tilde{x}}\theta'$ have been used. Since Eq. (5.8) must be satisfied for all $\tilde{x}$ and $\tilde{y}$, the coefficients of the terms proportional to Θ, $\tilde{x}^2\delta$, $\tilde{y}^2\delta$ and $\tilde{x}\tilde{y}\delta$ must vanish independently. This leads to the following equations

$$\mu_x = \frac{1}{a}\frac{da}{ds}, \tag{5.9}$$

$$\mu_y = \frac{1}{b}\frac{db}{ds}, \tag{5.10}$$

$$\frac{d\theta}{ds} = \frac{a^2\alpha_y - b^2\alpha_y}{a^2 - b^2}. \tag{5.11}$$

The force balance equation Eq. (5.3) represents two equations, one in the direction $\mathbf{e}_{\tilde{x}}$ and the other in the $\mathbf{e}_{\tilde{y}}$ directions. Substituting Eqs. (5.4)-(5.7) into Eq. (5.3), the two equations can be expressed as

$$f_x\tilde{x} + g_y\tilde{y} = 0, \tag{5.12}$$

$$g_x\tilde{x} + f_y\tilde{y} = 0, \tag{5.13}$$

where

$$f_x = \mu_x^{\,2} + \mu_x' - \alpha_x\alpha_y + (\alpha_x - \alpha_y)\theta' - \frac{2K}{(a+b)} - 2\sqrt{\kappa_{z0}}\sin(k_0 s)\alpha_y + \sqrt{\kappa_{z0}}\frac{k_{0x}^2 - k_{0y}^2}{k_0}\sin(2\theta)\cos(k_0 s), \tag{5.14}$$

$$f_y = \mu_y^{\,2} + \mu_y' - \alpha_x\alpha_y - (\alpha_x - \alpha_y)\theta' - \frac{2K}{(a+b)} + 2\sqrt{\kappa_{z0}}\sin(k_0 s)\alpha_x + \sqrt{\kappa_{z0}}\frac{k_{0x}^2 - k_{0y}^2}{k_0}\sin(2\theta)\cos(k_0 s), \tag{5.15}$$

$$g_x = \alpha_y' + (\mu_x - \mu_y)\theta' + (\mu_x + \mu_y)\alpha_y - 2\sqrt{\kappa_{z0}}\left(\frac{k_{0x}^2}{k_0}\cos^2\theta + \frac{k_{0y}^2}{k_0}\sin^2\theta\right)\cos(k_0 s) - 2\sqrt{\kappa_{z0}}\mu_x \sin(k_0 s), \tag{5.16}$$

$$g_y = -\alpha_x' + (\mu_x - \mu_y)\theta' - (\mu_x + \mu_y)\alpha_x + 2\sqrt{\kappa_{z0}}\left(\frac{k_{0x}^2}{k_0}\sin^2\theta + \frac{k_{0y}^2}{k_0}\cos^2\theta\right)\cos(k_0 s) + 2\sqrt{\kappa_{z0}}\mu_y \sin(k_0 s). \tag{5.17}$$

Since Eq. (5.12) and (5.13) must be satisfied for all $\tilde{x}$ and $\tilde{y}$, the coefficients of the terms proportional to $\tilde{x}$ and $\tilde{y}$ must vanish independently, which lead to

$$f_x = 0, \tag{5.18}$$

$$f_y = 0, \tag{5.19}$$

$$g_x = 0, \tag{5.20}$$

$$g_y = 0. \tag{5.21}$$

Substituting Eqs. (5.9)-(5.11) into Eqs. (5.18)-(5.21), we obtain the following generalized envelope equations

$$\frac{d^2 a}{ds^2} - \left[\frac{b^2(\alpha_x^2 - 2\alpha_x\alpha_y) + a^2\alpha_y^2}{a^2 - b^2} + \sqrt{\kappa_{z0}}\frac{k_{0x}^2 - k_{0y}^2}{k_0}\cos(k_0 s)\sin(2\theta) - 2\sqrt{\kappa_{z0}}\alpha_y \sin(k_0 s)\right]a - \frac{2K}{a+b} = 0, \tag{5.22}$$

$$\frac{d^2 b}{ds^2} + \left[\frac{a^2(\alpha_y^2 - 2\alpha_x\alpha_y) + b^2\alpha_x^2}{a^2 - b^2} + \sqrt{\kappa_{z0}}\frac{k_{0x}^2 - k_{0y}^2}{k_0}\cos(k_0 s)\sin(2\theta) + 2\sqrt{\kappa_{z0}}\alpha_x \sin(k_0 s)\right]b - \frac{2K}{a+b} = 0, \tag{5.23}$$

$$\frac{d}{ds}(a^2\alpha_y) - \frac{ab^3(\alpha_x - \alpha_y)}{a^2 - b^2}\frac{d}{ds}\left(\frac{a}{b}\right) - 2\sqrt{\kappa_{z0}}\cos(k_0 s)\frac{k_{0x}^2\cos^2\theta + k_{0y}^2\sin^2\theta}{k_0}a^2 - 2\sqrt{\kappa_{z0}}a\frac{da}{ds}\sin(k_0 s) = 0, \tag{5.24}$$

$$\frac{d}{ds}\left(b^2\alpha_x\right)-\frac{a^3b\left(\alpha_x-\alpha_y\right)}{a^2-b^2}\frac{d}{ds}\left(\frac{b}{a}\right)-2\sqrt{\kappa_{z0}}\cos\left(k_0s\right)\frac{k_{0x}^2\sin^2\theta+k_{0y}^2\cos^2\theta}{k_0}b^2-2\sqrt{\kappa_{z0}}b\frac{db}{ds}\sin\left(k_0s\right)=0, \tag{5.25}$$

$$\frac{d\theta}{ds}=\frac{a^2\alpha_y-b^2\alpha_x}{a^2-b^2}, \tag{5.26}$$

where

$$\sqrt{\kappa_{z0}}\equiv\frac{qB_0}{2\gamma_b\beta_bmc^2}\text{ and }K\equiv\frac{2q^2N_b}{\gamma_b^3\beta_b^3mc^2}. \tag{5.27}$$

Equations (5.22)-(5.26) have "time" reversal symmetry under the transformation $\left(s,a,b,a',b',\alpha_x,\alpha_y,\theta\right)\rightarrow\left(-s,a,b,-a',-b',-\alpha_x,-\alpha_y,\theta\right)$. This implies that the dynamical system described by Eqs. (5.22)-(5.26) has the hyper symmetry plane $\left(a',b',\alpha_x,\alpha_y\right)$.

A numerical module in the PFB2D code has been developed to solve the generalized envelope equations (5.22)-(5.26). There are, in total, seven functions $a(s)$, $b(s)$, $a'(s)$, $b'(s)$, $\alpha_x(s)$, $\alpha_x(s)$ and $\theta(s)$ to be determined. The time reserval symmetry of the dynamical system requires the quantities $\left(a',b',\alpha_x,\alpha_y\right)$ vanish at $s=0$ for matched solutions. Therefore, only the three initial values $a(0)$, $b(0)$ and $\theta(0)$ corresponding to a matched solution need to be determined with Newton's method. Detailed numerical results will be presented in Sec. 5.4.

5.3 PIC simulation and OMNITRAK simulation

The beam equilibria predicted by the generalized envelope equations are verified by 2D PIC simulations using the PFB2D code which is described in Chapter 4. In the PFB2D simulations, we use the paraxial field in Eq. (5.4), typically 5×10^5 particles, a square grid with 400×400

cells, and a square conducting pipe with a full width which is 3 times the semi major axis of the beam. Such a square conducting pipe is sufficient to assume nearly free space propagation in which the image-charge effects are negligibly small. The results simulated by the PIC PFB2D code are in excellent agreement with the solutions of the generalized envelope equations. In addition, in PIC simulations, the density profile is measured and it remains uniform density profile as it evolves along time. We will demonstrate the PIC simulation for each design of the elliptic beams in Sec 5.4.

OMNITRAK [66], a commercial software produced by Field Precision, is a 3-dimensional self-consistent particle trajectory code which is used to study charged-particle orbits and collective beam physics in electric and magnetic fields. OMNITRAK is used to simulate a space-charge-dominated beam of large-aspect-ratio elliptic cross-section propagating in a non-axisymmetric periodic permanent magnet focusing field. The simulation results confirm theoretical predictions in the paraxial limit. We will present the 3D OMNITRAK simulation of an intense elliptic beam for a ribbon-beam amplifier in Sec. 5.4.1 [65].

5.4 Designs of periodically twisted ellipse-shaped charged-particle beams

High-intensity periodically twisted elliptic beam equilibria exist over a wide region of parameters ranging from the nonrelativistic to relativistic regimes. As examples, three potential applications are listed in Table 5.1. The nonrelativistic elliptic beam corresponds to a beam design for a high-efficiency 200 W ribbon-beam amplifier (RBA) which is being developed at Massachusetts Institute of Technology (MIT) and Beam Power Technology proposed for wireless communications. The mildly relativistic elliptic beam is proposed for a high-power,

high-efficiency RBA for radar applications. The relativistic elliptic beam is proposed to be used in a 10 MW L-Band ribbon-beam klystron (RBK) for the International Linear Collider (ILC).

Table 5.1 System parameters for elliptic-beam examples

Parameter	Nonrelativistic	Mildly Relativistic	Fully Relativistic
Application	Wireless Communication	Missile Defense	International Linear Collider
Frequency (GHz)	1.95	2.8	1.3
RF Power (kW)	0.2 (cw)	500 (pulsed)	10,000 (pulsed)
Current (A)	0.11	18.5	85.5
Voltage (kV)	2.29	45.0	198.5
S (cm)	1.912	2.626	2.2
k_{0x}/k_{0y}	1.60	1.44	1.52
B_0 (kG)	0.337	1.099	2.40
a/b	6.0	4.0	5.0
a (cm)	0.373	0.585	0.425
θ_{max} (deg)	10.4	11.5	8.8

5.4.1 Design of a nonrelativistic elliptic beam

As an example of a nonrelativistic elliptic beam, we consider a beam with voltage $V_b = 2290$ eV , current $I_b = 0.11$ A, aspect ratio $a/b = 6$, and a non-axisymmetric periodic permanent magnet focusing with $B_0 = 337$ G , $S = 1.912$ cm , and $k_{0y}/k_{0x} = 1.6$ (see Table 1, Column 2). For such a system, the matched solution of the generalized envelope equations (5.22)-(5.26) is calculated numerically as shown in Figs. 5.2(a)-5.2(c) (solid curves) with the corresponding parameters: $k_{0x} = 1.90$ cm^{-1} , $k_{0y} = 3.03$ cm^{-1} , $\sqrt{\kappa_{z0}} = 1.04$ cm^{-1} , and $K = 1.52\times10^{-2}$. The solution to the generalized envelope equations (5.22)-(5.26), displayed as solid and dashed curves in Fig. 5.2, shows that the semiaxes of the elliptical beam remain almost constant with small oscillations, that the orientation of the ellipse twists periodically with an amplitude of ten degrees, and that the normalized rotation flow velocities α_x and α_y oscillate with the magnet periodicity. It is worthwhile pointing out that the normalized velocities μ_x, μ_y, α_x and α_y vanish at $s = 0$ which makes it a natural matching point for a parallel-flow elliptic beam from an elliptic diode [64].

Shown in Figs. 5.2(a) and 5.2(b), the dotted curves are the envelopes and angle of the beam ellipse obtained from the PFB2D simulation for the nonrelativistic elliptic beam. In the simulation, the emittance is set to be negligibly small in order to demonstrate the cold-fluid approximation. As shown in Fig. 5.2, there is excellent agreement between the theoretical envelope solution (solid curves) and the self-consistent PIC simulation results (dotted curves).

The PFB2D simulation also shows that the transverse beam distribution preserves the equilibrium profile as it propagates. In Fig. 5.3, 5,000 particles (a sample of the 5×10^5 particles

in the PFB2D simulation) are plotted in the planes (x, y) and $(x, dy/ds)$ for five snapshots within one period: $s/S = 9.0, 9.25, 9.5, 9.75$ and 10.0 for the same elliptic beam shown in Fig. 5.2. This also suggests that the beam equilibrium is stable.

The 3D OMNITRAK is used to further simulate the nonrelativistic elliptic beam. The OMNITRAK simulation results further confirm theoretical predictions in the paraxial limit [65]. There is small discrepancy between the analytic envelope solution and the OMNITRAK simulation in the envelope oscillations, which is due to a small mismatch induced by 3D effects. The small mismatch can be eliminated by making slight adjustments to the envelope solutions, via an iterative procedure using OMNITRAK simulations.

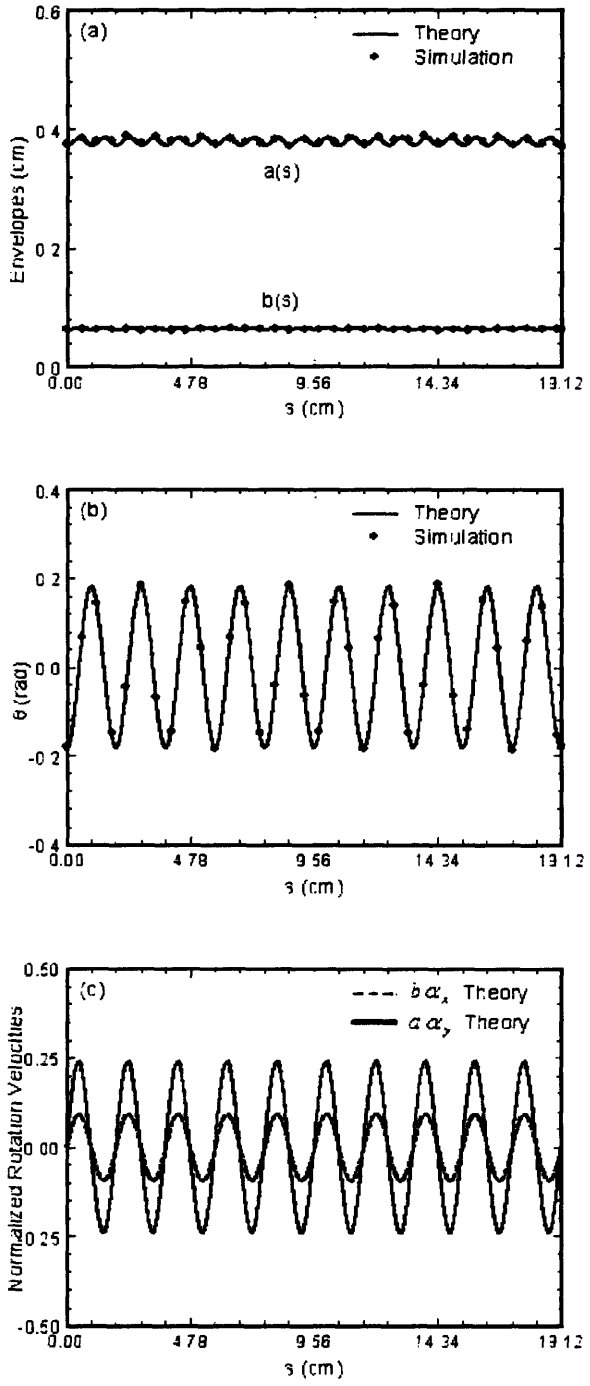

Figure 5.2 Plots of (a) envelopes $a(s)$ and $b(s)$, (b) twist angle $\theta(s)$ $\theta(s)$, and (c) normalized rotational velocities $b(s)\alpha_x(s)$ and $a(s)\alpha_y(s)$ versus the axial distance s for the nonrelativistic twisted ellipse-shaped beam in Table 1 (Column 2). The solid and dashed curves are the generalized envelope solution, whereas the dotted curves are from the PFB2D simulation.

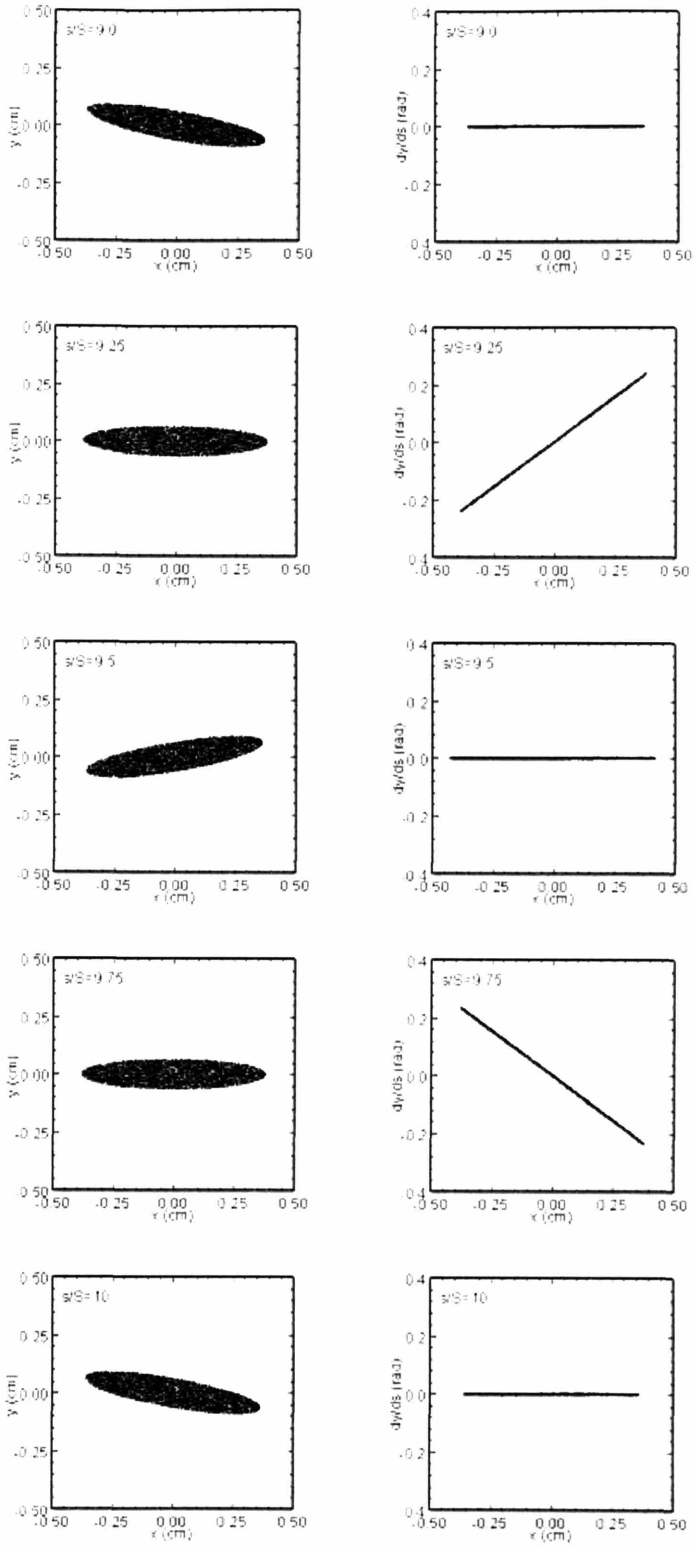

Figure 5.3 Plots of 5,000 particles (a sample of the 5×10^5 particles in the PFB2D simulation) in the planes (x, y) and $(x, dy/ds)$ for five snapshots within one period: $s/S = 9.0,\ 9.25,\ 9.5,\ 9.75$ and 10.0 for the same elliptic beam shown in Fig. 5. 2.

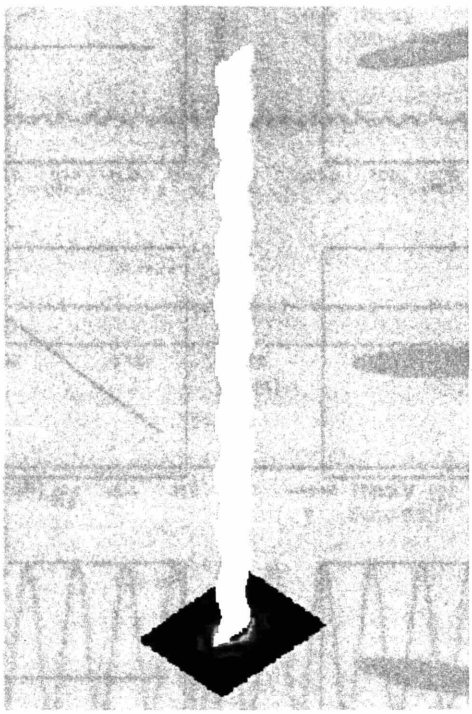

Figure 5.4 3D OMNITRAK simulation of the nonrelativistic twisted ellipse-shaped beam in Table 1 (Column 2).

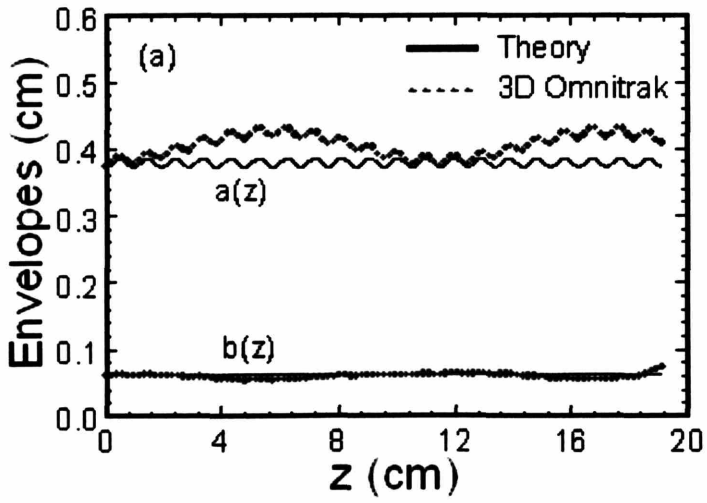

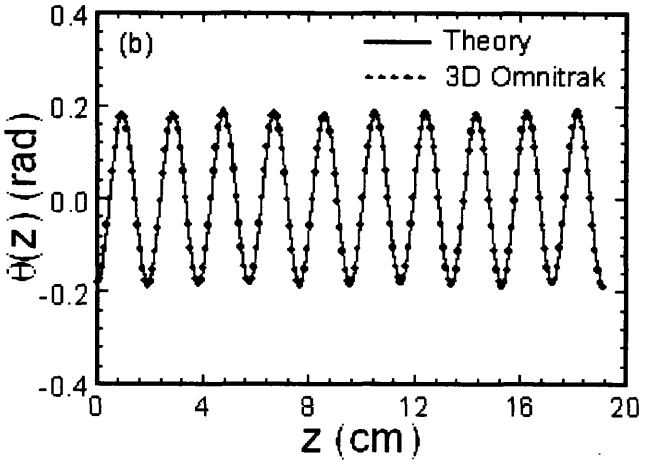

Figure 5.5 Plots of (a) envelopes $a(s)$ and $b(s)$, (b) twist angle $\theta(s)$ versus the axial distance s for the nonrelativistic twisted ellipse-shaped beam in Table 1 (Column 2). The solid and dashed curves are the generalized envelope solution, whereas the dotted curves are from the 3D OMNITRAK simulation.

5.4.2 Design of a relativistic elliptic beam

As an example of a relativistic elliptic beam, we consider a relativistic beam with voltage $V_b = 198.5$ keV, current $I_b = 85.5$ A, aspect ratio $a/b = 5$, and a non-axisymmetric periodic permanent magnet focusing field with $B_0 = 2.4$ kG, $S = 2.2$ cm, and $k_{0y}/k_{0x} = 1.52$ (see Table 1, Column 4). For such a system the matched solution of the generalized envelope equations (5.22)-(5.26) is calculated numerically as shown in Figs. 5.5(a)-5.5(c) (solid curves) with the corresponding parameters: $k_{0x} = 1.57$ cm^{-1}, $k_{0y} = 2.39$ cm^{-1}, $\sqrt{\kappa_{\perp 0}} = 0.732$ cm^{-1}, and $K = 1.13\times10^{-2}$. The solution to the generalized envelope equations (5.22)-(5.26), displayed as solid and dashed curves in Fig. 5.5, shows that the semiaxes of the elliptical beam remain almost

constant with small oscillations, that the orientation of the ellipse twists periodically with an amplitude of ten degrees, and that the normalized rotation flow velocities α_x and α_y oscillate with the magnet periodicity. It is worthwhile pointing out that the normalized velocities μ_x, μ_y, α_x and α_y vanish at $s = 0$.

Shown in Figs. 5.5(a) and 5.5(b), the dotted curves are the envelopes and angle of the beam ellipse obtained from the PFB2D simulation for the fully relativistic elliptic beam. In the simulation, the emittance is set to be negligibly small in order to demonstrate the cold-fluid approximation. As shown in Fig. 5.5, there is excellent agreement between the theoretical envelope solution (solid curves) and the self-consistent PIC simulation results (dotted curves).

The PFB2D simulation also shows that the transverse beam distribution preserves the equilibrium profile as it propagates. In Fig. 5.6, 10,000 particles (a sample of the 5×10^5 particles in the PFB2D simulation) are plotted in the planes (x, y) and $(x, dy/ds)$ for five snapshots within one period: $s/S = 9.0, 9.25, 9.5, 9.75$ and 10.0 for the same elliptic beam shown in Fig. 5.5. The preservation of the beam distribution is further demonstrated in Fig. 5.7, which displays the evolution of the normalized fourth moments $\langle x^4\rangle/\langle x^2\rangle^2$ and $\langle y^4\rangle/\langle y^2\rangle^2$ for the same beam shown in Fig. 5.5. In Fig. 5.7, it is evident that the normalized fourth moments $\langle x^4\rangle/\langle x^2\rangle^2$ and $\langle y^4\rangle/\langle y^2\rangle^2$, which are both equal to 2 for a uniform-density distribution, remain to be 2 within $\pm 1\%$ as the beam propagates for ten periods. The PIC simulation results suggest that the beam equilibrium is stable, as in the case of the nonrelativistic elliptic beam.

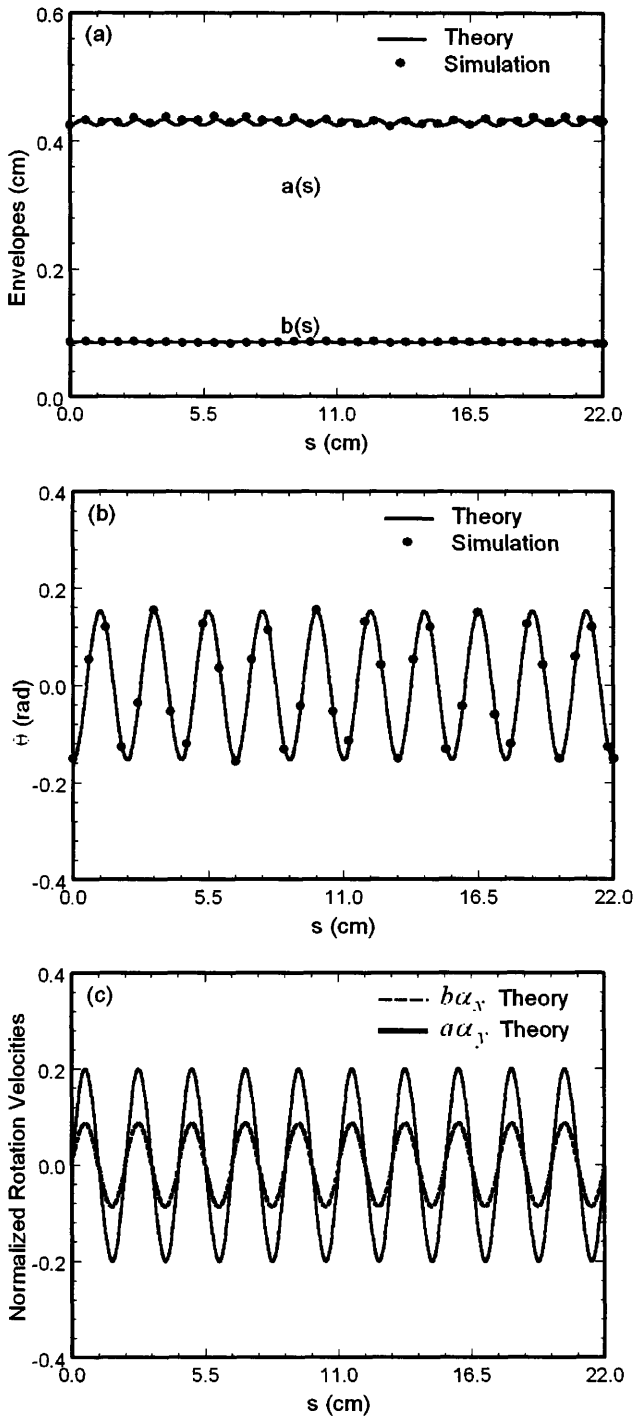

Figure 5.5 Plots of (a) envelopes $a(s)$ and $b(s)$, (b) twist angle $\theta(s)$, and (c) normalized rotational velocities $b(s)\alpha_x(s)$ and $a(s)\alpha_y(s)$ versus the axial distance for the fully relativistic twisted ellipse-shaped beam in Table 1 (Column 4). The solid and dashed curves are the generalized envelope solution, whereas the dotted curves are from the PFB2D simulation.

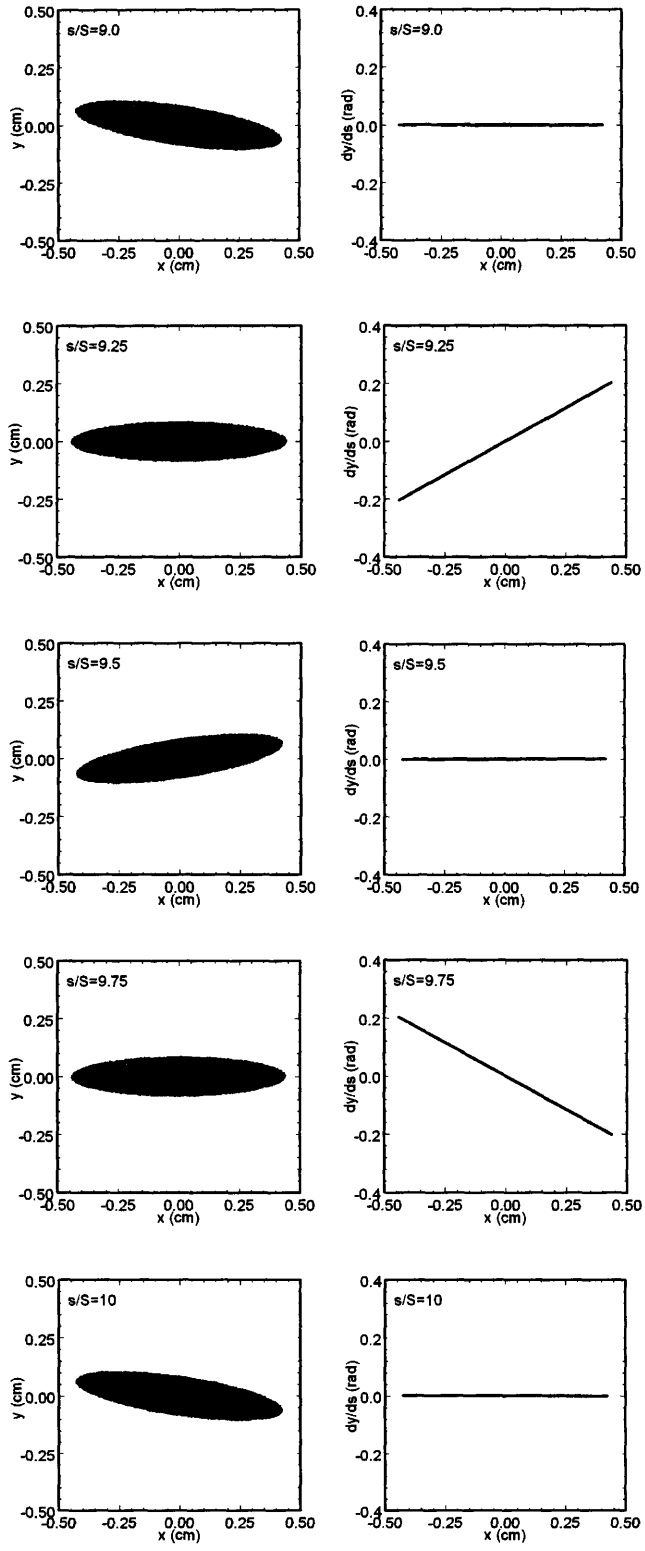

Figure 5.6 Plots of 10,000 particles (a sample of the 5×10^5 particles in the PFB2D simulation) in the planes (x, y) and $(x, dy/ds)$ for five snapshots within one period: $s/S = 9.0,\ 9.25,\ 9.5,\ 9.75$ and 10.0 for the same elliptic beam shown in Fig. 5.2.

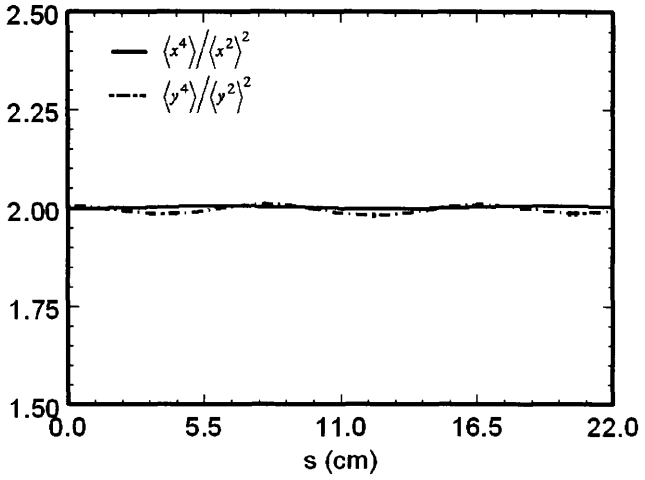

Fig. 5.7 Plots of the evolution of normalized fourth moments $\langle x^4\rangle/\langle x^2\rangle^2$ and $\langle y^4\rangle/\langle y^2\rangle^2$ for the same elliptic beam shown in Fig. 5.5.

5.5 Summary

A novel exact paraxial cold-fluid equilibrium has been found for a high-intensity, space-charge-dominated charged-particle beam with a periodically twisted elliptic cross section in a non-axisymmetric periodic magnetic field. Generalized envelope equations, which determine the beam envelopes, ellipse orientation, density, and internal flow velocity profiles, have been derived, and solved numerically in both the nonrelativistic and relativistic regimes. The equilibrium and stability of such beams have been demonstrated by self-consistent two-dimensional particle-in-cell PFB2D simulations. We anticipate that the equilibrium theory will provide a valuable tool in the design of high-intensity elliptic beams in novel vacuum electron devices, especially for ribbon-beam amplifiers and ribbon-beam klystrons. The ellipse-shaped

beam equilibrium may provide some flexibility in the design and operation of high-intensity accelerators.

Chapter 6

Vlasov Equilibrium of a High-Intensity Periodically Twisted Ellipse-Shaped Charged-Particle Beam

6.1 Introduction

A fundamental understanding of the kinetic equilibrium and stability properties high-intensity electron and ion beams in periodic focusing fields plays a central role in the design and operation of particle accelerators, such as storage rings and rf and induction linacs, as well as vacuum electron devices, such as klystrons and traveling-wave tubes with periodic permanent magnet (PPM) focusing. There are two well-known equilibria for periodically focused intense beams, namely, the Kapchinskij-Vladmirskij equilibrium [10], [59] in an alternating-gradient quadrupole magnetic focusing field and the periodically focused rigid-rotor Vlasov equilibrium [69][60] in a periodic solenoid magnetic focusing field. More generally, the self-consistent beam distributions can be constructed with linear focusing forces as discussed in Refs. [57] and [58].

These previously known Vlasov equilibria for high-intensity charged-particle beams propagating in the alternating-gradient quadrupole magnetic focusing field or the periodic solenoid magnetic focusing field charged-particle beams are circular on average; that is, the averages of the beam envelopes in different transverse directions over one period are the same.

In this chapter, it is shown that there exists a Vlasov equilibrium for a periodically twisted large-aspect-ratio intense charged-particle beam with a uniform density in the transverse direction propagating through a non-axisymmetric periodic magnetic focusing field. The single-particle Hamiltonian of such a periodically twisted large-aspect-ratio elliptic beam is investigated

self-consistently. A new constant of motion is found such that the self-consistent elliptic beam Vlasov equilibrium can be constructed as a function of the constant of motion. The beam envelope equations and flow velocity equations are derived. They are consistent with the generalized envelope equations derived from the cold-fluid theory [65] when the temperature is taken to be zero. Statistical properties and possible applications of the present elliptic beam Vlasov equilibrium are discussed.

6.2 Vlasov equilibrium theory

We consider an ellipse-shaped, continuous, intense charged-particle beam propagating with constant axial velocity $\beta_b c\mathbf{e}_z$ through an applied non-axisymmetic periodic magnetic focusing field. As in Sec. 5.2, the applied non-axisymmetic periodic magnetic focusing field inside a thin beam with $k_{0x}^2 a^2/6 << 1$ and $k_{0y}^2 b^2/6 << 1$ can be approximated by

$$\mathbf{B}^{\text{ext}} \cong B_0\left[\frac{k_{0x}{}^2}{k_0}\cos(k_0 s)x\mathbf{e}_x + \frac{k_{0y}{}^2}{k_0}\cos(k_0 s)y\mathbf{e}_y - \sin(k_0 s)\mathbf{e}_z\right], \tag{6.1}$$

where $s = z$ is the axial coordinate. The associated magnetic vector potential can be expressed as

$$\mathbf{A}^{\text{ext}} = -B_0\sin(k_0 s)\left[-\frac{k_{0x}{}^2}{k_0{}^2}y\mathbf{e}_x + \frac{k_{0y}{}^2}{k_0{}^2}x\mathbf{e}_y\right], \tag{6.2}$$

which gives $\mathbf{B}^{ext} = \nabla\times\mathbf{A}^{ext}$.

To determine the self-electric and self-magnetic fields of the elliptic beam self-consistently, we assume that the density profile of the beam is uniform inside the beam boundary, i.e.,

$$n_b(x,y,s)=\begin{cases}\dfrac{N_b}{\pi a(s)b(s)}, & \dfrac{\tilde{x}^2}{a^2(s)}+\dfrac{\tilde{y}^2}{b^2(s)}\le 1,\\ 0, & \textit{otherwise},\end{cases} \tag{6.3}$$

where

$$\tilde{x}=x\cos[\theta(s)]+y\sin[\theta(s)] \tag{6.4}$$

and

$$\tilde{y}=-x\sin[\theta(s)]+y\cos[\theta(s)] \tag{6.5}$$

are the twisted coordinates as illustrated in Fig. 5.1. The density of the elliptic beam with semi-major axis $a(s)=a(s+S)$ and semi-minor axis $b(s)=b(s+S)$ is uniform in the beam interior ($\tilde{x}^2/a^2+\tilde{y}^2/b^2\le 1$). The semi-major and semi-minor axes have the same periodicity $S=2\pi/k_0$ as the applied magnetic field. $N_b=\int_{-\infty}^{\infty}dxdyn_b(x,y,s)=\text{const}$ is the number of particles per unit axial length. In the paraxial approximation, the Budker parameter of the beam is assumed to be small, i.e., $q^2N_b/mc^2<<\gamma_b$, and the transverse kinetic energy of a beam particle is assumed to be small compared with its axial kinetic energy. Here, c is the speed of light in *vacuo*, $\gamma_b=\left(1-\beta_b^2\right)^{-1/2}$ is the relativistic mass factor, q and m are the particle charge and rest mass, respectively.

From the equilibrium Maxwell equations, we find that the self-electric and self-magnetic fields, $\mathbf{E}^{self}$ and $\mathbf{B}^{self}$, are given by

$$\mathbf{E}^{self}(\tilde{x},\tilde{y},s)=\frac{2qN_b}{a(s)+b(s)}\left[\frac{\tilde{x}}{a(s)}\mathbf{e}_{\tilde{x}}+\frac{\tilde{y}}{b(s)}\mathbf{e}_{\tilde{y}}\right] \tag{6.6}$$

and

$$\beta_b^{-1}\mathbf{B}^{self}(\tilde{x},\tilde{y},s)=\frac{2qN_b}{a(s)+b(s)}\left[-\frac{\tilde{y}}{b(s)}\mathbf{e}_{\tilde{x}}+\frac{\tilde{x}}{a(s)}\mathbf{e}_{\tilde{y}}\right] \tag{6.7}$$

in the beam interior ($\tilde{x}^2/a^2+\tilde{y}^2/b^2\le 1$). It is convenient to express the self-fields in terms of the scalar and vector potentials defined for $\tilde{x}^2/a^2+\tilde{y}^2/b^2\le 1$ by

$$\phi^{self}(\tilde{x},\tilde{y},s)=\beta_b^{-1}A_z^{self}(\tilde{x},\tilde{y},s)=-\frac{2qN_b}{a(s)+b(s)}\left[\frac{\tilde{x}^2}{a(s)}+\frac{\tilde{y}^2}{b(s)}\right] \tag{6.8}$$

and

$$\mathbf{A}^{self}(\tilde{x},\tilde{y},s)=A_z^{self}(\tilde{x},\tilde{y},s)\mathbf{e}_z. \tag{6.9}$$

The results are

$$\mathbf{E}^{self}(\tilde{x},\tilde{y},s)=-\left(\frac{\partial\phi^{self}}{\partial\tilde{x}}\mathbf{e}_{\tilde{x}}+\frac{\partial\phi^{self}}{\partial\tilde{y}}\mathbf{e}_{\tilde{y}}\right) \tag{6.10}$$

and

$$\mathbf{B}^{self}=\frac{\partial A_z^{self}}{\partial\tilde{y}}\mathbf{e}_{\tilde{x}}-\frac{\partial A_z^{self}}{\partial\tilde{x}}\mathbf{e}_{\tilde{y}}. \tag{6.11}$$

In the paraxial approximation, the transverse motion for an individual particle in the combined self fields and applied magnetic field is described by the normalized perpendicular Hamiltonian

$\hat{H}_\perp=H_\perp/\gamma_b\beta_b mc^2$,

$$\hat{H}_{\perp}(x,y,P_x,P_y,s)=\frac{1}{2}\left\{\left[P_x+\sqrt{\kappa_z(s)}\frac{k_{0y}^2}{k_0^2}y\right]^2+\left[P_y-\sqrt{\kappa_z(s)}\frac{k_{0x}^2}{k_0^2}x\right]^2\right\}$$
$$-\frac{K}{a(s)+b(s)}\left\{\frac{[x\cos\theta(s)+y\sin\theta(s)]^2}{a(s)}+\frac{[-x\sin\theta(s)+y\cos\theta(s)]^2}{b(s)}\right\}. \tag{6.12}$$

In Eq. (6.18), (x,P_x) and (y,P_y) are canonical conjugate pairs, $\sqrt{\kappa_z(s)}=qB_z(s)/2\gamma_b\beta_b mc^2$, $K=2q^2N/\gamma_b^3\beta_b^2mc^2$ is the self-field perveance, $\gamma_b=(1-\beta_b^2)^{-1/2}$ is the relativistic mass factor, and the normalized transverse canonical momentum $\mathbf{P}_{\perp}=(P_x,P_y)$ is related to the transverse mechanical momentum $\mathbf{p}_{\perp}$ by $\mathbf{P}_{\perp}=(\gamma_b\beta_b mc)^{-1}(\mathbf{p}_{\perp}+q\mathbf{A}_{\perp}^{\text{ext}}/c)$.

It is convenient to transform the Hamiltonian from the Cartesian canonical variables (x,y,P_x,P_y) to new canonical variables (x_1,y_1,P_{x1},P_{y1}), so that the new Hamiltonian assumes a simpler form from which the invariants of the motion are easily identified.

The transformation of the Hamiltonian from the Cartesian canonical variables (x,y,P_x,P_y) to the new canonical variables (x_1,y_1,P_{x1},P_{y1}) involves two steps. We first transform the Cartesian canonical variables (x,y,P_x,P_y) to twisted canonical variables $(\tilde{x},\tilde{y},\tilde{P}_x,\tilde{P}_y)$ using the generating function

$$F_2(x,y;\tilde{P}_x,\tilde{P}_y,s)=\tilde{P}_x\{x\cos[\theta(s)]+y\sin[\theta(s)]\}+\tilde{P}_y\{-x\sin[\theta(s)]+y\cos[\theta(s)]\}. \tag{6.13}$$

It follows from Eq. (6.13) that

$$P_x=\frac{\partial F_2}{\partial x}=\tilde{P}_x\cos[\theta(s)]-\tilde{P}_y\sin[\theta(s)], \tag{6.14}$$

$$P_y = \frac{\partial F_2}{\partial y} = \tilde{P}_x \sin[\theta(s)] + \tilde{P}_y \cos[\theta(s)], \tag{6.15}$$

$$\tilde{x} = \frac{\partial F_2}{\partial \tilde{P}_x} = x\cos[\theta(s)] + y\sin[\theta(s)], \tag{6.16}$$

$$\tilde{y} = \frac{\partial F_2}{\partial \tilde{P}_y} = -x\sin[\theta(s)] + y\cos[\theta(s)]. \tag{6.17}$$

The Hamiltonian in the twisted canonical variables is then expressed as

$$\begin{aligned}
\tilde{H}_\perp(\tilde{x},\tilde{y},\tilde{P}_x,\tilde{P}_y,s) &= \hat{H}_\perp(x,y,P_x,P_y,s) + \frac{\partial F_2}{\partial s} \\
&= \frac{1}{2}\left\{\tilde{P}_x\cos[\theta(s)] - \tilde{P}_y\sin[\theta(s)] + \sqrt{\kappa_z(s)}\frac{k_{0y}^2}{k_0^2}\tilde{x}\sin[\theta(s)] + \sqrt{\kappa_z(s)}\frac{k_{0y}^2}{k_0^2}\tilde{y}\cos[\theta(s)]\right\}^2 \\
&+ \frac{1}{2}\left\{\tilde{P}_x\sin[\theta(s)] + \tilde{P}_y\cos[\theta(s)] - \sqrt{\kappa_z(s)}\frac{k_{0x}^2}{k_0^2}\tilde{x}\cos[\theta(s)] + \sqrt{\kappa_z(s)}\frac{k_{0x}^2}{k_0^2}\tilde{y}\sin[\theta(s)]\right\}^2 \\
&- \frac{K}{a(s)+b(s)}\left[\frac{\tilde{x}^2}{a(s)} + \frac{\tilde{y}^2}{b(s)}\right] - (\tilde{x}\tilde{P}_y - \tilde{y}\tilde{P}_x)\frac{d\theta(s)}{ds}.
\end{aligned} \tag{6.18}$$

The equations of motion associated with the Hamiltonian in Eq. (6.18) are

$$\tilde{x}' = \frac{\partial \tilde{H}_\perp}{\partial P_{\tilde{x}}} = P_{\tilde{x}} + C(s)\tilde{x} + [\theta'(s) - \alpha_x(s)]\tilde{y}, \tag{6.19}$$

$$\tilde{y}' = \frac{\partial \tilde{H}_\perp}{\partial P_{\tilde{y}}} = P_{\tilde{y}} - C(s)\tilde{y} - [\theta'(s) - \alpha_y(s)]\tilde{x}, \tag{6.20}$$

$$\begin{aligned}
P_{\tilde{x}}' = -\frac{\partial \tilde{H}_\perp}{\partial \tilde{x}} &= -\left\{\kappa_z(s)\frac{k_{0x}^4\cos^2[\theta(s)] + k_{0y}^4\sin^2[\theta(s)]}{k_0^4} - \frac{2K}{a(s)[a(s)+b(s)]}\right\}\tilde{x} \\
&- C(s)P_{\tilde{x}} + [\theta'(s) - \alpha_y(s)]P_{\tilde{y}} - \kappa_z(s)\left(\frac{k_{0y}^4 - k_{0x}^4}{k_0^4}\right)\frac{\sin[2\theta(s)]}{2}\tilde{y},
\end{aligned} \tag{6.21}$$

$$P_{\tilde{y}}' = -\frac{\partial \tilde{H}_{\perp}}{\partial \tilde{y}} = -\left\{ \kappa_z(s) \frac{k_{0x}^4 \sin^2[\theta(s)] + k_{0y}^4 \cos^2[\theta(s)]}{k_0^4} - \frac{2K}{b(s)[a(s)+b(s)]} \right\} \tilde{y}$$
$$+ C(s) P_{\tilde{y}} - [\theta'(s) - \alpha_x(s)] P_{\tilde{x}} - \kappa_z(s) \left(\frac{k_{0y}^4 - k_{0x}^4}{k_0^4} \right) \frac{\sin[2\theta(s)]}{2} \tilde{x}, \tag{6.22}$$

where prime denotes derivative with respect to s,

$$C(s) \equiv \sqrt{\kappa_z(s)} \frac{k_{0y}^2 - k_{0x}^2}{2k_0^2} \sin[2\theta(s)], \tag{6.23}$$

$$\alpha_x(s) = -\sqrt{\kappa_z(s)} \left\{ \frac{k_{0x}^2}{k_0^2} \sin^2[\theta(s)] + \frac{k_{0y}^2}{k_0^2} \cos^2[\theta(s)] \right\}, \tag{6.24}$$

and

$$\alpha_y(s) = -\sqrt{\kappa_z(s)} \left\{ \frac{k_{0x}^2}{k_0^2} \cos^2[\theta(s)] + \frac{k_{0y}^2}{k_0^2} \sin^2[\theta(s)] \right\}. \tag{6.25}$$

By adding Eqs. (5.24) and (5.25), subtracting Eq. (5.24) from Eq. (5.25), and carrying out the integrations on resulting equations with the initial condition $\alpha_x(0) = \alpha_y(0) = 0$, it is readily shown that α_x and α_y in Eqs. (6.24) and (6.25) are a particular solution to Eqs. (5.24) and (5.25).

As a second step, we apply another transformation from the twisted canonical variables $(\tilde{x}, \tilde{y}, \tilde{P}_x, \tilde{P}_y)$ to canonical variables $(x_1, y_1, P_{x1}, P_{y1})$ using the generating function

$$\tilde{F}_2(\tilde{x}, \tilde{y}; P_{x1}, P_{y1}, s) = \frac{1}{2} \left[\frac{w_x'(s)}{w_x(s)} - C(s) \right] \tilde{x}^2 + \frac{1}{2} \left[\frac{w_y'(s)}{w_y(s)} + C(s) \right] \tilde{y}^2 + \frac{\tilde{x} P_{x1}}{w_x(s)} + \frac{\tilde{y} P_{y1}}{w_y(s)}, \tag{6.26}$$

where $w_x(s) = w_x(s+S)$ and $w_y(s) = w_y(s+S)$ are periodic functions solves the differential equations

$$\frac{w_x''(s)}{w_x(s)} - C'(s) - C^2(s) + \sqrt{\kappa_z(s)}\frac{k_{0y}^2 \sin^2[\theta(s)] + k_{0x}^2 \cos^2[\theta(s)]}{k_0^2} - \frac{2K}{a(s)[a(s)+b(s)]} = \frac{1}{w_x^4(s)}, \tag{6.27}$$

$$\frac{w_y''(s)}{w_y(s)} + C'(s) - C^2(s) + \sqrt{\kappa_z(s)}\frac{k_{0y}^2 \cos^2[\theta(s)] + k_{0x}^2 \sin^2[\theta(s)]}{k_0^2} - \frac{2K}{b(s)[a(s)+b(s)]} = \frac{1}{w_y^4(s)}. \tag{6.28}$$

It follows from Eq. (6.26) that

$$\tilde{P}_x = \frac{\partial \tilde{F}_2}{\partial \tilde{x}} = \left[\frac{w_x'(s)}{w_x(s)} - C(s)\right]\tilde{x} + \frac{P_{x1}}{w_x(s)}, \tag{6.29}$$

$$\tilde{P}_y = \frac{\partial \tilde{F}_2}{\partial \tilde{y}} = \left[\frac{w_y'(s)}{w_y(s)} + C(s)\right]\tilde{y} + \frac{P_{y1}}{w_y(s)}, \tag{6.30}$$

$$x_1 = \frac{\partial \tilde{F}_2}{\partial P_{x1}} = \frac{\tilde{x}}{w_x(s)}, \tag{6.31}$$

$$y_1 = \frac{\partial \tilde{F}_2}{\partial P_{y1}} = \frac{\tilde{y}}{w_y(s)}. \tag{6.32}$$

The Hamiltonian in the canonical variables $(x_1, y_1, P_{x1}, P_{y1})$ is then expressed as

$$\begin{aligned} H_{1\perp}(x_1, y_1, P_{x1}, P_{y1}, s) &= \tilde{H}_\perp(\tilde{x}, \tilde{y}, \tilde{P}_x, \tilde{P}_y, s) + \frac{\partial \tilde{F}_2}{\partial s} \\ &= \frac{1}{2}\left\{\frac{P_{x1}^2}{w_x^2(s)} + \frac{P_{y1}^2}{w_y^2(s)} + \frac{x_1^2}{w_x^2(s)} + \frac{y_1^2}{w_y^2(s)}\right\} + \frac{d\varphi(s)}{ds}(y_1 P_{x1} - x_1 P_{y1}), \end{aligned} \tag{6.33}$$

where we have introduced and demanded

$$\frac{d\varphi(s)}{ds} \equiv \frac{w_y(s)}{w_x(s)}\left\{\frac{d\theta(s)}{ds} - \alpha_x\right\} = \frac{w_x(s)}{w_y(s)}\left\{\frac{d\theta(s)}{ds} - \alpha_y\right\}. \tag{6.34}$$

Following Eq. (6.34), it can be shown that the twisted angle $\theta(s)$ has to satisfy the differential equation

$$\frac{d\theta(s)}{ds} = \frac{w_x^2(s)\alpha_y(s) - w_y^2(s)\alpha_x(s)}{w_x^2(s) - w_y^2(s)}. \tag{6.35}$$

The equations of motion described by $H_{1\perp}$ are

$$x_1' = \frac{\partial H_{1\perp}}{\partial P_{x1}} = \frac{P_{x1}}{w_x^2(s)} + \frac{d\varphi(s)}{ds} y_1, \tag{6.36}$$

$$y_1' = \frac{\partial H_{1\perp}}{\partial P_{y1}} = \frac{P_{y1}}{w_y^2(s)} - \frac{d\varphi(s)}{ds} x_1, \tag{6.37}$$

$$P_{x1}' = -\frac{\partial H_{1\perp}}{\partial x_1} = -\frac{x_1}{w_x^2(s)} + \frac{d\varphi(s)}{ds} P_{y1}, \tag{6.38}$$

$$P_{y1}' = -\frac{\partial H_{1\perp}}{\partial y_1} = -\frac{y_1}{w_y^2(s)} - \frac{d\varphi(s)}{ds} P_{x1}. \tag{6.39}$$

From Eqs. (6.36)-(6.39), it is readily shown that

$$\mathrm{E} = x_1^2 + y_1^2 + P_{x1}^2 + P_{y1}^2 \tag{6.40}$$

is an exact single-particle constant of the motion for the Hamiltonian in Eq. (6.33). In the reminder of this section, we consider the following trial choice of the Vlasov equilibrium distribution function

$$f_b(x_1, y_1, P_{x1}, P_{y1}, s) = \frac{N_b}{\pi^2 \varepsilon_T} \delta\left[x_1^2 + y_1^2 + P_{x1}^2 + P_{y1}^2 - \varepsilon_T\right], \tag{6.41}$$

where $df_b/ds = 0$, $\varepsilon_T = \text{const} > 0$ is an effective emittance, and $\delta(x)$ is the Dirac δ function. As will be shown below, the density profile of the beam described by the distribution functions f_b is consistent with the uniform density profile within an ellipse, which is the key requirement for the quantity $\mathrm{E} = x_1^2 + y_1^2 + P_{x1}^2 + P_{y1}^2$ to be a constant of motion. Therefore, the distribution function defined in Eq. (6.41) is indeed a Vlasov equilibrium, i.e.,

$$\frac{\partial f_b}{\partial s} = 0. \tag{6.42}$$

The distribution described in Eq. (6.41) has the following statistical properties. First, the distribution is consistent with the assumed density profile in Eq. (6.3)

$$\begin{aligned} n_b(\tilde{x}, \tilde{y}, s) &= \frac{1}{w_x w_y} \iint f dP_{x1} dP_{y1} \\ &= \frac{1}{w_x w_y} \int_0^\infty \frac{N_b}{\pi^2 \varepsilon_T} \delta\left[\frac{U^2}{\varepsilon_T} - \left(1 - \frac{x_1^2}{\varepsilon_T} - \frac{y_1^2}{\varepsilon_T}\right)\right] \pi d\frac{U^2}{\varepsilon_T} \\ &= \begin{cases} \dfrac{N_b}{\pi \varepsilon_T w_x w_y}, & \text{if } \dfrac{x_1^2}{\varepsilon_T} + \dfrac{y_1^2}{\varepsilon_T} \le 1, \\ 0, & \text{otherwise.} \end{cases} \end{aligned} \tag{6.43}$$

If $a = \sqrt{\varepsilon_T} w_x$ and $b = \sqrt{\varepsilon_T} w_y$ then the beam is uniform in the beam interior $\dfrac{x_1^2}{\varepsilon_T} + \dfrac{y_1^2}{\varepsilon_T} = \dfrac{\tilde{x}^2}{w_x^2 \varepsilon_T} + \dfrac{\tilde{y}^2}{w_y^2 \varepsilon_T} = \dfrac{\tilde{x}^2}{a^2} + \dfrac{\tilde{y}^2}{b^2} \le 1$; that is, the beam has the uniform-density profile given in Eq. (6.3), provided that

$$a = \sqrt{\varepsilon_T}\, w_x \tag{6.44}$$

and

$$b = \sqrt{\varepsilon_T}\, w_x \tag{6.45}$$

are satisfied. Substituting Eqs. (6.44) and (6.45) into Eqs. (6.27), (6.28) and (6.35), we obtain

$$\frac{d^2 a}{ds^2} - \left[\frac{b^2\left(\alpha_x^2 - 2\alpha_x\alpha_y\right) + a^2\alpha_y^2}{a^2 - b^2} + \sqrt{\kappa_{z0}}\,\frac{k_{0x}^2 - k_{0y}^2}{k_0}\cos(k_0 s)\sin(2\theta) - 2\sqrt{\kappa_{z0}}\,\alpha_y \sin(k_0 s) \right] a - \frac{2K}{a+b} = \frac{\varepsilon_T^2}{a^3}, \tag{6.46}$$

$$\frac{d^2 b}{ds^2} + \left[\frac{a^2\left(\alpha_y^2 - 2\alpha_x\alpha_y\right) + b^2\alpha_x^2}{a^2 - b^2} + \sqrt{\kappa_{z0}}\,\frac{k_{0x}^2 - k_{0y}^2}{k_0}\cos(k_0 s)\sin(2\theta) + 2\sqrt{\kappa_{z0}}\,\alpha_x \sin(k_0 s) \right] b - \frac{2K}{a+b} = \frac{\varepsilon_T^2}{b^3}. \tag{6.47}$$

$$\frac{d\theta}{ds} = \frac{a^2\alpha_y - b^2\alpha_x}{a^2 - b^2}. \tag{6.48}$$

Equations (6.46)-(6.48) are written in a form similar to Eqs. (5.22), (5.23) and (5.26) in the cold-fluid equilibrium theory. They are identical to Eqs. (5.22), (5.23) and (5.26) in the cold-fluid equilibrium theory, except that the thermal emittance terms appear on the right hand side of the first two equations are zero in the cold-fluid equilibrium theory. Therefore, they are more general than the cold-fluid equilibrium theory.

Second, in the normalized units, the average (macroscopic flow) transverse velocity of the beam equilibrium described by Eq. (6.41) is given in the twisted coordinates by

$$
\begin{aligned}
\tilde{\mathbf{V}}_{\perp} &= \left(\frac{N_b}{\pi\varepsilon_T w_x w_y}\right)^{-1} \frac{1}{w_x w_y} \int\left[(\tilde{x}' - \tilde{y}\theta')\mathbf{e}_{\tilde{x}} + (\tilde{y}' + \tilde{x}\theta')\mathbf{e}_{\tilde{y}}\right] f dP_{x1} dP_{y1} \\
&= \frac{\pi\varepsilon_T}{N_b} \int\left[\left(\frac{P_{x1}}{w_x} + w_x' x_1 - \alpha_x w_y y_1\right)\mathbf{e}_{\tilde{x}} + \left(\frac{P_{y1}}{w_y} + w_y' y_1 + \alpha_y w_x x_1\right)\mathbf{e}_{\tilde{y}}\right] f dP_{x1} dP_{y1} \\
&= \frac{\pi\varepsilon_T}{N_b}\left\{\int\left(\frac{P_{x1}}{w_x}\mathbf{e}_{\tilde{x}} + \frac{P_{y1}}{w_y}\mathbf{e}_{\tilde{y}}\right) f dP_{x1} dP_{y1} + \left[(w_x' x_1 - \alpha_x w_y y_1)\mathbf{e}_{\tilde{x}} + (w_y' y_1 + \alpha_y w_x x_1)\mathbf{e}_{\tilde{y}}\right]\int f dP_{x1} dP_{y1}\right\} \\
&= \left(\frac{w_x'}{w_x}\tilde{x} - \alpha_x \tilde{y}\right)\mathbf{e}_{\tilde{x}} + \left(\frac{w_y'}{w_y}\tilde{y} + \alpha_y \tilde{x}\right)\mathbf{e}_{\tilde{y}}.
\end{aligned}
\tag{6.49}
$$

The flow velocity in Eq. (6.49) is identical to the flow velocity derived by the cold-fluid theory provided that the relations

$$
\mu_x = a'/a = w_x'/w_x \tag{6.50}
$$

and

$$
\mu_y = b'/b = w_y'/w_y \tag{6.51}
$$

are satisfied.

As a third statistical property, the beam equilibrium described by Eq. (6.41) has the effective transverse temperature profile

$$
\begin{aligned}
T_{\perp}(\tilde{x}, \tilde{y}, s) &= \left(\frac{N_b}{\pi\varepsilon_T w_x w_y}\right)^{-1} \frac{1}{w_x w_y} \int\left(\tilde{\mathbf{v}}_{\perp} - \tilde{\mathbf{V}}_{\perp}\right)^2 f dP_{x1} dP_{y1} \\
&= \frac{\pi\varepsilon_T}{N_b} \int\left[\left(\tilde{x}' - \tilde{y}\theta' - \frac{w_x'}{w_x}\tilde{x} + \alpha_x \tilde{y}\right)\mathbf{e}_{\tilde{x}} + \left(\tilde{y}' + \tilde{x}\theta' - \frac{w_y'}{w_y}\tilde{y} - \alpha_y \tilde{x}\right)\mathbf{e}_{\tilde{y}}\right]^2 f dP_{x1} dP_{y1} \\
&= \frac{\pi\varepsilon_T}{N_b} \int\left[\left(\frac{P_{x1}}{w_x}\right)^2 + \left(\frac{P_{y1}}{w_y}\right)^2\right] f dP_{x1} dP_{y1}
\end{aligned}
$$

$$
\begin{aligned}
&= \frac{1}{2}\left(\frac{1}{w_x^{\,2}} + \frac{1}{w_y^{\,2}}\right)\left(1 - \frac{\tilde{x}^2}{\varepsilon_T w_x^{\,2}} - \frac{\tilde{y}^2}{\varepsilon_T w_y^{\,2}}\right) \\
&= \frac{\varepsilon_T}{2}\left(\frac{1}{a^2} + \frac{1}{b^2}\right)\left(1 - \frac{\tilde{x}^2}{a^2} - \frac{\tilde{y}^2}{b^2}\right).
\end{aligned}
\tag{6.52}
$$

As the fourth property, defining the 4 times thermal the rms emittance of the beam in the twisted frame by

$$
\varepsilon_{th} = \frac{4}{\beta_c c}\sqrt{\left\langle \tilde{x}^2 \right\rangle \left\langle \tilde{v}_x - \tilde{V}_x \right\rangle^2}\,, \tag{6.53}
$$

where

$$
\begin{aligned}
\left\langle \tilde{x}^2 \right\rangle &= \frac{\int \tilde{x}^2 f dx_1 dy_1 dP_{x1} dP_{y1}}{\int f dx_1 dy_1 dP_{x1} dP_{y1}} = \frac{1}{\pi^2 \varepsilon_T}\int x_1^{\,2} w_x^2 \delta\left[x_1^2 + y_1^2 + P_{x1}^2 + P_{y1}^2 - \varepsilon_T\right] dx_1 dy_1 dP_{x1} dP_{y1} \\
&= \frac{1}{\pi\varepsilon_T}\int w_x^2 r_1^2 \cos^2\theta_1\, \delta\left[r_1^2 + U^2 - \varepsilon_T\right] r_1 dr_1 d\theta_1 dU^2 \\
&= \frac{w_x^2}{\varepsilon_T}\frac{1}{4}\varepsilon_T^2 \\
&= \frac{1}{4}a^2,
\end{aligned}
\tag{6.54}
$$

$$
\begin{aligned}
\left\langle \tilde{v}_x^2 - \tilde{V}_x^2 \right\rangle &= \frac{\int\left(\tilde{v}_x^2 - \tilde{V}_x^2\right) f dx_1 dy_1 dP_{x1} dP_{y1}}{\int f dx_1 dy_1 dP_{x1} dP_{y1}} = \frac{\beta_b^2 c^2}{\pi^2 \varepsilon_T}\int \frac{P_{x1}^2}{w_x^2}\delta\left[x_1^2 + y_1^2 + P_{x1}^2 + P_{y1}^2 - \varepsilon_T\right] dx_1 dy_1 dP_{x1} dP_{y1} \\
&= \frac{\beta_b^2 c^2}{\pi\varepsilon_T}\int w_x^{-2} U^2 \cos^2\varphi_1\, \delta\left[r_1^2 + U^2 - \varepsilon_T\right] r_1 dr_1 d\theta_1 d\frac{U^2}{2} d\varphi_1 \\
&= \frac{\beta_b^2 c^2}{\varepsilon_T}\frac{1}{4w_x^2}\varepsilon_T^2 \\
&= \frac{\beta_b^2 c^2}{4}\frac{\varepsilon_T^2}{a^2}.
\end{aligned}
\tag{6.55}
$$

Combining Eqs. (6.52)-(6.54) yields

$$\varepsilon_{th} = \frac{4}{\beta_c C}\sqrt{\left\langle \tilde{x}^2 \right\rangle \left\langle \left(\tilde{v}_x - \tilde{V}_x\right)^2 \right\rangle} = \varepsilon_T . \tag{6.56}$$

Finally, the Vlasov elliptic beam equilibrium has two limiting cases which are well know. It recovers the familiar rigid-rotor Vlasov equilibrium [69] by setting the major-axis equal to the minor-axis of the beam ellipse. It also recovers the familiar constant-radius, uniform-density rigid-rotor Valsov equilibrium [60] by taking the limit of a uniform magnetic field with $B_z = B = \text{const.}$

6.3 Applications of the Vlasov equilibrium theory

We illustrate examples an example of periodically focused Vlasov equilibrium beams in a periodic non-axisymmetric magnetic focusing field and the temperature effects with numerical calculations. A numerical module in the PFB2D code has been developed to solve the generalized envelope equations (6.24), (6.25), (6.46)-(6.48), which determines the rotational flow velocity, the outer equilibrium major-axis $a(s)$ and minor-axis $b(s)$of the beam ellipse, and the twisted angle $\theta(s)$.

In particular, we consider a nonrelativistic elliptic beam with voltage $V_b = 2.29$ keV, current $I_b = 0.11$ A, aspect ratio $a/b = 6$, and non-axisymmetric periodic permanent magnet focusing with $B_0 = 337.5$ G, $S = 1.912$ cm, and $k_{0y}/k_{0x} = 1.6$, which is corresponding to a beam design for a high-efficiency 200 W ribbon-beam amplifier (RBA) which is being developed at Massachusetts Institute of Technology (MIT) and Beam Power Technology for wireless communication [65]. For such a system the matched solution of the generalized envelope

equations (6.24), (6.25), (6.46)-(6.48) is calculated numerically as shown in Figs. 6.1 and 6.2 for various maximum (on-axis) temperature choices with the corresponding parameters: $k_{0x} = 1.57$ cm^{-1}, $k_{0y} = 2.39$ cm^{-1}, $\sqrt{\kappa_{z0}} = 0.732$ cm^{-1}, and $K = 1.13 \times 10^{-2}$. The solutions to the generalized envelope equations (6.24), (6.25), (6.46)-(6.48), displayed as solid and dashed curves in Fig. 6.1 and 6.2, show that the semi-axes of the elliptical beam remain almost constant with small-amplitude oscillations, that the orientation of the ellipse twists periodically with an amplitude of ten degrees.

As shown in Fig. 6.1 and 6.2, the solid lines represent the beam envelopes and twisted angle with zero temperature which is corresponding to a cold beam, while the dashed lines represent the beam envelopes and twisted angles with 1 eV on-axis temperature in Fig. 6.1 and 10 eV on-axis temperature in Fig. 6.2. The aspect ratio of the beam reduces from 6 to 3.8 as the on-axis temperature of the beam increases from 0 to 10 eV, i.e., the elliptic beam becomes more circular. However, the twisted angle is almost unchanged as the on-axis temperature increases from 0 to 10 eV. For the elliptic beam designed for the 200 W ribbon-beam amplifier, the temperature of the beam is estimated to be 0.1 eV from simulations [64]. In such a case, the temperature effect is negligible.

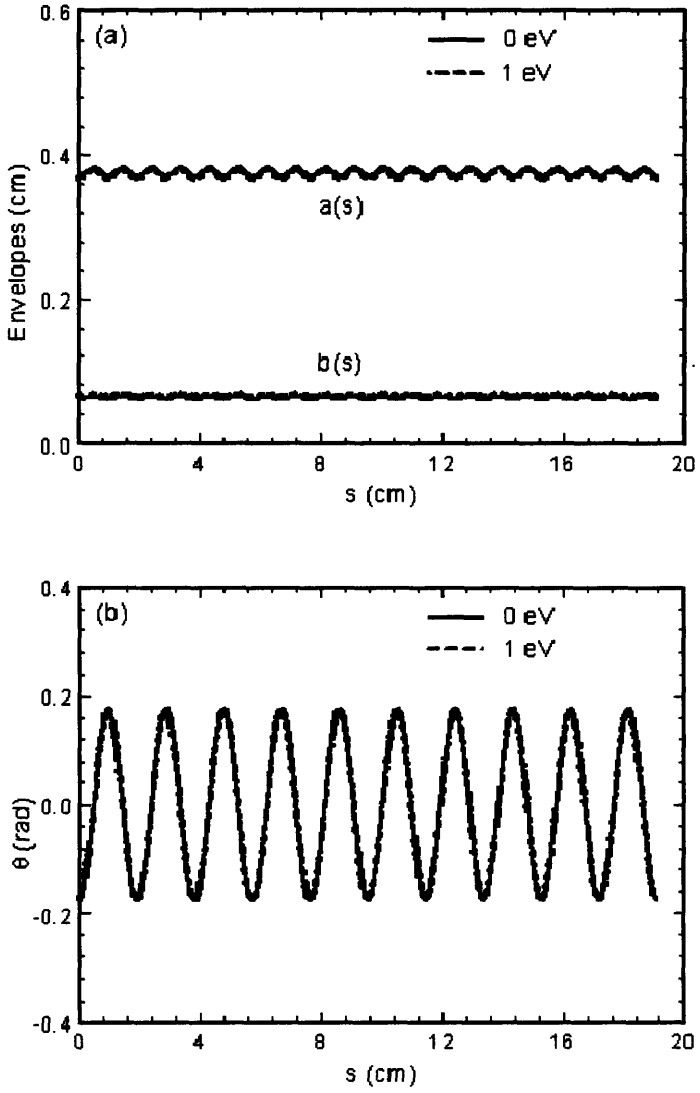

Fig. 6.1 Plots of (a) envelopes $a(s)$ and $b(s)$ and (b) twist angle $\theta(s)$ versus the axial distance s for the nonrelativistic twisted ellipse-shaped beam. The solid curves are the generalized envelope solution for a zero-temperature beam, whereas the dashed curves are for a 1 eV on-axis temperature beam.

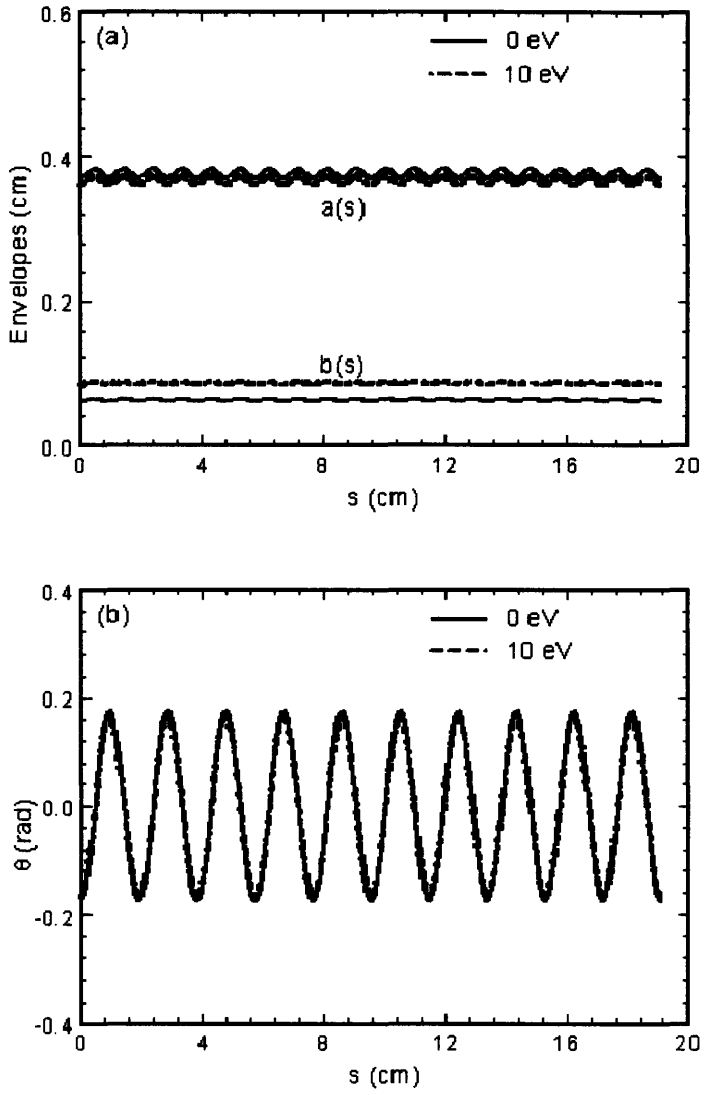

Fig. 6.2 Plots of (a) envelopes $a(s)$ and $b(s)$ and (b) twist angle $\theta(s)$ versus the axial distance s for the nonrelativistic twisted ellipse-shaped beam. The solid curves are the generalized envelope solution for a zero-temperature beam, whereas the dashed curves are for a 10 eV on-axis temperature beam.

6.4 Summary

The single-particle Hamiltonian of a periodically twisted large-aspect-ratio elliptic beam in a non-axisymmetric periodic magnetic focusing field has been investigated. A new constant of motion has been found such that the self-consistent beam equilibrium can be constructed as a function of the constant of motion. The beam envelope equations and flow velocity equations have been derived. They are consistent with the generalized envelope equations derived from the cold-fluid equilibrium theory [65] when the temperature is taken to be zero. Statistical properties of the present Vlasov elliptic beam equilibrium have been studied. For current applications of interest, the temperature effects have been found to be small on periodically twisted large-aspect-ratio elliptic beams.

Chapter 7

Conclusion and Future Directions

7.1 Conclusion

In this thesis, we focus on the transport theory of high-intensity elliptic charged-particle beams. In particular, the halo formation and beam loss problem associated with the high space charge and small-aperture structure is addressed. A novel transport theory of large-aspect-ratio elliptic beams has been developed.

To understand the halo formation and beam loss of high-intensity elliptic charged-particle beams in small-aperture systems, beam envelope studies, test-particle studies and self-consistent PIC simulations have been carried out. First of all, the rms envelope equations have been derived and analyzed for unbunched intense charged-particle beams in an alternating-gradient focusing field and a cylindrical metal pipe. All higher-order image-charge effects from the cylindrical conducting pipe have been expressed in terms of so-called multiple moment factors in the rms beam envelope equations, and the multiple momentum factors were evaluated. Numerical results have shown that for vacuum phase advance $\sigma_v < 90$, the higher-order image-charge effects on the matched and slightly mismatched beam envelopes are negligibly small for all beams with arbitrary beam density profiles (including hollow density profiles) as well as for arbitrary small apertures (including beams with large aspect ratios). However, the main unstable region for the envelope evolution with image-charge effects, which occurs for $90 < \sigma_v < 270$, depending on the value of the normalized beam intensity SK/ε , has been found to be narrower than its counterpart without image-charge effects.

Secondly, it has been shown that using the test-particle model in a small-aperture alternating-gradient focusing channel, image-charge effects induce a new mechanism for chaotic particle motions and halo formation in intense charge-particle beams. This mechanism occurs for well-matched beams with the ideal Kapchinskij-Vladimirskij (KV) distribution. The halo formation and beam loss are sensitive to system parameters: the quadruple focusing field filling factor, the vacuum phase advance, the perveance and the pipe radius. As shown in our parametric studies, the beam loss increases rapidly as the perveance of the beam increases and as the pipe radius decreases. This demonstrates that in the current configuration, the halo formation and beam loss is intrinsic due to the nonlinear space-charge forces in high-intensity charged-particle beams focused by the alternating-gradient focusing fields in small-aperture systems.

Thirdly, a self-consistent PIC simulation code, Periodically Focused Beam (PFB2D), has been developed. The algorithms used in the code have been discussed. Such a code has been used to simulate intense charged-particle beams in small-aperture alternating-gradient systems which have been investigated theoretically. PIC simulation results on the beam envelope are consistent with the envelope equation solutions, and PIC simulation results on the halo formation are consistent with the test-particle results. However, due to numerical noise in PIC simulations, the beam loss predicted by PIC simulation has been found to be an order of magnitude higher than that predicted by theory, which led to the an analysis of noise in PIC simulations. An error scaling law for the edge emittance growth and particle diffusion due to the discrete macro-particle effects has been derived for self-consistent intense beam simulations. The scaling law has been valid for both the periodic solenoidal magnetic focusing channel and the periodic quadrupole magnetic focusing channel. In addition, the error scaling law has been tested in the

self-consistent Green's function simulations and self-consistent PIC PFB2D simulations. The simulation results have shown good agreement with the scaling law.

Finally, novel exact paraxial cold-fluid and Vlasov equilibria have been found for a high-intensity, space-charge-dominated charged-particle beam with a periodically twisted elliptic cross section in a non-axisymmetric periodic magnetic field. Generalized envelope equations, which determine the beam envelopes, ellipse orientation, density, and internal flow velocity profiles, have been derived, and solved numerically for nonrelativistic and relativistic examples of such beams. The equilibrium and stability of such beams have been demonstrated by self-consistent particle-in-cell (PIC) simulations. For current applications, the temperature effects are found to be small on a periodically twisted large-aspect-ratio elliptic beam. We anticipate that the equilibrium theory will provide a valuable tool in the design of high-intensity elliptic beams in novel vacuum electron devices, especially for ribbon-beam klystrons (RBKs) and ribbon-beam traveling-wave amplifiers (RBA). The ellipse-shaped beam equilibria may provide some flexibility in the design and operation of high-intensity accelerators.

7.2 Future Directions

Solid ground on the understanding of the space charge effects of high-intensity elliptic charged-particle beams in small-aperture systems has been gained. However, most of the theoretical models are based on 2-dimensional continuous dc beams and the ideal KV beam distribution. In order to represent a practical situation, 3-D theoretical models have to be developed and more realistic beam distribution, for example, a thermal equilibrium distribution, is desirable. Therefore, toward to the goal of achieving realistic models and simulations of the intense beams, the following problems have to be addressed in the future.

- *Thermal equilibrium theory.* The state of art of equilibrium theory in intense elliptic charged-particle beams are based the assumption of the KV distribution. In such a distribution, all the particles have the same single energy which is artificial and does not represent a realistic situation. Statistically, a many-body system is most likely to relax to a thermal equilibrium which can be described by a Maxwellian distribution. The only known thermal equilibrium of intense beams is a constant-radius uniform-density rigid-rotor beam [74] in a uniform applied magnetic field. Recently, the author is investigating in thermal equilibrium theory of a periodically focused rigid-rotor beam with breathing envelopes [75]. Furthermore, it is desirable to have a thermal equilibrium of intense elliptic beams for applications of heavy-ion beams.
- *3D effects of bunched beams.* The current theoretical models assume the beam is infinite long in the longitudinal direction. Therefore, the 3D effects from a finite-length bunched beam are ignored. However, in reality the beams have finite lengths. In some applications the beams are bunched to very short lengths. Therefore, it is required to understand the physics and space charge effects in the 3D configuration for those applications. The self-electric and self-magnetic field calculations for 3D cigar-like beams or ellipsoid beams are no longer trivial. A future step is to consider a spherical beam whose self-electric and self-magnetic fields are easier to calculate. The rigorous theoretical analysis of the space charge effects and halo formation are required on 3D bunched beams.

Appendix A

Solution of 2D Poisson Equation with a Cylindrical Boundary

A.1 Solutions to Poisson equation in free space

A.1.1 Solutions to 3D Poisson equation in free space

The three-dimensional Poisson equation in free space is expressed as

$$\nabla^2\phi = -4\pi qn \text{ and } \phi|_{\infty} = 0, \tag{A.1}$$

where ϕ is the potential, q is the particle charge, and n is the number density in the self-similar beam model, which can be expressed as

$$n = n(\frac{x^2}{a^2}+\frac{y^2}{b^2}+\frac{z^2}{c^2}). \tag{A.2}$$

In order to solve Eq. (A.1), we first find the Green function of $G = G(\mathbf{x},\mathbf{x}')$ for this problem. Here, $\mathbf{x} = (x, y, z)$ and $\mathbf{x}' = (x', y', z')$. The Green function G satisfies

$$\nabla^2 G = -4\pi\delta(\mathbf{x}-\mathbf{x}') \text{ and } G|_{\infty} = 0, \tag{A.3}$$

The solution of G is well known, and is expressed as

$$G(\mathbf{x},\mathbf{x}') = \frac{1}{|\mathbf{x}-\mathbf{x}'|} = \frac{1}{2\pi^2}\int_{-\infty}^{\infty}\int_{-\infty}^{\infty}\int_{-\infty}^{\infty}\frac{\exp[i\mathbf{k}\cdot(\mathbf{x}-\mathbf{x}')]}{k^2}d\mathbf{k}. \tag{A.4}$$

Therefore, the solution of potential is written as

$$\phi(\mathbf{x}) = q\int_{V'} n(\mathbf{x}')G(\mathbf{x},\mathbf{x}')d\mathbf{x}' = \frac{q}{2\pi^2}\int n(\mathbf{x}')\frac{\exp[i\mathbf{k}\cdot(\mathbf{x}-\mathbf{x}')]}{k^2}d\mathbf{x}'d\mathbf{k}$$

$$= \frac{q}{2\pi^2} \int \frac{\exp(i\mathbf{k}\cdot\mathbf{x})}{k^2} d\mathbf{k} \int n(\mathbf{x}) \exp(-i\mathbf{k}\cdot\mathbf{x}) d\mathbf{x}'. \tag{A.5}$$

Using $\hat{x} = \frac{x'}{a}$, $\hat{y} = \frac{y'}{b}$, and $\hat{z} = \frac{z'}{c}$, we obtain

$$I_1 = \int n(\mathbf{x}') \exp(-i\mathbf{k}\cdot\mathbf{x}') d\mathbf{x}'$$

$$= \int n\left(\frac{x'^2}{a^2} + \frac{y'^2}{b^2} + \frac{z'^2}{c^2}\right) \exp(-i\mathbf{k}\cdot\mathbf{x}') d\mathbf{x}'$$

$$= abc \int n(\hat{x}^2 + \hat{y}^2 + \hat{z}^2) \exp(-i\mathbf{k}'\cdot\hat{\mathbf{x}}) d\hat{\mathbf{x}}, \tag{A.6}$$

where, $\hat{\mathbf{x}} = (\hat{x}, \hat{y}, \hat{z})$ and $\mathbf{k}' = (k_x a, k_y b, k_z c)$. The expression (A.6) can be simplified to

$$I_1 = I_1(k') = 4\pi abc \int_0^\infty n(\hat{r}^2)\, \hat{r}^2 \frac{\sin(k'\hat{r})}{k'\hat{r}} d\hat{r}, \tag{A.7}$$

where $\hat{r}^2 = \hat{x}^2 + \hat{y}^2 + \hat{z}^2$.

Using Eqs. (A.6) and (A.7) in Eq. (A.5), we obtain

$$\phi(\mathbf{x}) = \frac{q}{2\pi^2} \int \frac{\exp(i\mathbf{k}\cdot\mathbf{x})}{k^2} d\mathbf{k} \int n(\mathbf{x}') \exp(-i\mathbf{k}\cdot\mathbf{x}') d\mathbf{x}'$$

$$= \frac{q}{2\pi^2} \int \frac{\exp(i\mathbf{k}\cdot\mathbf{x})}{k^2} d\mathbf{k}\, 4\pi abc \int_0^\infty n(r^2)\, r^2 \frac{\sin(k'r)}{k'r} dr$$

$$= \frac{2q}{\pi} \int \frac{\exp\left[i\left(\frac{k'_x x}{a} + \frac{k'_y y}{b} + \frac{k'_z z}{c}\right)\right]}{\left(\frac{k'_x}{a}\right)^2 + \left(\frac{k'_y}{b}\right)^2 + \left(\frac{k'_z}{c}\right)^2} d\mathbf{k}' \int_0^\infty n(r^2)\, r^2 \frac{\sin(k'r)}{k'r} dr$$

$$= \frac{2q}{\pi} \int_0^\infty \int_0^\pi \int_0^{2\pi} \frac{\cos\left[k'\left(a^{-1} x \sin\theta\cos\varphi + b^{-1} y \sin\theta\sin\varphi + c^{-1} z\cos\theta\right)\right]}{\left[\left(a^{-1}\sin\theta\cos\varphi\right)^2 + \left(b^{-1}\sin\theta\sin\varphi\right)^2 + \left(c^{-1}\cos\theta\right)^2\right] k'^2} k'^2 \sin\theta\, dk'\, d\theta\, d\varphi \times$$

$$\int_0^{\infty} n\left(\hat{r}^2\right)\hat{r}^2\frac{\sin\left(k'\hat{r}\right)}{k'\hat{r}}d\hat{r}\,, \tag{A.8}$$

where

$$k_x' = k'\sin\theta\cos\varphi\,,\ k_y' = k'\sin\theta\sin\varphi\,,\text{ and }\ k_y' = k'\cos\theta\,. \tag{A.9}$$

It is readily shown from Eq. (A.8) that the potential ϕ satisfies

$$\phi(x,y,z)=\phi(-x,y,z)=\phi(x,-y,z)=\phi(x,y,-z). \tag{A.10}$$

From table of integrals [77], we obtain

$$\int_0^{\pi}\int_0^{2\pi}\frac{\sin\theta d\theta d\varphi}{\left(a^{-1}\sin\theta\cos\varphi\right)^2+\left(b^{-1}\sin\theta\sin\varphi\right)^2+\left(c^{-1}\cos\theta\right)^2}$$

$$=2\pi\int_0^{\pi}\frac{\sin\theta d\theta}{\sqrt{\left(a^{-2}\sin^2\theta+c^{-2}\cos^2\theta\right)\left(b^{-2}\sin^2\theta+c^{-2}\cos^2\theta\right)}}$$

$$=2\pi abc\int_0^{\infty}\frac{ds}{\sqrt{\left(a^2+s\right)\left(b^2+s\right)\left(c^2+s\right)}}. \tag{A.11}$$

Now, we return to Eq. (A.8), and note that

$$I_2=\int_0^{\pi}\int_0^{2\pi}\frac{\cos\left[k'\left(a^{-1}x\sin\theta\cos\varphi+b^{-1}y\sin\theta\sin\varphi+c^{-1}z\cos\theta\right)\right]}{\left[\left(a^{-1}\sin\theta\cos\varphi\right)^2+\left(b^{-1}\sin\theta\sin\varphi\right)^2+\left(c^{-1}\cos\theta\right)^2\right]}\sin\theta d\theta d\varphi$$

$$=\int_0^{\pi}\int_0^{2\pi}\frac{\sum_{n=0}^{\infty}\frac{(-)^n}{(2n)!}\left[k'\left(a^{-1}x\sin\theta\cos\varphi+b^{-1}y\sin\theta\sin\varphi+c^{-1}z\cos\theta\right)\right]^{2n}}{\left[\left(a^{-1}\sin\theta\cos\varphi\right)^2+\left(b^{-1}\sin\theta\sin\varphi\right)^2+\left(c^{-1}\cos\theta\right)^2\right]}\sin\theta d\theta d\varphi. \tag{A.12}$$

Using Eq. (A.10), we obtain

$$I_2 = \int_0^{\pi}\int_0^{2\pi} \frac{\sum_{n=0}^{\infty}\frac{(-)^n k'^{2n}}{(2n)!}\sum_{\substack{\hat{p},\hat{q},\hat{r}=0\\ \hat{p}+\hat{q}+\hat{r}=2n}}^{2n}\frac{(2n)!}{\hat{p}!\hat{q}!\hat{r}!}\left(a^{-1}x\sin\theta\cos\varphi\right)^{\hat{p}}\left(b^{-1}y\sin\theta\sin\varphi\right)^{\hat{q}}\left(c^{-1}z\cos\theta\right)^{\hat{r}}}{\left(a^{-1}\sin\theta\cos\varphi\right)^2+\left(b^{-1}\sin\theta\sin\varphi\right)^2+\left(c^{-1}\cos\theta\right)^2}\sin\theta d\theta d\varphi$$

$$= \int_0^{\pi}\int_0^{2\pi} \frac{\sum_{n=0}^{\infty}\frac{(-)^n k'^{2n}}{(2n)!}\sum_{\substack{p,q,r=0\\ p+q+r=n}}^{n}\frac{(2n)!}{(2p)!(2q)!(2r)!}\left(a^{-1}x\sin\theta\cos\varphi\right)^{2p}\left(b^{-1}y\sin\theta\sin\varphi\right)^{2q}\left(c^{-1}z\cos\theta\right)^{2r}}{a^{-2}\sin^2\theta\cos^2\varphi+b^{-2}\sin^2\theta\sin^2\varphi+c^{-2}\cos^2\theta}\sin\theta d\theta d\varphi \tag{A.13}$$

The issue is to work out the integral of

$$I(p,q,r)=\int_0^{\pi}\int_0^{2\pi}\frac{\left(a^{-1}\sin\theta\cos\varphi\right)^{2p}\left(b^{-1}\sin\theta\sin\varphi\right)^{2q}\left(c^{-1}\cos\theta\right)^{2r}}{a^{-2}\sin^2\theta\cos^2\varphi+b^{-2}\sin^2\theta\sin^2\varphi+c^{-2}\cos^2\theta}\sin\theta d\theta d\varphi . \tag{A.14}$$

To evaluate the integral in Eq. (A.14), we note that

$$I(p,q,r)=\int_0^{\infty}\delta(k-1)dk\int_0^{\pi}\int_0^{2\pi}\frac{\left(a^{-1}k\sin\theta\cos\varphi\right)^{2p}\left(b^{-1}k\sin\theta\sin\varphi\right)^{2q}\left(c^{-1}k\cos\theta\right)^{2r}}{\left(a^{-2}\sin^2\theta\cos^2\varphi+b^{-2}\sin^2\theta\sin^2\varphi+c^{-2}\cos^2\theta\right)k^2}k^2\sin\theta d\theta d\varphi$$

$$=\int_0^{\infty}\int_0^{\pi}\int_0^{2\pi}\frac{\left(a^{-1}k\sin\theta\cos\varphi\right)^{2p}\left(b^{-1}k\sin\theta\sin\varphi\right)^{2q}\left(c^{-1}k\cos\theta\right)^{2r}}{\left(a^{-2}\sin^2\theta\cos^2\varphi+b^{-2}\sin^2\theta\sin^2\varphi+c^{-2}\cos^2\theta\right)k^2}k^2\delta(k-1)\sin\theta dk d\theta d\varphi$$

$$=\int_{-\infty}^{\infty}\int_{-\infty}^{\infty}\int_{-\infty}^{\infty}\frac{\left(a^{-1}k_x\right)^{2p}\left(b^{-1}k_y\right)^{2q}\left(c^{-1}k_z\right)^{2r}}{a^{-2}k_x^2+b^{-2}k_y^2+c^{-2}k_z^2}\delta\left(\sqrt{k_x^2+k_y^2+k_z^2}-1\right)dk_x dk_y dk_z$$

$$=abc\int_{-\infty}^{\infty}\int_{-\infty}^{\infty}\int_{-\infty}^{\infty}\frac{\left(\hat{k}_x\right)^{2p}\left(\hat{k}_y\right)^{2q}\left(\hat{k}_z\right)^{2r}}{\hat{k}_x^2+\hat{k}_y^2+\hat{k}_z^2}\delta\left(\sqrt{a^2\hat{k}_x^2+b^2\hat{k}_y^2+c^2\hat{k}_z^2}-1\right)d\hat{k}_x d\hat{k}_y d\hat{k}_z$$

$$=abc\int_0^{\infty}\delta\left(\hat{k}\sqrt{a^2\sin^2\theta\cos^2\varphi+b^2\sin^2\theta\sin^2\varphi+c^2\cos^2\theta}-1\right)d\hat{k}\times$$

$$\int_0^{\pi}\int_0^{2\pi}\left(\hat{k}\sin\theta\cos\varphi\right)^{2p}\left(\hat{k}\sin\theta\sin\varphi\right)^{2q}\left(\hat{k}\cos\theta\right)^{2r}\sin\theta d\theta d\varphi$$

$$= abc \int_0^{\pi} \int_0^{2\pi} \frac{(\sin\theta\cos\varphi)^{2p}(\sin\theta\sin\varphi)^{2q}(\cos\theta)^{2r}}{\left(a^2\sin^2\theta\cos^2\varphi + b^2\sin^2\theta\sin^2\varphi + c^2\cos^2\theta\right)^{p+q+r+\frac{1}{2}}} \sin\theta d\theta d\varphi . \tag{A.15}$$

It is also readily shown from Eq. (A.15) that

$$\frac{I(p,q,r)}{abc} = \frac{(-)^{p+q+r}\Gamma\left(\frac{1}{2}\right)}{\Gamma\left(p+q+r+\frac{1}{2}\right)} \frac{\partial^{(p+q+r)}}{\partial(a^2)^p \partial(b^2)^q \partial(c^2)^r}\left[\frac{I(0,0,0)}{abc}\right] \tag{A.16}$$

where

$$I(0,0,0) = abc \int_0^{\pi} \int_0^{2\pi} \frac{\sin\theta d\theta d\varphi}{\left(a^2\sin^2\theta\cos^2\varphi + b^2\sin^2\theta\sin^2\varphi + c^2\cos^2\theta\right)^{\frac{1}{2}}} . \tag{A.17}$$

From Eqs. (A.11), (A.14), and (A.17), we obtain

$$\frac{I(0,0,0)}{abc} = 2\pi \int_0^{\infty} \frac{ds}{\sqrt{(a^2+s)(b^2+s)(c^2+s)}} \tag{A.18}$$

and

$$\frac{\partial^{(p+q+r)}}{\partial(a^2)^p \partial(b^2)^q \partial(c^2)^r}\left[\frac{I(0,0,0)}{abc}\right] = 2\pi \frac{(-)^{p+q+r}\Gamma\left(p+\frac{1}{2}\right)\Gamma\left(q+\frac{1}{2}\right)\Gamma\left(r+\frac{1}{2}\right)}{\Gamma\left(\frac{1}{2}\right)\Gamma\left(\frac{1}{2}\right)\Gamma\left(\frac{1}{2}\right)} \times$$

$$\int_0^{\infty} \frac{\left(\frac{1}{a^2+s}\right)^p \left(\frac{1}{b^2+s}\right)^q \left(\frac{1}{c^2+s}\right)^r ds}{\sqrt{(a^2+s)(b^2+s)(c^2+s)}} . \tag{A.19}$$

Equations (A.16) and (A.19) result in

$$I(p,q,r) = \frac{2\pi abc(2p)!(2q)!(2r)!n!}{(2n)!\,p!\,q!\,r!} \int_0^{\infty} \frac{\left(\frac{1}{a^2+s}\right)^p \left(\frac{1}{b^2+s}\right)^q \left(\frac{1}{c^2+s}\right)^r ds}{\sqrt{(a^2+s)(b^2+s)(c^2+s)}} . \tag{A.20}$$

Substituting Eq. (A.20) into Eq. (A.13), we obtain

$$I_2 = \int_0^{\pi}\int_0^{2\pi} \frac{\cos\left[k'\left(a^{-1}x\sin\theta\cos\varphi + b^{-1}y\sin\theta\sin\varphi + c^{-1}z\cos\theta\right)\right]}{\left(a^{-1}\sin\theta\cos\varphi\right)^2 + \left(b^{-1}\sin\theta\sin\varphi\right)^2 + \left(c^{-1}\cos\theta\right)^2}\sin\theta d\theta d\varphi$$

$$= 2\pi abc\int_0^{\pi}\int_0^{2\pi} \frac{\displaystyle\sum_{n=0}^{\infty}\frac{(-)^n k'^{2n}}{(2n)!}\sum_{\substack{p,q,r=0\\ p+q+r=n}}^{n}\frac{n!}{p!q!r!}\left(\frac{x^2}{a^2+s}\right)^p\left(\frac{y^2}{b^2+s}\right)^q\left(\frac{z^2}{c^2+s}\right)^r}{\sqrt{\left(a^2+s\right)\left(b^2+s\right)\left(c^2+s\right)}}ds$$

$$= 2\pi abc\int_0^{\pi}\int_0^{2\pi} \frac{\displaystyle\sum_{n=0}^{\infty}\frac{(-)^n k'^{2n}}{(2n)!}\left(\frac{x^2}{a^2+s}+\frac{y^2}{b^2+s}+\frac{z^2}{c^2+s}\right)^n}{\sqrt{\left(a^2+s\right)\left(b^2+s\right)\left(c^2+s\right)}}ds$$

$$= 2\pi abc\int_0^{\pi}\int_0^{2\pi} \frac{\displaystyle\sum_{n=0}^{\infty}\frac{(-)^n k'^{2n}}{(2n)!}\left(\sqrt{\frac{x^2}{a^2+s}+\frac{y^2}{b^2+s}+\frac{z^2}{c^2+s}}\right)^{2n}}{\sqrt{\left(a^2+s\right)\left(b^2+s\right)\left(c^2+s\right)}}ds$$

$$= 2\pi abc\int_0^{\infty} \frac{\cos\left[k'\left(\sqrt{\frac{x^2}{a^2+s}+\frac{y^2}{b^2+s}+\frac{z^2}{c^2+s}}\right)\right]ds}{\sqrt{\left(a^2+s\right)\left(b^2+s\right)\left(c^2+s\right)}}. \qquad \text{(A.21)}$$

Substituting Eq. (A.21) into Eq. (A.8) yields

$$\phi(\mathbf{x}) = 4qabc\int_0^{\infty}dk'\int_0^{\infty} \frac{\cos\left[k'\left(\sqrt{\frac{x^2}{a^2+s}+\frac{y^2}{b^2+s}+\frac{z^2}{c^2+s}}\right)\right]ds}{\sqrt{\left(a^2+s\right)\left(b^2+s\right)\left(c^2+s\right)}}\int_0^{\infty}n\left(\hat{r}^2\right)\hat{r}^2\frac{\sin\left(k'\hat{r}\right)}{k'\hat{r}}d\hat{r}$$

$$= 4qabc\int_0^{\infty}\frac{ds}{\sqrt{\left(a^2+s\right)\left(b^2+s\right)\left(c^2+s\right)}}\int_0^{\infty}n\left(\hat{r}^2\right)\hat{r}d\hat{r}\int_0^{\infty}\frac{\sin\left(k'\hat{r}\right)\cos\left[k'\left(\sqrt{\frac{x^2}{a^2+s}+\frac{y^2}{b^2+s}+\frac{z^2}{c^2+s}}\right)\right]}{k'}dk'$$

$$= \pi qabc\int_0^{\infty}\frac{ds}{\sqrt{\left(a^2+s\right)\left(b^2+s\right)\left(c^2+s\right)}}\int_T n(T')\,dT', \qquad \text{(A.22)}$$

where

where

$$T = \frac{x^2}{a^2+s} + \frac{y^2}{b^2+s} + \frac{z^2}{c^2+s} \tag{A.23}$$

and the identity

$$\int_0^\infty \frac{\sin(ax)\cos(bx)}{x} dx = \begin{cases} \pi/2, & 0 < b < a \\ 0, & 0 < a < b \\ \pi/4, & 0 < a = b \end{cases} \tag{A.24}$$

has been employed.

We observe from Eq. (A.22) that the potential ϕ is a finite non-zero constant at $(x, y, z) = (0,0,0)$ and becomes zero at $(x, y, z) = \infty$. However, we may choose an alternative form of the Green function differing from Eq. (A.4). The alternative Green's function is expressed as

$$G(\mathbf{x}, \mathbf{x}') = \frac{1}{|\mathbf{x} - \mathbf{x}'|} - \frac{1}{|\mathbf{x}'|} = \frac{1}{2\pi^2} \int_{-\infty}^{\infty}\int_{-\infty}^{\infty}\int_{-\infty}^{\infty} \left\{ \frac{\exp[i\mathbf{k}\cdot(\mathbf{x}-\mathbf{x}')]}{k^2} - \frac{\exp[-i\mathbf{k}\cdot\mathbf{x}']}{k^2} \right\} d\mathbf{k}, \tag{A.25}$$

and satisfies $G|_{\mathbf{x}=0} = 0$. In this case, Eq. (A.5) still holds, which can be expressed as

$$\phi(\mathbf{x}) = q \int_{V'} n(\mathbf{x}') G(\mathbf{x}, \mathbf{x}') d\mathbf{x}', \tag{A.26}$$

because of $\nabla\phi|_\infty = 0$ and $\nabla G|_\infty = 0$. Note that the Green function given by Eq. (A.25) is not symmetrical about $\mathbf{x}$ and $\mathbf{x}'$, but can be a useful solution to the problem. Using Eqs. (A.25) and (A.26), We follow a similar procedure mentioned above and obtain another solution for the potential, which can be expressed as

$$\phi(\mathbf{x}) = -\pi q a b c \int_0^{\infty} \frac{ds}{\sqrt{(a^2+s)(b^2+s)(c^2+s)}} \int_0^{T} n(T')\, dT', \tag{A.27}$$

where

$$T = \frac{x^2}{a^2+s} + \frac{y^2}{b^2+s} + \frac{z^2}{c^2+s}. \tag{A.28}$$

In this case, Eq. (A.27) indicates that $\phi = 0$ at $(x, y, z) = (0,0,0)$ and $\phi =$ finite constant at $(x, y, z) = \infty$ if the beam density satisfies $\int_0^{\infty} n(T')\, dT' =$ finite constant. This is always true physically. The solutions in Eqs. (A.22) and (A.27) may be applicable for different calculation purposes according to actual models.

A.1.2 Solutions to 2D Poisson equation in free space

The two-dimensional Poisson equation in free space is expressed as

$$\frac{\partial^2 \phi}{\partial x^2} + \frac{\partial^2 \phi}{\partial y^2} = -4\pi q n \text{ and } \nabla \phi|_{\infty} = 0, \tag{A.29}$$

where ϕ is the potential, q is the particle charge, and n is the number density in the self-similar beam model, which can be expressed as

$$n = n\left(\frac{x^2}{a^2} + \frac{y^2}{b^2}\right). \tag{A.30}$$

In order to solve Eq. (A.29), we need to find the Green function of $G = G(\mathbf{x}, \mathbf{x}')$ for this problem. Here, $\mathbf{x} = (x, y)$ and $\mathbf{x}' = (x', y')$. The Green function G satisfies

$$\frac{\partial^2 G}{\partial x^2}+\frac{\partial^2 G}{\partial y^2}=-4\pi\delta(x-x')\delta(y-y'),\ \text{and}\ \nabla G\big|_{\infty}=0. \tag{A.31}$$

In order to avoid the infinite constant problem at $\mathbf{x}=(x,y)=0$, one special solution of G should satisfy $G\big|_{\mathbf{x}=0}=0$, and is expressed as

$$G(\mathbf{x},\mathbf{x}')=\frac{1}{\pi}\int_{-\infty}^{\infty}\int_{-\infty}^{\infty}\frac{\exp[i\mathbf{k}\cdot(\mathbf{x}-\mathbf{x}')]-\exp(-\mathbf{k}\cdot\mathbf{x}')}{k^2}d\mathbf{k}$$

$$=\frac{1}{\pi}\int_{-\infty}^{\infty}\int_{-\infty}^{\infty}\frac{\exp[ik_x(x-x')+ik_y(y-y')]-\exp(-ik_x x'-ik_y y')}{k_x^2+k_y^2}dk_x dk_y$$

$$=\int_{-\infty}^{\infty}\delta(k_z)dk_z\frac{1}{\pi}\int_{-\infty}^{\infty}\int_{-\infty}^{\infty}\frac{\exp[ik_x(x-x')+ik_y(y-y')]-\exp(-ik_x x'-ik_y y')}{k_x^2+k_y^2+k_z^2}dk_x dk_y$$

$$=\int_{-\infty}^{\infty}\left\{\frac{1}{2\pi}\int_{-\infty}^{\infty}\exp[ik_z(z-z')]d(z-z')\right\}dk_z\frac{1}{\pi}\int_{-\infty}^{\infty}\int_{-\infty}^{\infty}\frac{\exp[ik_x(x-x')+ik_y(y-y')]}{k_x^2+k_y^2+k_z^2}dk_x dk_y$$

$$-\int_{-\infty}^{\infty}\left\{\frac{1}{2\pi}\int_{-\infty}^{\infty}\exp[-ik_z z']dz'\right\}dk_z\frac{1}{\pi}\int_{-\infty}^{\infty}\int_{-\infty}^{\infty}\frac{\exp[-ik_x x'-ik_y y']}{k_x^2+k_y^2+k_z^2}dk_x dk_y$$

$$=\int_{-\infty}^{\infty}d(z-z')\left\{\frac{1}{2\pi^2}\int_{-\infty}^{\infty}\int_{-\infty}^{\infty}\int_{-\infty}^{\infty}\frac{\exp[ik_x(x-x')+ik_y(y-y')+ik_z(z-z')]}{k_x^2+k_y^2+k_z^2}dk_x dk_y dk_z\right\}$$

$$-\int_{-\infty}^{\infty}dz'\left\{\frac{1}{2\pi^2}\int_{-\infty}^{\infty}\int_{-\infty}^{\infty}\int_{-\infty}^{\infty}\frac{\exp[-ik_x x'-ik_y y'-ik_z z']}{k_x^2+k_y^2+k_z^2}dk_x dk_y dk_z\right\}$$

$$=-\ln\left[\frac{(\vec{x}-\vec{x}')^2}{\vec{x}'^2}\right]=-\ln\left(r^2+r'^2-2rr'\cos(\varphi-\varphi')\right)+\ln r'^2. \tag{A.32}$$

The Green function given by Eq. (A.32) is also not symmetrical about $\mathbf{x}$ and $\mathbf{x}'$, but avoids the infinity constant problem. In order to drive the solution of potential, we use the three-dimensional results in Sec. A.1.1. We find the relationship between the two kinds of solutions using the properties of the Delta function. The solution of potential is written as

$$\phi(\mathbf{x}) = q\int_{S'} n(\mathbf{x}')G(\mathbf{x},\mathbf{x}')d\mathbf{x}' = \frac{q}{\pi}\int n(\mathbf{x}')\frac{\exp[i\mathbf{k}\cdot(\mathbf{x}-\mathbf{x}')]-\exp(-\mathbf{k}\cdot\mathbf{x}')}{k^2}d\mathbf{x}'d\mathbf{k}$$

$$= \frac{q}{\pi}\int n\left(\frac{x'^2}{a^2}+\frac{y'^2}{b^2}\right)\left[\frac{1}{\pi}\int_{-\infty}^{\infty}\int_{-\infty}^{\infty}\frac{\exp[ik_x(x-x')+ik_y(y-y')]-\exp(-ik_x x'-ik_y y')}{k_x^2+k_y^2}\right]dx'dy'dk_x dk_y$$

$$= \frac{q}{\pi}\int_{-\infty}^{\infty}\delta(z')dz'\int n\left(\frac{x'^2}{a^2}+\frac{y'^2}{b^2}+\frac{z'^2}{c^2}\right)\times$$

$$\left[\frac{1}{\pi}\int_{-\infty}^{\infty}\int_{-\infty}^{\infty}\frac{\exp[ik_x(x-x')+ik_y(y-y')]-\exp(-ik_x x'-ik_y y')}{k_x^2+k_y^2}\right]dx'dy'dk_x dk_y$$

$$= \frac{q}{\pi}\int_{-\infty}^{\infty}\left[\frac{1}{2\pi}\int_{-\infty}^{\infty}\exp(-ik_z z')dk_z\right]dz'\int n\left(\frac{x'^2}{a^2}+\frac{y'^2}{b^2}+\frac{z'^2}{c^2}\right)\frac{e^{[ik_x(x-x')+ik_y(y-y')]}-e^{(-ik_x x'-ik_y y')}}{k_x^2+k_y^2}dx'dy'dk_x dk_y$$

$$= \frac{q}{2\pi^2}\int n\left(\frac{x'^2}{a^2}+\frac{y'^2}{b^2}+\frac{z'^2}{c^2}\right)\exp[-i(k_x x'+k_y y'+k_z z')]\frac{\exp[i(k_x x+k_y y)]-1}{k_x^2+k_y^2}dx'dy'dz'dk_x dk_y dk_z$$

$$= \frac{q}{2\pi^2}\int\frac{\exp\left[i\left(\frac{\hat{k}_x x}{a}+\frac{\hat{k}_y y}{b}\right)\right]-1}{\frac{\hat{k}_x^2}{a^2}+\frac{\hat{k}_y^2}{b^2}}d\hat{k}_x d\hat{k}_y d\hat{k}_z\int n(\hat{x}^2+\hat{y}^2+\hat{z}^2)\exp[-i(\hat{k}_x\hat{x}+\hat{k}_y\hat{y}+\hat{k}_z\hat{z})]d\hat{x}d\hat{y}d\hat{z},$$

(A.33)

where $\hat{x}=\frac{x'}{a}$, $\hat{y}=\frac{y'}{b}$, and $\hat{z}=\frac{z'}{c}$, and $\hat{k}_x = k_x a$, $\hat{k}_y = k_y b$, and $\hat{k}_z = k_z c$.

Note that

$$I_1 = \int n(\hat{x}^2+\hat{y}^2+\hat{z}^2)\exp[-i(\hat{k}_x\hat{x}+\hat{k}_y\hat{y}+\hat{k}_z\hat{z})]d\hat{x}d\hat{y}d\hat{z},$$

$$= 4\pi\int_0^{\infty} n(\hat{r}^2)\,\hat{r}^2\frac{\sin(\hat{k}\hat{r})}{\hat{k}\hat{r}}d\hat{r}, \qquad \text{(A.34)}$$

where $\hat{r}^2 = \hat{x}^2+\hat{y}^2+\hat{z}^2$. Substituting Eq. (A.34) into Eq. (A.33) results in

$$\phi = \frac{2q}{\pi}\int \frac{\exp\left[i\left(\frac{\hat{k}_x x}{a}+\frac{\hat{k}_y y}{b}\right)\right]-1}{\frac{\hat{k}_x^2}{a^2}+\frac{\hat{k}_y^2}{b^2}} d\hat{k}_x d\hat{k}_y d\hat{k}_z \int_0^\infty n(\hat{r}^2)\,\hat{r}^2\,\frac{\sin(\hat{k}\hat{r})}{\hat{k}\hat{r}}d\hat{r}$$

$$= \frac{2q}{\pi}\int_0^\infty\int_0^\pi\int_0^{2\pi} \frac{\cos\left[k'\left(\frac{x\sin\theta\cos\varphi}{a}+\frac{y\sin\theta\cos\varphi}{b}\right)\right]-1}{\left[\left(\frac{\sin\theta\cos\varphi}{a}\right)^2+\left(\frac{\sin\theta\sin\varphi}{b}\right)^2\right]k'^2}\, k'^2\sin\theta dk' d\theta d\varphi \int_0^\infty n(\hat{r}^2)\,\hat{r}^2\,\frac{\sin(\hat{k}\hat{r})}{\hat{k}\hat{r}}d\hat{r}$$

$$= \lim_{c\to\infty}\left\{\frac{2q}{\pi}\int_0^\infty\int_0^\pi\int_0^{2\pi} \frac{\cos\left[k'\left(\frac{x\sin\theta\cos\varphi}{a}+\frac{y\sin\theta\cos\varphi}{b}+\frac{z\cos\theta}{c}\right)\right]-1}{\left[\left(\frac{\sin\theta\cos\varphi}{a}\right)^2+\left(\frac{\sin\theta\sin\varphi}{b}\right)^2+\left(\frac{\cos\theta}{c}\right)^2\right]}\sin\theta dk' d\theta d\varphi \int_0^\infty n(\hat{r}^2)\frac{\sin(\hat{k}\hat{r})}{\hat{k}\hat{r}}\hat{r}^2 d\hat{r}\right\} \tag{A.35}$$

Using the three-dimensional results of Eqs. (A.8) and (A.22), Eq. (A.35) becomes

$$\phi(x,y,z) = \lim_{c\to\infty}\left\{\pi\, qabc\int_0^\infty \frac{ds}{\sqrt{(a^2+s)(b^2+s)(c^2+s)}}\int_T^\infty n(T)dT - \right.$$

$$\left.\pi\, qabc\int_0^\infty \frac{ds}{\sqrt{(a^2+s)(b^2+s)(c^2+s)}}\int_0^\infty n(T)dT'\right\}$$

$$= -\pi\, qab\int_0^\infty \frac{ds}{\sqrt{(a^2+s)(b^2+s)}}\int_0^{T'} n(T')dT', \tag{A.36}$$

where

$$T = \frac{x^2}{a^2+s}+\frac{y^2}{b^2+s}+\frac{z^2}{c^2+s} \tag{A.37}$$

and

$$T' = \frac{x^2}{a^2 + s} + \frac{y^2}{b^2 + s}. \tag{A.38}$$

It is readily shown from the two-dimensional solution in Eq. (A.36) that $\phi = 0$ at $(x, y, z) = (0,0,0)$ and $\phi = \infty$ at $(x, y, z) = \infty$.

A.2 Solutions to Poisson equation in a cylindrical boundary

The two-dimensional Poisson equation in the cylindrical coordinates (r, φ, z) is expressed as

$$\frac{1}{r}\frac{\partial}{\partial r}\left(r\frac{\partial \phi}{\partial r}\right) + \frac{1}{r^2}\frac{\partial^2 \phi}{\partial \varphi^2} = -4\pi q n, \text{ and } \phi|_{r=R} = 0, \tag{A.39}$$

where ϕ is the potential, q is the particle charge, R is the radius of the infinitely long cylindrical conducting pipe, and n is the number density in the self-similar model, which can be expressed as

$$n = n\left(\frac{x^2}{a^2} + \frac{y^2}{b^2}\right). \tag{A.40}$$

In order to solve Eq. (A.39), we first find the Green function $G = G(r, r', \varphi, \varphi')$ for this problem. Here, $x = r\cos\varphi$, $y = r\sin\varphi$, $x' = r'\cos\varphi'$, and $y' = r'\sin\varphi'$. The Green function G satisfies

$$\frac{1}{r}\frac{\partial}{\partial r}\left(r\frac{\partial G}{\partial r}\right) + \frac{1}{r^2}\frac{\partial^2 G}{\partial \varphi^2} = -4\pi\frac{1}{r}\delta(r - r')\delta(\varphi - \varphi'), \text{ with } G|_{r=0} = 0. \tag{A.41}$$

Note that choosing $G|_{r=0} = 0$ is to avoid an infinite constant problem at $r = 0$.

The Green function G can be written in the form

$$G = G_f + G_b, \tag{A.42}$$

where $G_f = G_f(r, r', \varphi, \varphi')$ is the Green function in free space, satisfying

$$\frac{1}{r}\frac{\partial}{\partial r}\left(r\frac{\partial G_f}{\partial r}\right)+\frac{1}{r^2}\frac{\partial^2 G_f}{\partial \varphi^2} = -4\pi\frac{1}{r}\delta(r-r')\delta(\varphi-\varphi'),\ G_f\big|_{r=0} = 0, \text{ and } \nabla G_f\big|_{r=\infty} = 0, \tag{A.43}$$

and $G_b = G_b(r, r', \varphi, \varphi')$ satisfies

$$\frac{1}{r}\frac{\partial}{\partial r}\left(r\frac{\partial G_b}{\partial r}\right)+\frac{1}{r^2}\frac{\partial^2 G_b}{\partial \varphi^2} = 0, \text{ and } G_b\big|_{r=R} = -G_f\big|_{r=R}. \tag{A.44}$$

It is readily shown that

$$G_f = -\ln\left(r^2 + r'^2 - 2rr'\cos(\varphi-\varphi')\right)+\ln r'^2. \tag{A.45}$$

Using an image charge method, we obtain

$$G_b = \ln\left(r_1^2 + r'^2 - 2r_1 r'\cos(\varphi-\varphi')\right)-\ln r'^2, \tag{A.46}$$

where $r_1 = R^2/r$. Therefore, the entire Green function

$$G = G_f + G_b = -\ln\left(r^2 + r'^2 - 2rr'\cos(\varphi-\varphi')\right)+\ln r'^2 + \ln\left(r_1^2 + r'^2 - 2r_1 r'\cos(\varphi-\varphi')\right)-\ln r'^2. \tag{A.47}$$

Using the expansion

$$\ln(1+x^2-2x\cos\theta) = -2\sum_{m=1}^{\infty}\frac{x^m\cos m\theta}{m}, \text{ and } -1 \le x \le 1, \tag{A.48}$$

we rewrite G_f and G_b as

$$G_f = \begin{cases} \sum_{m=1}^{\infty} \frac{2}{m}\left(\frac{r}{r'}\right)^m \cos[m(\varphi-\varphi')], & r < r' \\ -2\ln\frac{r}{r'} + \sum_{m=1}^{\infty} \frac{2}{m}\left(\frac{r'}{r}\right)^m \cos[m(\varphi-\varphi')], & r > r' \end{cases} \tag{A.49}$$

and

$$G_b = 2\ln\frac{R^2}{rr'} - \sum_{m=1}^{\infty} \frac{2}{m}\left(\frac{r'}{R}\right)^m \left(\frac{r}{R}\right)^m \cos[m(\varphi-\varphi')], \text{ for } 0 \le r \le R \text{ and } 0 \le r' \le R. \tag{A.50}$$

Equations (A.49) and (A.50) may be useful for numerical calculation purpose in some special cases.

The potential ϕ can be expressed as

$$\phi = q\int_{s'} n(\mathbf{x}')G(\mathbf{x},\mathbf{x}')d\mathbf{x}' = q\int_{s'} n(\mathbf{x}')G_f(\mathbf{x},\mathbf{x}')d\mathbf{x}' + q\int_{s'} n(\mathbf{x}')G_b(\mathbf{x},\mathbf{x}')d\mathbf{x}', \tag{A.51}$$

or

$$\phi = \phi(r,\varphi) = q\int_{-\infty}^{\infty}\int_{-\infty}^{\infty} n\left(\frac{x'^2}{a^2}+\frac{y'^2}{b^2}\right)G_f(x,x',y,y')dx'dy' + q\int_{-\infty}^{\infty}\int_{-\infty}^{\infty} n\left(\frac{x'^2}{a^2}+\frac{y'^2}{b^2}\right)G_b(x,x',y,y')dx'dy', \tag{A.52}$$

where

$$N = \int_{-\infty}^{\infty}\int_{-\infty}^{\infty} n\left(\frac{x^2}{a^2}+\frac{y^2}{b^2}\right)dxdy = 2\pi ab\int_0^{\infty} n(\hat{r}^2)\hat{r}d\hat{r} \tag{A.53}$$

represents the charged particle number per unit length along the z direction.

Using Eq. (A.47) and the two-dimensional results in Eqs. (A.32) and (A.36) in the case of free space, we obtain the potential [12][73],

$$\phi = -\pi abq \int_0^{\infty} \frac{ds}{\sqrt{(a^2+s)(b^2+s)}} \int_0^{T} n(T)dT + \pi abq \int_0^{\infty} \frac{ds}{\sqrt{(a^2+s)(b^2+s)}} \int_0^{T_1} n(T_1)dT_1 , \tag{A.54}$$

where

$$T = \frac{x^2}{a^2+s} + \frac{y^2}{b^2+s} \tag{A.55}$$

and

$$T_1 = \frac{x_1^2}{a^2+s} + \frac{y_1^2}{b^2+s} \tag{A.56}$$

with

$$x_1 = \frac{R^2 x}{x^2+y^2} , \tag{A.57}$$

and

$$y_1 = \frac{R^2 y}{x^2+y^2} . \tag{A.58}$$

Equation (A.54) satisfies the Poisson equation (A.39) and the boundary condition $\phi|_{r=R} = 0$.

The potential in Eq. (A.54) still goes to infinity at $r = 0$ due to the second term. In order to solve this problem, we examine the Green functions in Eqs. (A.47) and (A.50). The singularity at $r = 0$ is due to the term $2\ln\frac{R}{r}$ in the Green function. Removing $2\ln\frac{R}{r}$ from the Green function in Eq. (A.50) does not change the physics because $A\ln\frac{R}{r}$ is really a homogeneous solution to the Poisson equation, satisfying the boundary condition $\phi|_{r=R} = 0$. Therefore, the solution of the potential can be rewritten as

$$\phi = -\pi abq \int_0^\infty \frac{ds}{\sqrt{(a^2+s)(b^2+s)}} \int_0^T n(T)dT + \pi abq \int_0^\infty \frac{ds}{\sqrt{(a^2+s)(b^2+s)}} \int_0^{T_1} n(T_1)dT_1 - 2q \ln\frac{R}{r} \int n(\mathbf{x}')d\mathbf{x}'$$

$$= -\pi abq \int_0^\infty \frac{ds}{\sqrt{(a^2+s)(b^2+s)}} \int_0^T n(T)dT + \pi abq \left[\int_0^\infty \frac{ds}{\sqrt{(a^2+s)(b^2+s)}} \int_0^{T_1} n(T_1)dT_1 - 2\ln\frac{R}{r} \int_0^\infty n(T_1)dT_1 \right].$$

(A.59)

Using the other form of the Green function in Eqs. (A.49) and (A.50), we obtain another form of the potential ϕ, i.e.,

$$\phi = -\pi abq \int_0^\infty \frac{ds}{\sqrt{(a^2+s)(b^2+s)}} \int_0^T n(T)dT$$

$$+ 2q \int_0^\infty \int_0^{2\pi} \ln\left(\frac{R^2}{rr'}\right) n\left(\frac{r'^2\cos^2\varphi'}{a^2} + \frac{r'^2\sin^2\varphi'}{b^2}\right) r'dr'd\varphi'$$

$$- 2q \sum_{m=1}^\infty \int_0^\infty \int_0^{2\pi} \frac{1}{m}\left(\frac{r'r}{R^2}\right)^m \cos[m(\varphi-\varphi')]\, n\left(\frac{r'^2\cos^2\varphi'}{a^2} + \frac{r'^2\sin^2\varphi'}{b^2}\right) r'dr'd\varphi'. \quad \text{(A.60)}$$

Removing the singular term from Eq. (A.60) results in

$$\phi = -\pi abq \int_0^\infty \frac{ds}{\sqrt{(a^2+s)(b^2+s)}} \int_0^T n(T)dT$$

$$+ 2q \int_0^\infty \int_0^{2\pi} \ln\left(\frac{R}{r'}\right) n\left(\frac{r'^2\cos^2\varphi'}{a^2} + \frac{r'^2\sin^2\varphi'}{b^2}\right) r'dr'd\varphi'$$

$$- 2q \sum_{m=1}^\infty \int_0^\infty \int_0^{2\pi} \frac{1}{m}\left(\frac{r'r}{R^2}\right)^m \cos[m(\varphi-\varphi')]\, n\left(\frac{r'^2\cos^2\varphi'}{a^2} + \frac{r'^2\sin^2\varphi'}{b^2}\right) r'dr'd\varphi'. \quad \text{(A.61)}$$

Equations (A.60) and (A.61) can be useful for numerical calculation purpose.

Appendix B

Self-Field Potential of an Elliptic Beam with a Uniform Density in a Cylindrical Conducting Pipe

B.1. Self-field potential inside the beam

The special case of the two-dimensional Poisson equation solution is the solution for the uniform beam density. The general solution is given by

$$\phi = -\pi abq\int_0^{\infty}\frac{ds}{\sqrt{(a^2+s)(b^2+s)}}\int_0^{T}n(T)dT + \pi abq\left[\int_0^{\infty}\frac{ds}{\sqrt{(a^2+s)(b^2+s)}}\int_0^{T_1}n(T_1)dT_1 - 2\ln\frac{R}{r}\int_0^{\infty}n(T_1)dT_1\right] \tag{B.1}$$

where

$$T = \frac{x^2}{a^2+s}+\frac{y^2}{b^2+s}, \tag{B.2}$$

$$T_1 = \frac{R^4}{(x^2+y^2)^2}\left(\frac{x^2}{a^2+s}+\frac{y^2}{b^2+s}\right). \tag{B.3}$$

The first part is produced by the beam charges in free-space and the second part is produced by the induced charges. For the uniform density,

$$n = \begin{cases} n_0, & \dfrac{x^2}{a^2}+\dfrac{y^2}{b^2}\le 1, \\ 0, & \dfrac{x^2}{a^2}+\dfrac{y^2}{b^2}\ge 1, \end{cases} \tag{B.4}$$

the free-space part is

$$\begin{aligned}\phi_i^{free-space} &= -\pi abq\int_0^\infty \frac{ds}{\sqrt{(a^2+s)(b^2+s)}}\int_0^T n(T)dT \\ &= -\pi abqn_0\int_0^\infty \frac{Tds}{\sqrt{(a^2+s)(b^2+s)}} \\ &= -\pi abqn_0\int_0^\infty \frac{ds}{\sqrt{(a^2+s)(b^2+s)}}\left(\frac{x^2}{a^2+s}+\frac{y^2}{b^2+s}\right).\end{aligned} \tag{B.5}$$

Using the identities

$$I = \int \frac{ds}{\sqrt{(a^2+s)(b^2+s)}} = \ln\left[2\sqrt{(a^2+s)(b^2+s)}+2s+a^2+b^2\right], \tag{B.6}$$

$$\int_0^\infty \frac{ds}{(a^2+s)^{\frac{3}{2}}(b^2+s)^{\frac{1}{2}}} = -2\frac{\partial I}{\partial(a^2)}\bigg|_0^\infty = \frac{2}{a(a+b)}\ , \tag{B.7}$$

$$\int_0^\infty \frac{ds}{(a^2+s)^{\frac{1}{2}}(b^2+s)^{\frac{3}{2}}} = -2\frac{\partial I}{\partial(b^2)}\bigg|_0^\infty = \frac{2}{b(a+b)}, \tag{B.8}$$

we obtain

$$\phi_i^{free-space} = -\pi abqn_0\left[\frac{2x^2}{a(a+b)}+\frac{2y^2}{b(a+b)}\right] = -\frac{2\pi abqn_0}{a+b}\left[\frac{x^2}{a}+\frac{y^2}{b}\right]. \tag{B.9}$$

The image part is

$$\phi_i^{image} = \pi abq\left[\int_0^\infty \frac{ds}{\sqrt{(a^2+s)(b^2+s)}}\int_0^{T_1} n(T_1)dT_1 - 2\ln\frac{R}{r}\int_0^\infty n(T_1)dT_1\right], \tag{B.10}$$

where

$$T_1 = \frac{R^4}{(x^2+y^2)^2}\left(\frac{x^2}{a^2+s}+\frac{y^2}{b^2+s}\right). \tag{B.11}$$

Since the density is nonzero only when $T_1 \le 1$, in the first term the integral should be broken into two parts

$$\phi_i^{image} = \pi abqn_0 \left[\int_0^{\xi_1} \frac{ds}{\sqrt{(a^2+s)(b^2+s)}} + \int_{\xi_1}^{\infty} \frac{T_1 ds}{\sqrt{(a^2+s)(b^2+s)}} - 2\ln\frac{R}{r} \right], \tag{B.12}$$

where $\xi_1 = \xi_1(x, y)$ is the solution of the equation

$$T_1(x, y, \xi_1) = \frac{R^4}{(x^2+y^2)^2}\left(\frac{x^2}{a^2+\xi_1} + \frac{y^2}{b^2+\xi_1}\right) = 1. \tag{B.13}$$

The solution to Eq. (B.13) is

$$\xi_1 = \frac{1}{2(x^2+y^2)}\left[R^4 - (a^2+b^2)(x^2+y^2) \pm \sqrt{R^8 - 2(a^2-b^2)(x^2-y^2)R^4 + (a^2-b^2)^2(x^2+y^2)^2}\right]. \tag{B.14}$$

For present purpose we take plus sign since ξ_1 is always positive.

To evaluate the integral, we use the identities

$$I = \int \frac{ds}{\sqrt{(a^2+s)(b^2+s)}} = \ln\left[2\sqrt{(a^2+s)(b^2+s)} + 2s + a^2 + b^2\right], \tag{B.15}$$

$$\int_0^{\xi_1} \frac{ds}{\sqrt{(a^2+s)(b^2+s)}} = \ln\left[2\sqrt{(a^2+\xi_1)(b^2+\xi_1)} + 2\xi_1 + a^2 + b^2\right] - 2\ln[a+b], \tag{B.16}$$

$$\int_{\xi_1}^{\infty} \frac{ds}{(a^2+\xi_1)^{\frac{3}{2}}(b^2+\xi_1)^{\frac{1}{2}}} = -2\frac{\partial I}{\partial(a^2)}\bigg|_{\xi_1}^{\infty} = 2\frac{\sqrt{\frac{b^2+\xi_1}{a^2+\xi_1}} + 1}{2\sqrt{(a^2+\xi_1)(b^2+\xi_1)} + 2\xi_1 + a^2 + b^2}, \tag{B.17}$$

$$\int_{\xi_1}^{\infty}\frac{ds}{\left(a^2+\xi_1\right)^{\frac{1}{2}}\left(b^2+\xi_1\right)^{\frac{3}{2}}}=-2\frac{\partial I}{\partial\left(b^2\right)}\Bigg|_{\xi_1}^{\infty}=2\frac{\sqrt{\frac{a^2+\xi_1}{b^2+\xi_1}}+1}{2\sqrt{\left(a^2+\xi_1\right)\left(b^2+\xi_1\right)}+2\xi_1+a^2+b^2}, \tag{B.18}$$

and obtain

$$\begin{aligned}\phi_i^{image}=2\pi abqn_0\Bigg[&\ln\left(\sqrt{a^2+\xi_1}+\sqrt{b^2+\xi_1}\right)-\ln(a+b)-\ln\frac{R}{\sqrt{x^2+y^2}}\\&+\frac{x^2\sqrt{b^2+\xi_1}+y^2\sqrt{a^2+\xi_1}}{\left(\sqrt{a^2+\xi_1}+\sqrt{b^2+\xi_1}\right)\sqrt{\left(a^2+\xi_1\right)\left(b^2+\xi_1\right)}}\times\frac{R^4}{\left(x^2+y^2\right)^2}\Bigg].\end{aligned} \tag{B.19}$$

The total potential is

$$\begin{aligned}\phi_i=-\frac{2\pi abqn_0}{a+b}\left[\frac{x^2}{a}+\frac{y^2}{b}\right]+2\pi abqn_0\Bigg[&\ln\left(\sqrt{a^2+\xi_1}+\sqrt{b^2+\xi_1}\right)-\ln(a+b)-\ln\frac{R}{\sqrt{x^2+y^2}}\\&+\frac{x^2\sqrt{b^2+\xi_1}+y^2\sqrt{a^2+\xi_1}}{\left(\sqrt{a^2+\xi_1}+\sqrt{b^2+\xi_1}\right)\sqrt{\left(a^2+\xi_1\right)\left(b^2+\xi_1\right)}}\times\frac{R^4}{\left(x^2+y^2\right)^2}\Bigg].\end{aligned} \tag{B.20}$$

B.2. Self-field potential outside the beam

Outside the beam, T can be bigger or less than 1 in different region, the integral of the potential is separated into two parts, i.e.,

$$\begin{aligned}\phi_o&=-\pi abq\Bigg[\int_0^{\xi}\frac{ds}{\sqrt{\left(a^2+s\right)\left(b^2+s\right)}}\int_0^1 n(T)dT+\int_{\xi}^{\infty}\frac{ds}{\sqrt{\left(a^2+s\right)\left(b^2+s\right)}}\int_0^T n(T)dT\\&=-\pi abqn_0\Bigg[\int_0^{\xi}\frac{ds}{\sqrt{\left(a^2+s\right)\left(b^2+s\right)}}+\int_{\xi}^{\infty}\frac{Tds}{\sqrt{\left(a^2+s\right)\left(b^2+s\right)}}\Bigg],\end{aligned} \tag{B.21}$$

where

$$T = \frac{x^2}{a^2+s} + \frac{y^2}{b^2+s}, \tag{B.22}$$

and $\xi = \xi(x, y)$ solves

$$\frac{x^2}{a^2+\xi} + \frac{y^2}{b^2+\xi} = 1. \tag{B.23}$$

Solving Eq. (B.23), we obtain

$$\xi = \frac{1}{2}\left[x^2 + y^2 - a^2 - b^2 \pm \sqrt{\left(x^2 + y^2 - a^2 - b^2\right)^2 + 4\left(b^2x^2 + a^2y^2 - a^2b^2\right)}\right]. \tag{B.24}$$

We take plus sign in Eq. (B.24) to make ξ positive.

Using the identities in Eqs. (B.15)-(B.18), we obtain

$$\phi_o^{\,free-space} = -2\pi abqn_0\left[\ln\left(\sqrt{a^2+\xi} + \sqrt{b^2+\xi}\right) - \ln(a+b) + \frac{x^2\sqrt{b^2+\xi} + y^2\sqrt{a^2+\xi}}{\left(\sqrt{a^2+\xi} + \sqrt{b^2+\xi}\right)\sqrt{\left(a^2+\xi\right)\left(b^2+\xi\right)}}\right]. \tag{B.25}$$

The potential produced by the induced image-charges is the same expression as the one inside the beam because the induced image-charges are located outside the cylindrical conducting pipe.

Therefore, the total potential outside the beam is

$$\phi_o = -2\pi abqn_0\left[\ln\left(\sqrt{a^2+\xi} + \sqrt{b^2+\xi}\right) - \ln(a+b) + \frac{x^2\sqrt{b^2+\xi} + y^2\sqrt{a^2+\xi}}{\left(\sqrt{a^2+\xi} + \sqrt{b^2+\xi}\right)\sqrt{\left(a^2+\xi\right)\left(b^2+\xi\right)}}\right]$$

$$+ 2\pi abqn_0\left[\ln\left(\sqrt{a^2+\xi_1} + \sqrt{b^2+\xi_1}\right) - \ln(a+b) - \ln\frac{R}{\sqrt{x^2+y^2}}\right.$$

$$+\frac{x^2\sqrt{b^2+\xi_1}+y^2\sqrt{a^2+\xi_1}}{\left(\sqrt{a^2+\xi_1}+\sqrt{b^2+\xi_1}\right)\sqrt{\left(a^2+\xi_1\right)\left(b^2+\xi_1\right)}}\times\frac{R^4}{\left(x^2+y^2\right)^2}\Bigg]. \tag{B.26}$$

Appendix C

Derivation of the Amplitude-Phase Equations

To derive a closed set of equations for the slowly varying variables A_{xi} and Φ_{xi}, we return to Eq. (4.39), i.e.,

$$\cos[\psi_x + \Phi_{xi}]\left[A'_{xi}w'_x - \frac{A_{xi}\Phi'_{xi}}{w_x}\right] - \sin[\psi_x + \Phi_{xi}]\left[\frac{A'_{xi}}{w_x} + A_{xi}\Phi'_{xi}w'_x\right] = -\frac{K}{4qN_b}\frac{\partial}{\partial x_{xi}}[\phi^s - \phi^s_{\mathrm{KV}}]. \tag{C.1}$$

We will perform two averages in the derivation.

C. 1 Average over fast envelope oscillations

We first take the average of Eq. (C.1) over the fast envelope oscillations $\frac{1}{S}\int_s^{s+S}(...)w_x ds$, i.e.,

$$\mathrm{LHS} = \frac{1}{S}\int_s^{s+S}\{\cos[\psi_x + \Phi_{xi}][A'_{xi}w'_x w_x - A_{xi}\Phi'_{xi}] - \sin[\psi_x + \Phi_{xi}][A'_{xi} + A_{xi}\Phi'_{xi}w'_x w_x]\}ds$$

$$= -A_{xi}\Phi'_{xi}\cos[\psi_x + \Phi_{xi}] - A'_{xi}\sin[\psi_x + \Phi_{xi}] \tag{C.2}$$

$$\mathrm{RHS} = \frac{1}{S}\int_s^{s+S}\left\{\frac{K}{(a+b)}\frac{x_i}{a} - \frac{K}{2N_p}\sum_{j=1(j\neq i)}^{N_p}\frac{x_i - x_j}{(x_i - x_j)^2 + (y_i - y_j)^2}\right\}w_x ds$$

$$= \int_s^{s+S}\left\{\frac{K}{a+b}\frac{A_{xi}a^2\cos[\psi_x + \Phi_{xi}]}{a\varepsilon_x} - \frac{K}{2N_p}\sum_{j=1(j\neq i)}^{N_p}\frac{x_i - x_j}{(x_i - x_j)^2 + (y_i - y_j)^2}\frac{a}{\varepsilon_x}\right\}d\hat{s} \tag{C.3}$$

For a well-matched beam, the envelopes of the beam can be treated as a small-amplitude modulations (oscillations with the period S) on the smoothed-beam envelopes

$$a(s) = \bar{a} + \delta a, \tag{C.4}$$

$$b(s) = \bar{b} + \delta b, \tag{C.5}$$

with $\bar{a} = \bar{b} = \int_s^{s+S} ads/S = \int_s^{s+S} bds/S$, $\delta a \approx -\delta b$, $\langle \delta a \rangle = \int_s^{s+S} \delta a ds/S = 0$, $\langle \delta b \rangle = \int_s^{s+S} \delta b ds/S = 0$ and $\delta a/\bar{a} << 1$ and $\delta b/\bar{b} << 1$. Therefore, Eq. (C.3) becomes

$$\begin{aligned}
\text{RHS} = & \frac{1}{s}\int_s^{s+S}\left\{\frac{K}{a+b}\frac{A_{xi}a^2\cos[\psi_x+\Phi_{xi}]}{a\varepsilon_x} - \frac{K}{2N_p}\sum_{j=1(j\neq i)}^{N_p}\frac{x_i-x_j}{(x_i-x_j)^2+(y_i-y_j)^2}\frac{a}{\varepsilon_x}\right\}d\hat{s} \\
= & \frac{K}{2\varepsilon_x}A_{xi}\cos[\psi_x+\Phi_{xi}] \\
& -\frac{K}{2N_p}\frac{1}{S}\int_s^{s+S}ds\sum_{j=1(j\neq i)}^{N_p}\frac{A_{xi}\cos[\psi_x+\Phi_{xi}]-A_{xj}\cos[\psi_x+\Phi_{xj}]}{w_x^2\{A_{xi}\cos[\psi_x+\Phi_{xi}]-A_{xj}\cos[\psi_x+\Phi_{xj}]\}^2+w_y^2\{A_{yj}\sin[\psi_y+\Phi_{yj}]\}^2}w_x^2.
\end{aligned} \tag{C.6}$$

Because of $a = \sqrt{\varepsilon_x}w_x = \bar{a} + \delta a$, $b = \sqrt{\varepsilon_y}w_y = \bar{b} + \delta b$, in the second term of Eq. (C.6) we only keep the first order of δa and δb. The yields

$$\begin{aligned}
& \frac{A_{xi}\cos[\psi_x+\Phi_{xi}]-A_{xj}\cos[\psi_x+\Phi_{xj}]}{w_x^2\{A_{xi}\cos[\psi_x+\Phi_{xi}]-A_{xj}\cos[\psi_x+\Phi_{xj}]\}^2+w_y^2\{A_{yj}\sin[\psi_y+\Phi_{yj}]\}^2}w_x^2 \\
= & \frac{A_{xi}\cos[\psi_x+\Phi_{xi}]-A_{xj}\cos[\psi_x+\Phi_{xj}]}{\frac{\bar{a}^2}{\varepsilon_x}\{A_{xi}\cos[\psi_x+\Phi_{xi}]-A_{xj}\cos[\psi_x+\Phi_{xj}]\}^2+\frac{\bar{b}^2}{\varepsilon_y}\{A_{yj}\sin[\psi_y+\Phi_{yj}]\}^2}\frac{\bar{a}^2}{\varepsilon_x}[1-\text{terms of order }\delta a]
\end{aligned} \tag{C.7}$$

Carrying out the average, we obtain

$$\text{RHS} = \frac{K}{2\varepsilon_x} A_{xi} \cos[\psi_x + \Phi_{xi}]$$
$$- \frac{K}{2\varepsilon_x N_p} \sum_{j=1(j\neq i)}^{N_p} \frac{A_{xi}\cos[\psi_x + \Phi_{xi}] - A_{xj}\cos[\psi_x + \Phi_{xj}]}{\frac{1}{\varepsilon_x}\{A_{xi}\cos[\psi_x + \Phi_{xi}] - A_{xj}\cos[\psi_x + \Phi_{xj}]\}^2 + \frac{1}{\varepsilon_y}\{A_{yj}\sin[\psi_y + \Phi_{yj}]\}^2}. \quad \text{(C.8)}$$

C. 2 Average over betatron oscillations

We now take the average of Eqs. (C.2) and (C.8) over the betatron oscillations $\frac{1}{\pi}\int_s^{s+2\pi S/\sigma_x}(...)\sin[\psi_x + \Phi_{xi}]d\psi_x$ and $\frac{1}{\pi}\int_s^{s+2\pi S/\sigma_x}(...)\cos[\psi_x + \Phi_{xi}]d\psi_x$.

C.2.1 Average of $\frac{1}{\pi}\int_s^{s+2\pi S/\sigma_x}(...)\sin[\psi_x + \Phi_{xi}]d\psi_x$ on Eq. (C.8)

$$\text{LHS} = \frac{1}{\pi}\int_s^{s+2\pi S/\sigma_x}\{-A_{xi}\Phi'_{xi}\cos[\psi_x + \Phi_{xi}] - A'_{xi}\sin[\psi_x + \Phi_{xi}]\}\sin[\psi_x + \Phi_{xi}]d\psi_x = A'_{xi}, \quad \text{(C.9)}$$

$$\text{RHS} = \frac{1}{\pi}\int_s^{s+2\pi S/\sigma_x}\sin[\psi_x + \Phi_{xi}]d\psi_x\left\{\frac{K}{2\varepsilon_x}A_{xi}\cos[\psi_x + \Phi_{xi}]\right.$$
$$\left. - \frac{K}{2\varepsilon_x N_p}\sum_{j=1(j\neq i)}^{N_p}\frac{A_{xi}\cos[\psi_x + \Phi_{xi}] - A_{xj}\cos[\psi_x + \Phi_{xj}]}{\frac{1}{\varepsilon_x}\{A_{xi}\cos[\psi_x + \Phi_{xi}] - A_{xj}\cos[\psi_x + \Phi_{xj}]\}^2 + \frac{1}{\varepsilon_y}\{A_{yj}\sin[\psi_y + \Phi_{yj}]\}^2}\right\}. \quad \text{(C.10)}$$

In Eq. (C.10) the first term goes to zero, and the numerator of the second term becomes

$$\{A_{xi}\cos[\psi_x+\Phi_{xi}]-A_{xj}\cos[\psi_x+\Phi_{xj}]\}\sin[\psi_x+\Phi_{xi}]$$

$$=\frac{A_{xi}}{2}\sin[2\psi_x+2\Phi_{xi}]-\frac{A_{xj}}{2}\sin[2\psi_x+2\Phi_{xi}]\cos\Delta_{xj}-\frac{A_{xj}}{2}\cos[2\psi_x+2\Phi_{xi}]\sin\Delta_{xj}+\frac{A_{xj}}{2}\sin\Delta_{xj}$$

$$=-B_j+B_j\cos[2\psi_x+2\Phi_{xi}]+C_j\sin[2\psi_x+2\Phi_{xi}],$$

(C.11)

where

$$B_j=-\frac{1}{2}\frac{A_{xj}}{\sqrt{\varepsilon_x}}\sin\Delta_{xj}, \tag{C.12}$$

$$C_j=\frac{1}{2\sqrt{\varepsilon_x}}\left(A_{xi}-A_{xj}\cos\Delta_{xj}\right), \tag{C.13}$$

with $\Delta_{xj}=\Phi_{xj}-\Phi_{xi}$.

The denominator of the second term becomes

$$\frac{1}{\varepsilon_x}\{A_{xi}\cos[\psi_x+\Phi_{xi}]-A_{xj}\cos[\psi_x+\Phi_{xj}]\}^2+\frac{1}{\varepsilon_y}\{A_{yj}\sin[\psi_y+\Phi_{yj}]\}^2$$

$$=\frac{1}{\varepsilon_x}\{A_{xi}^2\cos^2[\psi_x+\Phi_{xi}]+A_{xj}^2\cos^2[\psi_x+\Phi_{xj}]-2A_{xi}A_{xj}\cos[\psi_x+\Phi_{xi}]\cos[\psi_x+\Phi_{xj}]\}+\frac{A_{yj}^2}{\varepsilon_y}\sin^2[\psi_y+\Phi_{yj}]$$

$$\begin{aligned}=&\left[\frac{A_{xi}^2}{2\varepsilon_x}+\frac{A_{xj}^2}{2\varepsilon_x}-\frac{A_{xi}A_{xj}}{\varepsilon_x}\cos\Delta_{xj}-\frac{A_{yi}^2}{2\varepsilon_y}\right]+\cos[2\psi_x+2\Phi_{xj}]\left\{\frac{A_{xi}^2}{2\varepsilon_x}+\frac{A_{xj}^2}{2\varepsilon_x}\cos2\Delta_{xj}-\frac{A_{xi}A_{xj}}{\varepsilon_x}\cos\Delta_{xj}\right\}\\&+\sin[2\psi_x+2\Phi_{xj}]\left\{-\frac{A_{xj}^2}{2\varepsilon_x}\sin2\Delta_{xj}+\frac{A_{xi}A_{xj}}{\varepsilon_x}\sin\Delta_{xj}\right\}+\frac{A_{yj}^2}{\varepsilon_y}\sin^2[\psi_y+\Phi_{yj}]\end{aligned} \tag{C.14}$$

Let us examine the last term in Eq. (C.14) and define $\Delta_\psi=\psi_y-\psi_x$. This term can be expressed as

$$\frac{A_{yj}^2}{\varepsilon_y}\sin^2[\psi_y+\Phi_{yj}]=\frac{A_{yj}^2}{2\varepsilon_y}[1-\cos[2\psi_y+2\Phi_{yj}]]=\frac{A_{yj}^2}{2\varepsilon_y}[1-\cos(2\psi_x+2\Phi_{xi}+2\Delta_\psi+2\Delta_{yj})]$$

$$=\frac{A_{yj}^2}{2\varepsilon_y}[1-\cos(2\psi_x+2\Phi_{xi})\cos(2\Delta_\psi+2\Delta_{yj})+\sin(2\psi_x+2\Phi_{xi})\sin(2\Delta_\psi+2\Delta_{yj})]. \tag{C.15}$$

Finally, Eq. (C.14) can be written as

$$a_j+b_j\cos[2\psi_x+2\Phi_{xi}]+c_j\sin[2\psi_x+2\Phi_{xi}], \tag{C.16}$$

where

$$a_j=\frac{A_{xi}^2}{2\varepsilon_x}-\frac{A_{xi}A_{xj}}{\varepsilon_x}\cos\Delta_{xj}+\frac{A_{xj}^2}{2\varepsilon_x}+\frac{A_{yj}^2}{2\varepsilon_y}, \tag{C.17}$$

$$b_j=\frac{1}{2\varepsilon_x}(A_{xi}-A_{xj}\cos\Delta_{xj})^2-\frac{1}{2\varepsilon_x}(A_{xj}\sin\Delta_{xj})^2-\frac{A_{yj}^2}{2\varepsilon_y}\cos[2\Delta_\psi+2\Delta_{yj}], \tag{C.18}$$

$$c_j=\frac{1}{\varepsilon_x}(A_{xi}-A_{xj}\cos\Delta_{xj})A_{xj}\sin\Delta_{xj}+\frac{A_{yj}^2}{2\varepsilon_y}\sin[2\Delta_\psi+2\Delta_{yj}]. \tag{C.19}$$

Note that Δ_ψ is nearly constant. This is because $\psi_x=\int_0^s ds/w_x^2(s)$ and $\psi_y=\int_0^s ds/w_y^2(s)$ and in the smoothed-beam approximation for $\varepsilon_x=\varepsilon_y$,

$$\psi_x=\int_0^s\frac{ds}{w_x^2(s)}=\varepsilon_x\int_0^s\frac{ds}{a^2(s)}=\varepsilon_x\int_0^s\frac{ds}{(\bar{a}+\delta a)^2}\cong\frac{\varepsilon_x}{\bar{a}^2}\int_0^s\left(1-2\frac{\delta a}{\bar{a}}\right)ds=\frac{\varepsilon_x}{\bar{a}^2}s, \tag{C.20}$$

$$\psi_y=\int_0^s\frac{ds}{w_y^2(s)}=\varepsilon_y\int_0^s\frac{ds}{b^2(s)}=\varepsilon_y\int_0^s\frac{ds}{(\bar{b}+\delta b)^2}\cong\frac{\varepsilon_y}{\bar{b}^2}\int_0^s\left(1-2\frac{\delta b}{\bar{b}}\right)ds=\frac{\varepsilon_y}{\bar{b}^2}s. \tag{C.21}$$

Using the identity

$$\int_0^{2\pi} \frac{A + B\cos x + C\sin x}{a + b\cos x + c\sin x} dx = 2\pi \frac{Bb + Cc}{b^2 + c^2}, \tag{C.22}$$

Eq. (C.10) becomes

$$\text{RHS} = -\frac{K}{\sqrt{\varepsilon_x} N_p} \sum_{j=1(j\neq i)}^{N_p} \frac{B_j b_j + C_j c_j}{b_j^2 + c_j^2} . \tag{C.23}$$

C.2.2 Average of $\frac{1}{\pi}\int_s^{s+2\pi S/\sigma_x}(...)\cos[\psi_x + \Phi_{xi}]d\psi_x$ on Eq. (C.8)

$$\text{LHS} = \frac{1}{\pi}\int_s^{s+2\pi S/\sigma_x}\{-A_{xi}\Phi'_{xi}\cos[\psi_x + \Phi_{xi}] - A'_{xi}\sin[\psi_x + \Phi_{xi}]\}\cos[\psi_x + \Phi_{xi}]d\psi_x = -A_{xi}\Phi'_{xi}, \tag{C.24}$$

$$\text{RHS} = \frac{1}{\pi}\int_s^{s+2\pi S/\sigma_x}\cos[\psi_x + \Phi_{xi}]d\psi_x \left\{\frac{K}{2\varepsilon_x}A_{xi}\cos[\psi_x + \Phi_{xi}]\right.$$

$$\left. - \frac{K}{2\varepsilon_x N_p}\sum_{j=1(j\neq i)}^{N_p} \frac{A_{xi}\cos[\psi_x + \Phi_{xi}] - A_{xj}\cos[\psi_x + \Phi_{xj}]}{\frac{1}{\varepsilon_x}\{A_{xi}\cos[\psi_x + \Phi_{xi}] - A_{xj}\cos[\psi_x + \Phi_{xj}]\}^2 + \frac{1}{\varepsilon_y}\{A_{yj}\sin[\psi_y + \Phi_{yj}]\}^2}\right\}$$

$$= \frac{A_{xi}K}{2\varepsilon_x}$$

$$-\frac{1}{\pi}\int_s^{s+2\pi S/\sigma_x} d\psi_x \frac{K}{2\varepsilon_x N_p}\sum_{j=1(j\neq i)}^{N_p} \frac{\{A_{xi}\cos[\psi_x + \Phi_{xi}] - A_{xj}\cos[\psi_x + \Phi_{xj}]\}\cos[\psi_x + \Phi_{xi}]}{\frac{1}{\varepsilon_x}\{A_{xi}\cos[\psi_x + \Phi_{xi}] - A_{xj}\cos[\psi_x + \Phi_{xj}]\}^2 + \frac{1}{\varepsilon_y}\{A_{yj}\sin[\psi_y + \Phi_{yj}]\}^2}$$

(C.25)

The numerator of the second term in Eq. (C.25) becomes

$$\{A_{xi}\cos[\psi_x+\Phi_{xi}]-A_{xj}\cos[\psi_x+\Phi_{xj}]\}\cos[\psi_x+\Phi_{xi}]$$

$$=\frac{A_{xi}}{2}+\frac{A_{xi}}{2}\cos[2\psi_x+2\Phi_{xi}]-\frac{A_{xj}}{2}\cos[2\psi_x+2\Phi_{xi}]\cos\Delta_{xj}+\frac{A_{xj}}{2}\sin[2\psi_x+2\Phi_{xi}]\sin\Delta_{xj}+\frac{A_{xj}}{2}\cos\Delta_{xj}$$

$$=C_j+C_j\cos[2\psi_x+2\Phi_{xi}]-B_j\sin[2\psi_x+2\Phi_{xi}] \tag{C.26}$$

Eq. (C.25) becomes

$$\text{RHS}=\frac{A_{xi}K}{2\varepsilon_x}-\frac{K}{\sqrt{\varepsilon_x}N_p}\sum_{j=1(j\neq i)}^{N_p}\frac{C_jb_j-B_jc_j}{b_j^2+c_j^2}. \tag{C.27}$$

Collecting the results above [i.e., Eqs. (C.9), (C.23), (C.24) and (C.27)], we have the differential equations which determine the slowly varying variables A_{xi} and Φ_{xi},

$$\frac{dA_{xi}}{ds}=-\frac{K}{\sqrt{\varepsilon_x}N_p}\sum_{j=1(j\neq i)}^{N_p}\frac{B_jb_j+C_jc_j}{b_j^2+c_j^2}\ , \tag{C.28}$$

$$\frac{d\Phi_{xi}}{ds}=\frac{K}{2\varepsilon_x}-\frac{K}{A_{xi}\sqrt{\varepsilon_x}N_p}\sum_{j=1(j\neq i)}^{N_p}\frac{C_jb_j-B_jc_j}{b_j^2+c_j^2}. \tag{C.29}$$

Reference

[1] R. B. Miller, *An introduction to the physics of intense charged particle beam* (Plenum press, New York and London, 1982).

[2] P. A. Seidl, *et al.*, The High Current Transport Experiment for Heavy Ion Inertial Fusion, LBNL-53014 (2003).

[3] P. K. Roy, S. S. Yu, S. Eylon, *et al.*, Neutralized transport experiment, Nucl. Instrum. Methods Phys. Res. **A 544,** 225–235 (2005).

[4] G. Scheitrum, Design and Construction of a W-band Sheet Beam Klystron, SLAC-PUB-11688.

[5] B. E. Carlsten, S. J. Russell, L. M. Earley, *et al.*, Technology Development for a mm-Wave Sheet-Beam Traveling-Wave Tube, IEEE Trans. on Plasma Sci. **33**, 85 (2005).

[6] *"29th ICFA Advanced Beam Dynamics Workshop on Beam-Halo Dynamics, Diagnostics, and Collimation and the Beam-Beam'03 Workshop"*, AIP Conference Proceedings **693**, edited by J. Wei, W. Fischer, P. Manning, (Montauk, New York, 19-23 May 2003).

[7] A. V. Fedotov, Mechanisms of halo formation, AIP Conf. Proc. **693**, edited by J. Wei, W. Fischer, and P. Manning (Montauk, New York, May 2003), p. 3.

[8] Q. Qian, R. C. Davidson, and C. Chen, Halo formation induced by density nonuniformities in intense ion beams, Phys. Rev. **E 51**, R5216 (1995).

[9] T. P. Wangler, Physics results from the Los Alamos beam-halo experiment, AIP Conf. Proc. **693**, edited by J. Wei, W. Fischer, and P. Manning (Montauk, New York, 19-23 May 2003), p. 108.

[10] I. M. Kapchinskij and V. V. Vladimirskij, in *Proceedings of the International Conference on High Energy Accelerator* (CERN, Geneva, 1959), p. 274.

[11] P. Lapostolle, CERN Repoet AR/Int SG/65-15 (1965).

[12] F. J. Sacherer, IEEE Trans. Nucl. Sci. **NS-18**, 1105 (1971).

[13] P. Lapostolle, IEEE Trans. Nucl. Sci. **NS-18**, 1101 (1971).

[14] C. K. Allen, Ph. D. dissertation, University of Maryland (1996).

[15] C. K. Allen and M. Reiser, Image effects of cylindrical pipes on continuous beams, Phys. Rev. **E 54**, 2884 (1996).

[16] C. K. Allen and M. Reiser, Bunched beam envelope equations including image effects from a cylindrical pipe, Phys. Rev. **E 55**, 7591 (1997).

[17] B. L. Qian, J. Zhou and C. Chen, private communication (2002).

[18] B. L. Qian, J. Zhou and C. Chen, Image-charge effects on the envelope dynamics of an unbunched intense charged-particle beam, Phys. Rev. ST-AB, **6**, 014201 (2003).

[19] S. Yu, S. Eylon, E. Henestroza, and D. Grote, in *Space Charge Dominated Beams and Applications of High-Brightness Beams*, AIP Conf. Proc. **377**, edited by S. Y. Lee (AIP, New York, 1996).

[20] Q. Qian and R. C. Davidson, Nonlinear dynamics of intense ion beam envelopes, Phys. Rev. **E53**, 5349 (1996).

[21] I. Hofmann, L. Laslett, L. Smith, and I. Haber, Part. Accel. **13**, 145 (1983).

[22] J. Stuckmeier, J. Klabunde, and M. Reiser, Part. Accel. **15**, 47 (1984).

[23] R. Pakter and F. B. Rizzato, Stability of Periodically Focused Intense Particle Beams, Phys. Rev. Lett. **87**, 044801 (2001).

[24] R. Pakter and F. B. Rizzato, Nonlinear dynamics of periodically focused intense particle beams, Phys. Rev. **E65**, 056503 (2002).

[25] C. Chen, and R. Pakter, Mechanisms and control of beam halo formation in intense microwave sources and accelerators, Phys. Plasmas **7**, 2203 (2000).

[26] C. Chen, R. Pakter, and R. C. Davidson, Ideal matching of heavy ion beams, Nucl. Instrum. Methods Phys. Res. **A464**, 518 (2001).

[27] E. Lee, et al, eds, *Proceedings of 13th International Symposium on Heavy Ion Inertial Fusion*, Nucl. Instrum. Methods Phys. Res. **A464** (2001).

[28] Q. Qian, R. C. Davidson, and C. Chen, Chaotic particle motion and halo formation induced by charge nonuniformities in an intense ion beam propagating through a periodic quadrupole focusing field, Phys. Plasmas **2**, 2674 (1995).

[29] J. M. Lagniel, Chaotic behavior and halo formation from 2D space-charge dominated beams, Nucl. Instrum. Methods Phys. Res. **A 345**, 405 (1994).

[30] R. L. Gluckstern, Analytic Model for Halo Formation in High Current Ion Linacs, Phys. Rev. Lett. **73**, 1247 (1994).

[31] C. M. Celata, I. Haber, and D. P. Grote, *Proceedings of the 2001 Particle Accelerator Conference*, Chicago, IL, 2001 (IEEE, Piscataway, NJ, 2001), pp. 2926-2928.

[32] R. W. Garnett, J. H. Billen, K. C. D. Chan, *et al.*, in *Space Charge Dominated Beams and Applications of High Brightness Beams*, edited by S. Y. Lee, AIP Conf. Proc. No. **377** (AIP, New York, 1996), p. 60.

[33] C. M. Celata, F. M. Bieniosek, L. Prost, *et al.*, *Proc. of the 2003 Particle Accel. Conf.*, Portland, OR, May 2003 (IEEE, Piscataway, NJ, 2003), p. 1518.

[34] J. Zhou and C. Chen, Parametric studies of image-charge effects on an intense beam in a small-aperture alternating-gradient focusing system, Nucl. Instrum. Methods Phys. Res. **A 544/1-2**, 492-496 (2005).

[35] J. Zhou, B. L. Qian and C. Chen, Chaotic particle motion and beam halo formation induced by image-charge effects in a small-aperture alternating-gradient focusing system, Phys. Plasma **10**, 4203 (2003).

[36] R. C. Davidson, *Physics of Nonneutral Plasmas* (Addison-Wesley, Reading, MA, 1990), Chap. 10, and references therein.

[37] IMSL Fortran Subroutines for Mathematical Applications, published by Visual Numerics, Inc.

[38] P. A. Seidl, F. M. Bieniosek, C. M. Celata, *et al.,* Experiments at the Virtual National Laboratory for Heavy Ion Fusion, Nucl. Instrum. Methods Phys. Res. **A 464**, 369 (2001).

[39] A. J. Lichtenberg and M. A. Lieberman, *Regular and Chaotic Dynamics,* Applied Mathematical Science **38** (Springer-Verlag, New York, 1992).

[40] J. M. Dawson, Phys. Rev. **118**, 381-389 (1960).

[41] J. M. Dawson, One-Dimensional Plasma Model, Phys. Fluids **5**, 445-459 (1962).

[42] J. M. Dawson, Particles simulations of plasmas, Rev. Mod. Phys. **55**, 403-447 (1983).

[43] C. K. Birdsall, A. B. Langdon, *Plasma Physics via Computer Simulation* (Institute of Physics Publishing, Bristol and Philadelphia, 1991).

[44] K. Ko et el., Impact of SciDAC on Accelerator Projects across the Office of Science through Electromagnetic Modelling, Proc. of SciDAC 2005 Conference, San Francisco (2005).

[45] D. P. Grote, A. Friedman, I. Haber, Methods used in WARP3d, a Three-Dimensional PIC/Accelerator Code, Proc. of the 1996 Computational Accel. Phys. Conf., AIP Conf. Proc. **391**, p. 51 (1996).

[46] B. Goplen, et al., User-Configurable MAGIC for electromagnetic PIC calculations, Computer Phys. Comm., **87**, 54–86 (1995).

[47] C. Nieter and J. R. Cary, VORPAL: a versatile plasma simulation code, J. Comp. Phys. **196**, 448-472 (2004).

[48] J. Zhou, R. Pakter and C. Chen, manuscript in preparation (2006).

[49] W. H. Press, S. A. Teukolsky, W. T. Vetterling, *et al.*, *Numerical Recipes in C* (CAMBRIDGE UNIVERSITY PRESS, New York, 1992), Chapter 17 and references therein.

[50] R. Pakter and C. Chen, *Proceedings of the 1997 Particle Accelerator Conference* (IEEE, Vancouver, Canada, 1997), p. 1938.

[51] P. A. Sturrock, J. Electron. Control **7**, 162 (1959).

[52] Z. X. Zhang, V. L. Granatstein, W.W. Destler, *et al.*, Experimental and numerical studies of sheet electron beam propagation through a planar wiggler magnet, IEEE Tran. Plasma Sci. **21**, 760 (1993).

[53] J. H. Booske, B. D. McVey, and T. M. Antonsen, Stability and confinement of nonrelativistic sheet electron beams with periodic cusped magnetic focusing, Jr., J. Appl. Phys. **73**, 4140 (1993).

[54] J. H. Booske, A. H. Kumbasar, and M. A. Basten, Periodic focusing and ponderomotive stabilization of sheet electron beams, Phys. Rev. Lett. **71**, 3979 (1993).

[55] J. H. Booske and M. A. Basten, Demonstration via simulation of stable confinement of sheet electron beams using periodic magnetic focusing, IEEE Tran. Plasma Sci. **27**, 134 (1999).

[56] M. A. Basten and J. H. Booske, Two-plane focusing of high-space-charge sheet electron beams using periodically cusped magnetic fields, J. Appl. Phys. **85**, 6313 (1999).

[57] F. J. Sacherer, Transverse Space-Charge Effects in Circular Accelerators, Ph. D. Thesis, Lawrence Radiation Laboratory, Univ. of California, Berkeley (October 30, 1968), p. 15-19.

[58] V. Danilov, S. Cousineau, S. Henderson, and J. Holmes, Self-consistent time dependent two dimensional and three dimensional space charge distributions with linear force, Phys. Rev. ST-AB **6**, 094202 (2003).

[59] R. C. Davidson, *Physics of Nonneutral Plasma* (Addison-Wesley, 1990), p. 694.

[60] R. C. Davidson and H. Qin, *Physics of Intense Charged Particle Beams in High Energy Accelerators* (World Scientific, Singapore, 2001), p. 242.

[61] R. Pakter and C. Chen, Cold-fluid equilibrium for a corkscrewing elliptic beam in a variably focusing channel, Phys. Rev. E **62**, 2789 (2000).

[62] C. Chen and R. Pakter, Mechanisms and control of beam halo formation in intense microwave sources and accelerators, Phys. Plasmas **7**, 2203 (2000).

[63] R. C. Davidson, P. Stoltz and C. Chen, Intense non-neutral beam propagation in a periodic solenoidal field using a macroscopic fluid model with zero thermal emittance, Phys. Plasmas **4**, 3710 (1997).

[64] R. Bhatt and C. Chen, Theory and simulation of nonrelativistic elliptic-beam formation with one-dimensional Child-Langmuir flow characteristics, Phys. Rev. ST-AB **8**, 014201 (2005).

[65] J. Zhou, R. Bhatt and C. Chen, Cold-fluid theory of equilibrium and stability of a high-intensity periodically twisted ellipse-shaped charged-particle beam, Phys. Rev. ST Accel. Beams **9**, 034401 (2006).

[66] Field Precision, Omnitak manual: OmniTrak 1.0 Three-dimensional Charged-particle Optics and Gun Design (2003).

[67] I. M. Kapchinskij, and V. V. Vladimirskij, in Proc. of the International Conf. on High Energy Accel. (CERN, Geneva, 1959), p. 274; F. J. Sacherer, Transverse Space-Charge Effects in Circular Accelerators, Ph. D. Thesis, Lawrence Radiation Laboratory, Univ. of California, Berkeley (October 30, 1968), p. 15-19.

[68] R. C. Davidson, *Physics of Nonneutral Plasma* (Addison-Wesley, 1990), p. 694.

[69] C. Chen, R. Pakter, and R. Davidson, Rigid-Rotor Vlasov Equilibrium for an Intense Charged-Particle Beam Propagating through a Periodic Solenoidal Magnetic Field, Phys. Rev. Lett. **79**, 225 (1997).

[70] R. C. Davidson and H. Qin, *Physics of Intense Charged Particle Beams in High Energy Accelerators* (World Scientific, Singapore, 2001), p. 242.

[71] R. Bhatt, J. Zhou, and C. Chen, Three Dimensional Simulation of Large-Aspect-Ratio Ellipse-Shaped Charged-Particle Beam Propagation, Proc. of the 2005 Part. Accel. Conf., (Knoxville, TN, 2005), p. 823.

[72] C. Chen, private communication, (2002).

[73] O. D. Kellogg, *Foundations of Potential Theory* (Dover, New York, 1953).

[74] R. C. Davidson, *Physics of Nonneutral Plasma* (Addison-Wesley, 1990), p. 52.

[75] J. Zhou and C. Chen, Thermal Equilibrium of Periodically focused Axisymmetric Beams, manuscript in preparation (2006).

[76] A. V. Fedotov and R. L. Gluckstern, Proc. of the 1999 Part. Accel. Conf. (New York, 1999), p. 606.

[77] I. S. Gradshteyn and I. M. Ryzhik, Table of Integrals, Series, and Products, (Academic press, 2000).